博士學位 請求論文

指導敎授 崔 榮 一

A Measurement of $\nu_\mu \leftrightarrow \nu_\tau$ Oscillation Parameters Using Atmospheric Neutrino Observed in Super Kamiokande-I and Super Kamiokande-II

成均館大學校 大學院

物理學科

核및粒子物理專攻

徐 賢 寬

博士學位 請求論文

指導敎授 崔 榮 一

A Measurement of $\nu_\mu \leftrightarrow \nu_\tau$ Oscillation Parameters Using Atmospheric Neutrino Observed in Super Kamiokande-I and Super Kamiokande-II

이 論文을 理學 博士學位請求論文으로 提出합니다

2006年 4月 日

成均館大學校 大學院

物理學科

核및粒子物理專攻

徐 賢 寬

이 論文을 徐賢寬의 理學
博士學位 論文으로 認定함

2006年 6月 日

審査委員長 오 필 렬

審査委員 김 수 봉

審査委員 박 차 원

審査委員 최 수 용

審査委員 최 영 일

A Measurement of $\nu_\mu \leftrightarrow \nu_\tau$ Oscillation Parameters Using Atmospheric Neutrino Observed in Super Kamiokande-I and Super Kamiokande-II

Hyunkwan Seo
Department of Physics
Sungkyunkwan University

Abstract

The deficit of atmospheric muon neutrinos observed in Super Kamiokande is well explained by $\nu_\mu \leftrightarrow \nu_\tau$ oscillation hypothesis. In this study, neutrino oscillation analysis was done utilizing zenith angle and energy dependent deficit of atmospheric muon neutrinos. The effect of momentum binning on the constraint of oscillation parameters was investigated. The best-fit parameters were located at ($\sin^2 2\theta = 1.00$, $\Delta m^2 = 2.5\times10^{-3}$ eV^2) with the minimum χ^2 value, χ^2_{min} = 767.5 / 737 DOF by the combined analysis of Super Kamiokande−I and Super Kamiokande-II data in the optimized momentum binning. The allowed oscillation parameter regions were $\sin^2 2\theta > 0.93$ and $2.1\times10^{-3} < \Delta m^2 < 3.0\times10^{-3}$ eV^2 at 90% C.L.

Contents

List of Tables

List of Figures

Chapter 1

Introduction

1.1 Review of neutrino mass and oscillation

Neutrinos are still the least known particles among the well-established fundamental fermions in the Universe. The most important property of the neutrinos is whether neutrinos are massive or not. Neutrino interacts very little with other matter. It can travel through 50 billion miles of water without interacting. On the surface of the earth, about a half of a trillion neutrinos from the sun pass through each square centimeter of area every second. It is also believed that there are 300 relic neutrinos per cubic centimeter of a volume in our universe which were produced about one second after the Bing-bang. Thus, if neutrino has non-zero mass, it can contribute to the mass and ultimate fate of the universe. The direct mass measurements based on the decay kinematics of ^3H, π and τ have been tried but it appeared that we reached the end of the road on this effort unless a new generation of the techniques is forthcoming. There is, however, the promising way to probe the neutrino mass, which is referred to as neutrino oscillation experiments. Oscillation is the changing of a neutrino's type as it travels through space or matter. This can occur only if the neutrino possesses mass. When a neutrino is created it must be of a specific flavor, that is, it must be an electron neutrino (ν_e), a muon neutrino (ν_μ) or a tau neutrino (ν_τ). When one speaks of massive neutrinos they are given the labels ν_1, ν_2 and ν_3 which have mass m_1, m_2 and m_3, respectively. In general a neutrino of a particular flavor will

be a linear superposition of three neutrinos, each of a particular mass. Recent experiments using atmospheric [2-5], solar [41,42], reactor [43] and accelerator neutrinos [44] have demonstrated that neutrino change flavor as they travel from the source to the detector, a phenomenon consistent with the hypothesis of neutrino oscillation. The finding is a major discovery with a far reaching impact in the elementary particle physics, cosmology and astrophysics. The phenomenon of neutrino oscillation which requires neutrinos to have non-zero mass will alter our view of the world of elementary particles, and the Standard Model, the currently prevailing theory of the elementary particles, must be modified. In the Standard Model the neutrinos have zero mass. The finding will also make the theories of the Grand Unification more viable and attractive, and make the universe a lot heavier than we currently assume.

1.2 Calculation of neutrino oscillation probability

If neutrinos are massive and mixed, neutrinos are produced and detected in the form of the weak eigenstates whereas when they propagate their motion is dictated by the mass eigenstates. This leads to the phenomenon of neutrino oscillations [20]. If neutrinos oscillate, the weak eigenstates and mass eigenstates are related by a unitary matrix U as

$$\nu_W = U\nu_M ,$$

Where, in the case of the two generations of neutrinos,

$$U = \begin{pmatrix} \cos\theta & \sin\theta \\ -\sin\theta & \cos\theta \end{pmatrix}$$

The equation of motion for the mass eigenstate is

$$i\dot{\nu}_M = H\nu_M = \begin{pmatrix} E_1 & 0 \\ 0 & E_2 \end{pmatrix}\nu_M$$

$$where, \quad \nu_M = \begin{pmatrix} \nu_1 \\ \nu_2 \end{pmatrix}$$

Since neutrinos are expected to be extremely relativistic, if we use the following approximation,

$$E_i = \sqrt{p^2 + m_i^2} \cong p + \frac{m_i^2}{2p} : p \cong E$$

then

$$i\dot{\nu}_M = \left[E \cdot 1 + \frac{1}{2E}\begin{pmatrix} m_1^2 & 0 \\ 0 & m_2^2 \end{pmatrix} \right]\nu_M$$

Replacing $\nu_M \rightarrow e^{i\alpha t}\nu_M$, the above equation becomes

$$i\dot{\nu}_M = (E + \alpha)\nu_M + \frac{1}{2E}\mathrm{M}_M\nu_M$$

Where $\mathrm{M}_M = \begin{pmatrix} m_1^2 & 0 \\ 0 & m_2^2 \end{pmatrix}$.

Taking $\alpha = -E$,

$$i\dot{\nu}_M = \frac{1}{2E}\mathrm{M}_M\nu_M$$

Now, using $\nu_M = U^+(\theta)\nu_W$, the equation of motion for weak eigenstates can be

derived as

$$i\dot{\nu}_M = \frac{1}{2E}U(\theta)\mathrm{M}_M U(\theta)^+ \nu_W$$

By solving the above differential equation, we obtain the well–known oscillation probability for the two generation case.

$$P(\nu_\alpha \to \nu_\beta) = \sin^2 2\theta \sin^2\left(\frac{1.27\Delta m^2(eV^2)L(km)}{E_\nu(GeV)}\right)$$

where, θ is the mixing angle, Δm^2 is the difference of the squared mass eigenvalues, L is the distance from source to detector, and E_ν is neutrino energy.

1.3 Usefulness of atmospheric neutrino for the oscillation study

Atmospheric neutrinos are produced from the decays of particles resulting from interactions of cosmic rays with Earth's atmosphere. Production of electron and muon neutrino is dominated by the following processes and its charge conjugate. (Figure 1.1)

$$\pi^+(or\ K^+) \to \mu^+ + \nu_\mu$$
$$\mapsto e^+ + \nu_e + \bar{\nu}_\mu$$

That gives an expected ratio of the flux of μ to the flux of e of about 2. Of course this is approximate as the actual ratio depends on energy and to some extent angle and position. Vertically downward-going neutrinos travel about 15 km while vertically upward-going neutrinos travel about 13,000 km before interacting in the detector. Because of good geometrical symmetry of the earth, we can expect up-down symmetry of neutrino flux. In the atmospheric neutrino analysis [2-5], however, a significant deficit of atmospheric muon neutrino interactions depending on zenith

angle were observed compared to the expectation and it was interpreted as neutrino oscillation. Thanks to wide ranges of L and E_ν, which atmospheric neutrinos undergo, we can measure the neutrino oscillation parameters, Δm^2 and $\sin^2 2\theta$. This thesis reports on the atmospheric neutrino analysis observed in Super Kamiokande.

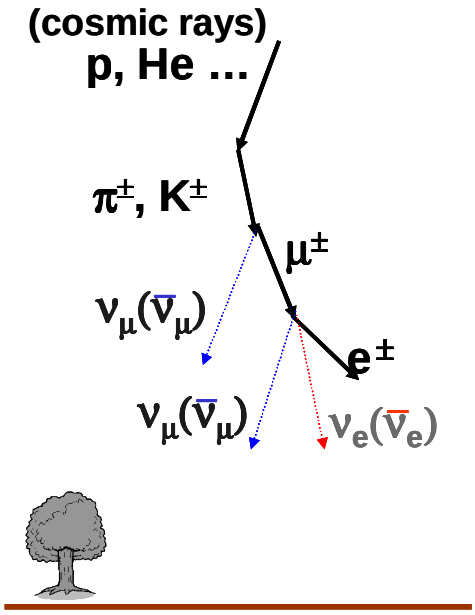

Figure 1.1 Process of atmospheric neutrino production in the earth's atmosphere.

1.4 Detection method of atmospheric neutrino in Super Kamiokande

Super-Kamiokande (also called Super-K or SK) is a 50 kiloton water Cherenkov detector. Figure 1.2 shows a cut-away diagram of the Super-Kamiokande detector (The detail description of Super Kamiokande detector is given in Chapter 2). Atmospheric neutrinos are detected in two ways in Super-K. The low energy

neutrinos from 100 MeV to 10 GeV are observed via the following charged current interactions with nuclei in the water.

$$\nu + N \rightarrow l + N'$$

Where, N and N' are the nucleons, l is the lepton.

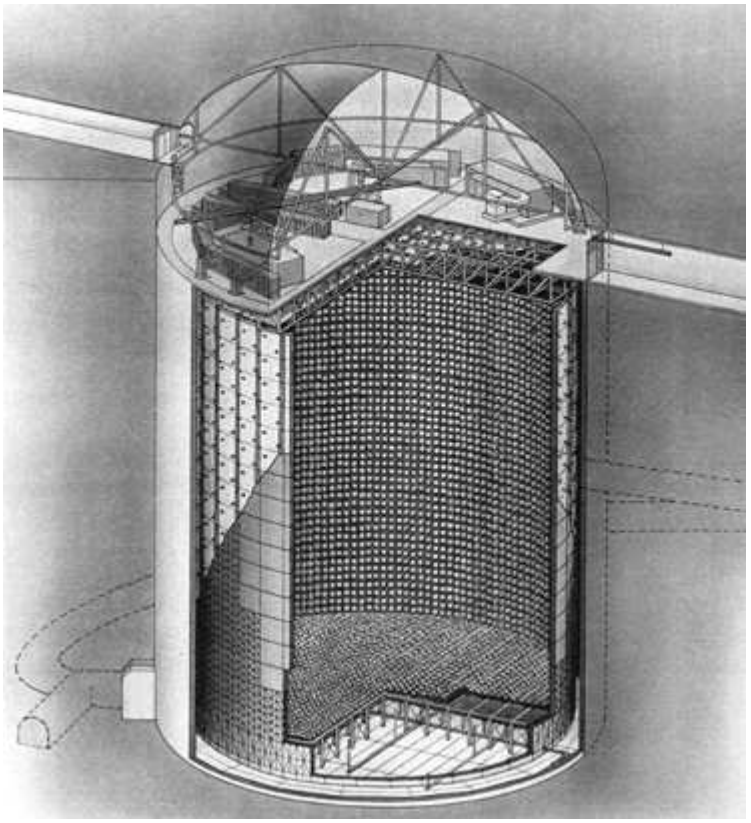

Figure 1.2 A cut away diagram of Super Kamiokande detector.

The flavor of neutrino is identified by the flavor of the lepton. This charged lepton generates Cherenkov light, which is detected by the PMTs installed on the wall of

Super-K. Another way of atmospheric neutrino detection is for high energy muon neutrinos. High energy ν_μ can undergo charged current interactions with the rock surrounding the detector and then produce high energy muons, which enter the detector. This muon is also observed via Cherenkov light by PMTs in Super-K.

Cherenkov radiation is emitted when charged particles pass through matter with a velocity exceeding the velocity of light in the medium,

$$v > v_i = c / n$$

where, n = refractive index of the medium, c = velocity of light and v_i = threshold velocity.

For a particle traveling faster than light, the wave-fronts do overlap, and constructive interference is possible and this leads to emit visible light known as Cherenkov radiation (Figure 1.3).

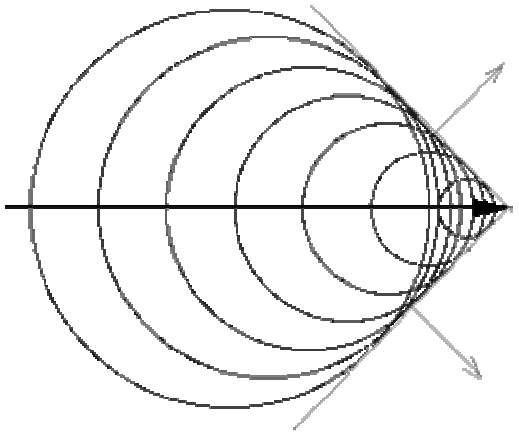

Figure 1.3 Cherenkov radiation is emitted when a particle travels faster than the speed of light in the medium.

The threshold energy corresponding to this threshold velocity is 0.768 MeV for electron and 158.7 MeV for muon. Cherenkov light is emitted under a constant angle θ with the particle trajectory, given by

$$\cos\theta = \frac{1}{\beta n}$$

Where β = v/c

When this cone of Cherenkov light reaches the wall of the detector, it forms a ring pattern. The PMTs measure the arrival time of the light and its photon yield. Figure 1.4 shows an event display of neutrino event detected via Cherenkov light in Super Kamiokande detector.

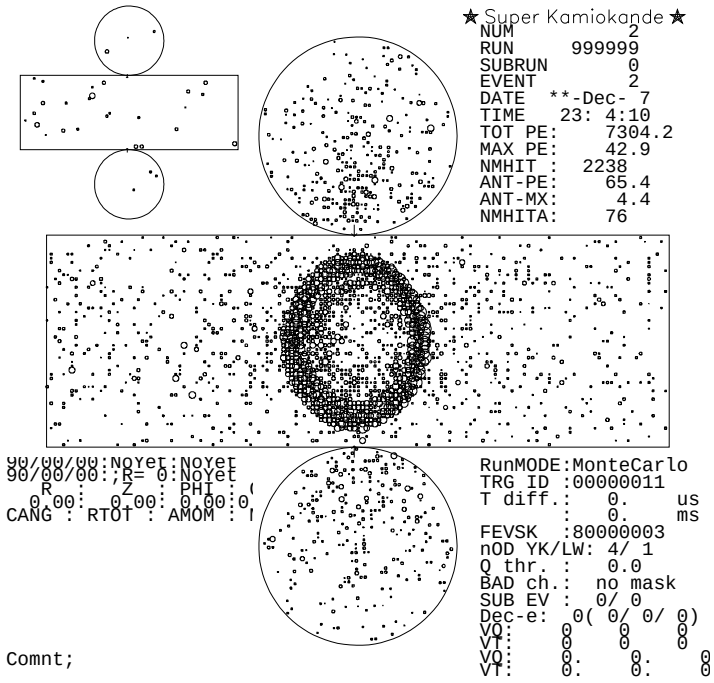

Figure 1.4 A muon neutrino event forming a ring pattern of Cherenkov light. in the Super Kamiokande detector.

Chapter 2

Super Kamiokande Detector

Super-Kamiokande, a 50 kiloton water Cherenkov detector is located in the Mozumi mine of the Kamioka Mining Company in Gifu prefecture, Japan, under the peak of Mt. Ikenoyama, providing a rock overburden of 2,700 meter-water-equivalent. Super-K consists of two concentric, optically separated water Cherenkov detectors.

Super-Kamiokande began to take data in April, 1996. It was shut down for maintenance and upgrade in July, 2001. This 1996-2001 running period is referred to as Super-Kamiokande-I. During filling the water to start Super Kamiokande-II, in November, 2001, an apparent cascade of implosions triggered by a single photomultiplier (PMT) implosion destroyed over half of the PMTs installed in the detector. In 2002, the detector was reconstructed using about 5,000 PMTs (the original number of PMTs used in Super-K is 11,146) encased in acrylic covers to avoid a similar accident. This partial reconstruction was done quickly in only a year. Super Kamiokande-II was operated from Dec. 2002 to Oct. 2005 with half the original density of PMTs. After termination of Super Kamiokande-II, the long awaited full reconstruction of the detector began. In June, 2006, the detector's third phase, Super Kamiokande-III, will start to take data.

2.1 Detector

2.1.1 Tank

The outer shell of the detector is a cylindrical stainless steel tank, 39 m in diameter and 42 m in height. Figure 2.1 shows a cross section view of Super Kamiokande. The tank is self-supporting, with concrete backfilled against the rough-hewn stone walls to counteract water pressure when the tank is filled with water. The capacity of the tank exceeds 50 ktons of water. A cylindrical PMT support structure divides the tank into two distinct, optically isolated volumes. The structure has inner dimensions, 33.8 m (diameter) by 36.2 m (height), defining the inner detector (ID) which contains 32 ktons of water and was viewed by inward-facing 50 cm PMTs (Hamamatsu R3600). Approximately 2.5 m distance remains on all outside of the support structure. This outside region defining outer detector (OD), serves as an active veto counter against incoming particles as well as a passive shield for neutrons and gamma rays from the surrounding rocks. OD was instrumented with 1,885 outward-facing 20 cm PMTs (Hamamatsu R1408) in both Super Kamiokande-I and Super Kamiokande-II. The two detector volumes are isolated from each other by two light-proof sheets on both surfaces of the PMT support structure. The 55 cm thick support structure comprises dead space from which light in principle cannot escape. Therefore, any interaction in that space cannot be detected. The OD PMTs were mounted in water-proof housings which effectively block light from the dead space.

2.1.2 PMTs

A 50 cm ID PMTs used in this experiment is depicted in Figure 2.2. The bialkali (Sb-K-Cs) photocathode has peak quantum efficiency of about 21% at 360 nm-400 nm as shown in Figure 2.3. The collection efficiency for photoelectrons (pe) at the first dynode is over 70%. The transit time spread for a 1 pe signal is 2.2 ns. The

average dark noise rate at the 0.25 pe threshold is about 3 kHz in Super Kamiokande-I. The ID PMTs were operated with

gain of 10^7 at a supply high voltage ranging from 1700 to 2000 V. The neck of each PMT was coated with a silver reflector to block external light.

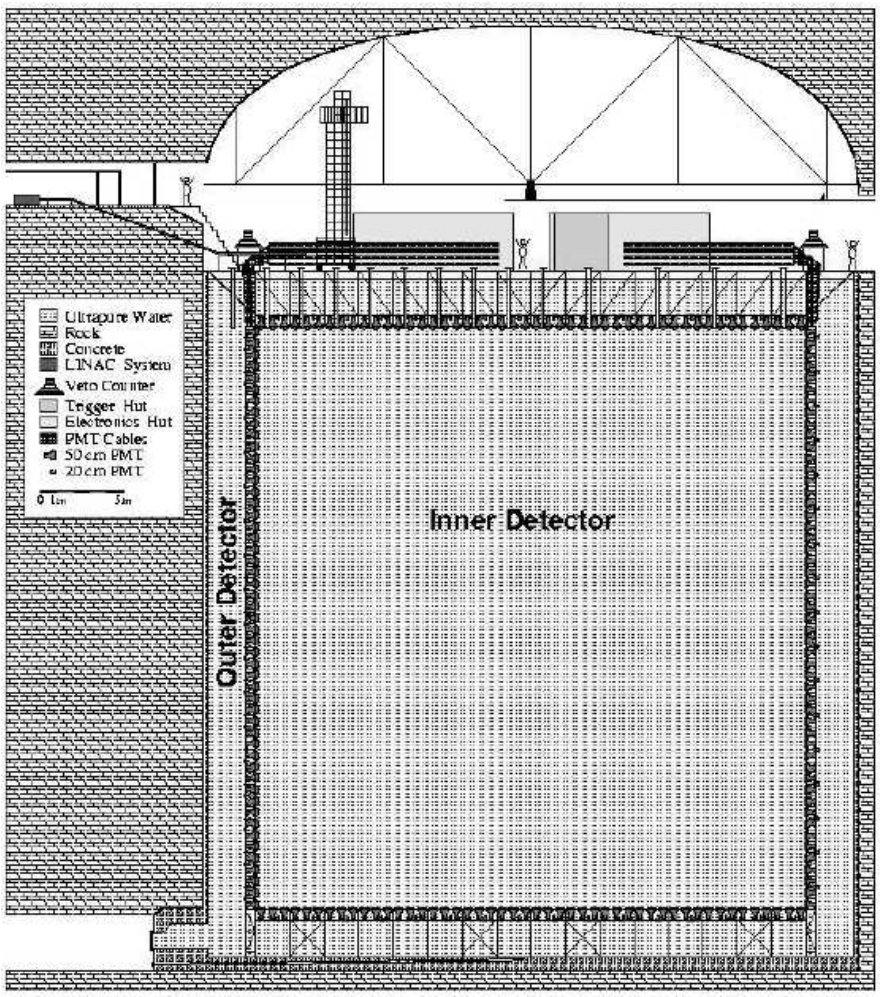

Figure 2.1 A cross section view of Super Kamiokande detector.

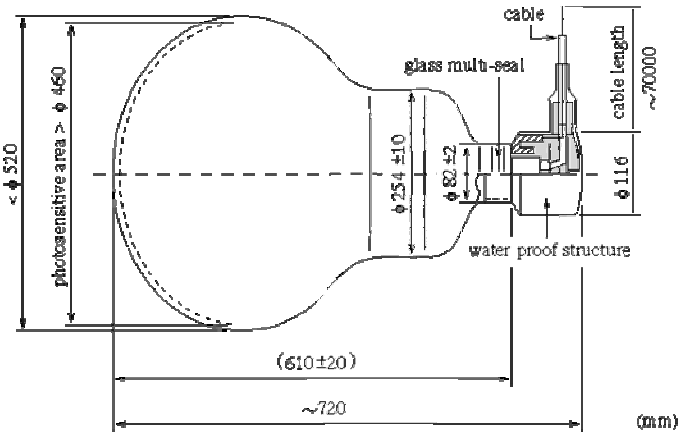

Figure 2.2 Schematic view of a 50 cm PMT used in inner detector of Super Kamiokande.

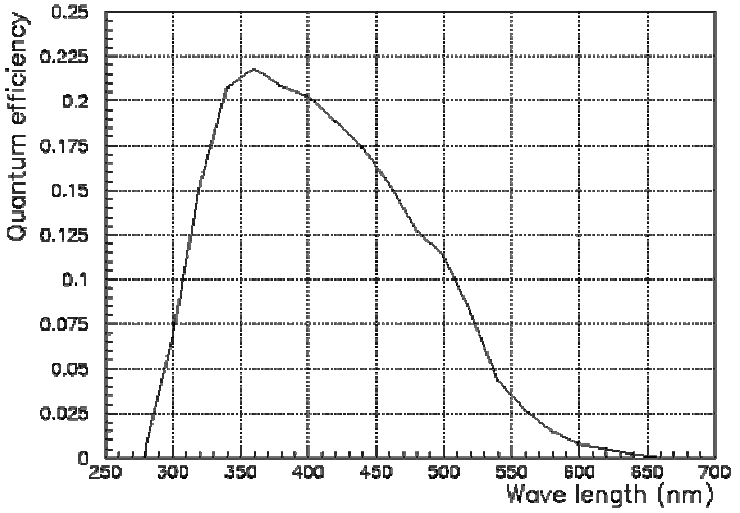

Figure 2.3 Quantum efficiency of the photocathode as a function ofwavelength.

2.1.3 PMT support structure and others

Figure 2.4 shows a detail of the PMT support structure. All support structure components are stainless steel. The basic unit for the ID PMTs is a supermodule, a frame which supports a 3x4 array of PMTs. Each supermodule has two OD PMTs attached on its back side. Opaque black plyethylene telephthalate sheets cover the gaps between the PMTs in the ID surface. These sheets improve the optical separation between the ID and OD and suppress unwanted low-energy events due to residual radioactivity occurring behind the PMTs. Light collection efficiency in the OD is enhanced by wavelength shifting (WS) plates attached to each OD PMT. The WS plates are square acrylic panels, 60 cm on a side and 1.3 cm thick, doped with 50 mg/ℓ of bis-MSB. The WS plates function by absorbing UV light, and then re-radiating photons in the blue-green, better matching the spectral sensitivity of the PMT's bialkali photocathode. The light collection of the PMT plus WS unit is improved over that of the bare PMT by about a factor of 1.5. To further enhance light collection, the OD volume is lined with a reflective layer made from Type 1073B Tyvek manufactured by DuPont. This inexpensive and very tough paper-like material has excellent reflectivity in the wavelength range in which PMTs are most sensitive, especially at short wavelengths. Measured reflectivities are on the order of 90% for wavelengths in excess of 400 nm, falling to 80% at about 340 nm. The presence of this liner allows multiple reflections of Cherenkov light, which minimizes the effects of dead PMTs, given their coarse spacing in the OD. Cherenkov light is spread over many PMTs, reducing pattern resolution but increasing overall detection efficiency.

The average geomagnetic field is about 450 mG and is inclined by about 45 with respect to the horizon at the detector site. The strength and uniform direction of the geomagnetic field could systematically bias photoelectron trajectories and timing in the PMTs. To counteract this, 26 sets of horizontal and vertical Helmholtz coils are arranged around the inner surfaces of the tank. With operation of these coils, the average field in the detector is reduced to about 50 mG. The magnetic field at various PMT locations were measured before the tank was filled with water.

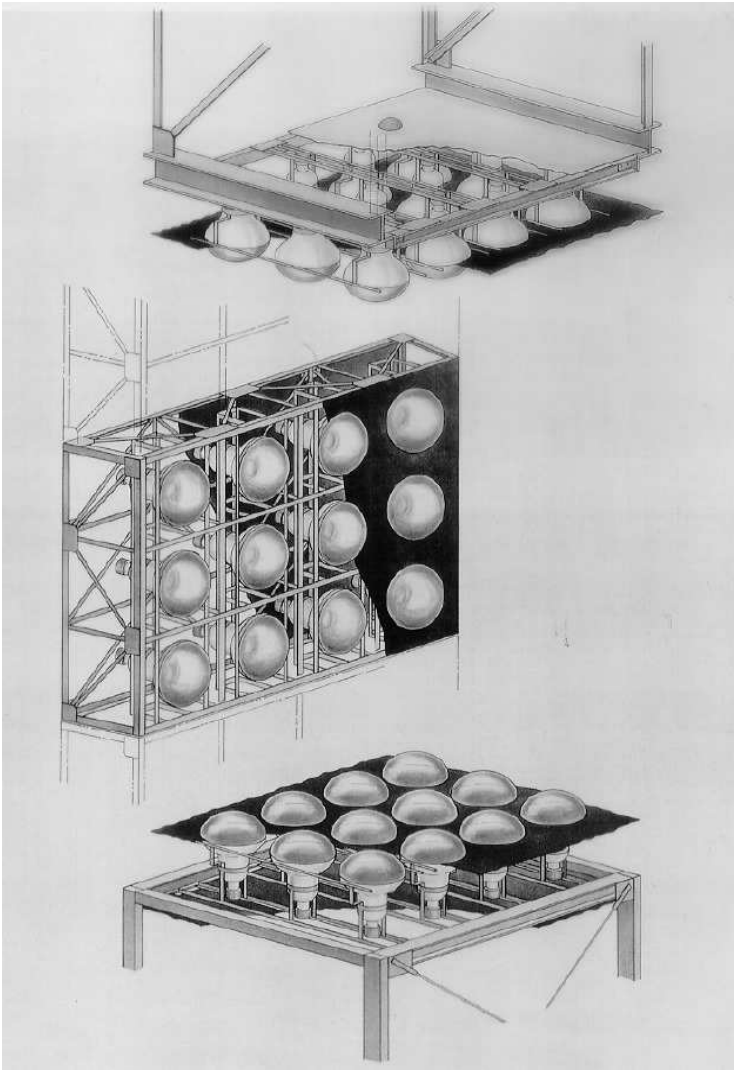

Figure 2.4 Schematic view of PMT support structures.

2.1.4 Inner detector electronics and data acquisition system

ID PMT signals are processed by custom built TKO modules called Analog-Timing-Modules (ATMs). The TKO (TRISTAN KEK Online) system was originally developed and built by KEK, and is optimized for front-end electronics where a large number of channels are to be handled. The ATM has the functionality of a combined ADC (Analog-to-Digital Converter) and TDC (Time-to-Digital Converter), and records the integrated charge and arrival time of each PMT signal. Signals from 12 PMTs are fed to an ATM board. Figure 2.5 shows a block diagram of the ATM board. The PMT signal into the current splitter is divided into four signals. One of them is fed to the discriminator with the threshold level for each channel set to -1 mV, which corresponds to 1/4 pe equivalent. When the PMT signal is above the threshold level, a "hit" signal with 200ns width and 15 mV pulse height is asserted on the ATM front panel. The HITSUM signal, which is used to generate the global trigger signal, is the analog sum of all these 15 mV/Channel pulses. At the same time, either of the split signals, A or B, is held by a QAC (Charge to Analog Converter), and a TAC (Time to

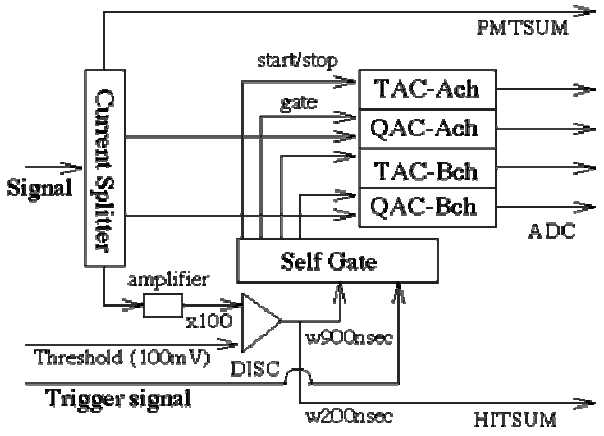

Figure 2.5 A block diagram of ATM board used for inner detector data acquisition.

Analog Converter) starts to integrate constant current. If a global trigger is received, the information in the TAC/QAC is digitized and stored in internal memory buffers. Since, for each channel, TAC integration is started by the PMT signal itself, the arrival time of the signal can be inferred from the value of the integrated charge. A "self gate" chip generates start/stop signals for the TAC, the gate signal for QAC, and clear signals for both. Output signals from the TAC/QAC are fed to an ADC and digitized. There are two TACs and QACs for each channel so that events in rapid succession, such as muon followed by its decay electron, can be processed without dead-time.

Figure 2.6 shows a schematic view of the inner detector data acquisition (ID DAQ) system. There are total 946 ATM modules, located in four "quadrant huts". ATMs record ADC/TDC data of each PMT above threshold when a global trigger signal is asserted by the VME TRG (TRiGger) module. The global trigger signal and event number information generated in the TRG module, are distributed to all ATMs via 48 GONG (Go/NoGo) modules.

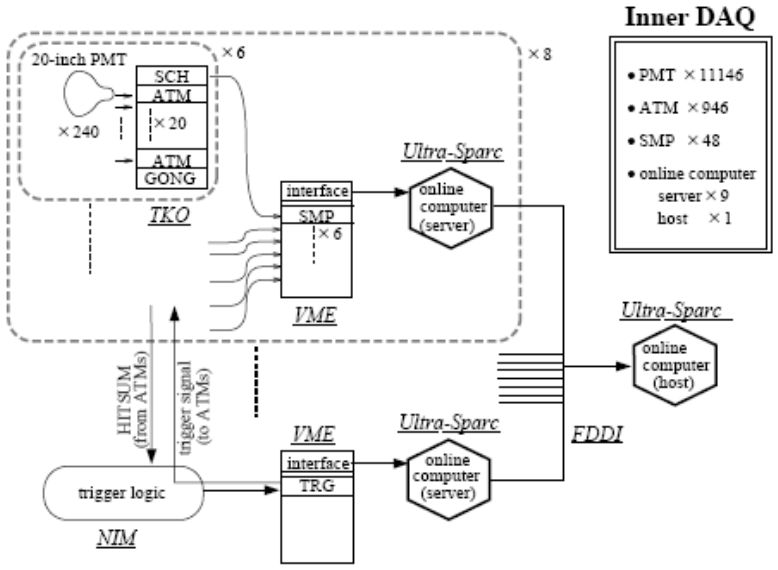

Figure 2.6 The data acquisition system for the inner detector.

2.1.5 Outer Detector Electronics and Data Acquisition

A block diagram of the OD data acquisition (OD-DAQ) system is shown in Figure 2.7. As with the inner detector, signals from the PMTs are processed and digitized in each of 4 quadrant electronics huts. From there, the signals are picked off, digitized and stored. As in the ID, local HITSUM pulses are formed in each quadrant hut and sent to the central hut, where their analog sum creates an OD trigger signal when the OD HITSUM threshold is exceeded. Figure 2.7 illustrates the data flow in a quadrant hut as well as the overall data flow. When a trigger from any source occurs, the data are passed out of the quadrant huts to the central hut for further processing. Once the PMT signals have been picked off, coaxial ribbon cables feed them to the custom charge-to-time conversion modules (QTC). The purpose of these modules is to measure the hit time and charge of the PMT pulse and convert it to a form which can be easily read and stored by the time-to-digital converters (TDCs). The output of the QTC modules is a logic pulse (ECL level) whose leading edge marks the hit arrival time and whose width represents the integrated charge Q of the PMT pulse.

2.2 Detector Calibration

2.2.1 Water Transparency Measurement

1) Indirect measurement with cosmic rays

The light attenuation length in water can be measured by using through-going cosmic ray muons. These muons are energetic enough to deposit almost constant ionization energy per unit path length (about 2 MeV / cm) independent of particle energy. This fact makes it possible to use these muons as a “constant” light source. The advantage of this method is that continuous and abundant samples of muons come without cost as we take normal data.

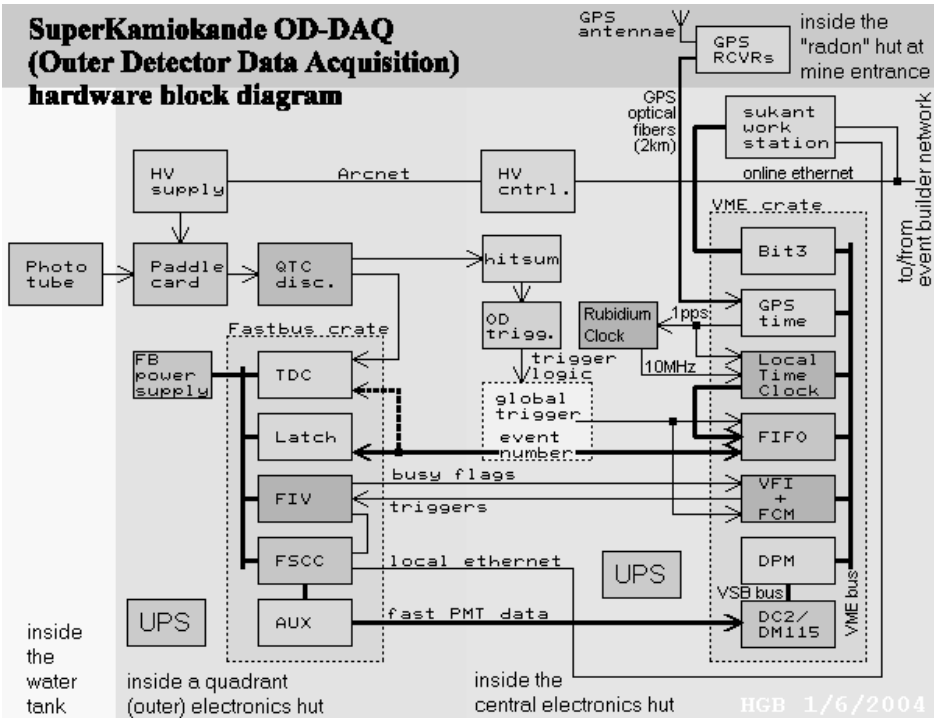

Figure 2.7 OD DAQ block diagram and data flow.

The disadvantage is that we cannot measure the transparency as a function of wavelength. However, since what we measure is the Cherenkov spectrum, this disadvantage is not necessarily a problem. Under the assumption that light reaching the PMTs is not scattered, the charge Q observed by a PMT is expressed by

$$Q = Q_0 \cdot \frac{f(\theta)}{\ell} \cdot \exp\left(-\frac{\ell}{L}\right)$$

Where ℓ is the light path length, L the effective attenuation length, Q_0 a constant and $f(\Theta)$ the relative photo-sensitive area, which depends upon the incidence angle Θ of the light on the PMT, as shown in Figure 2.8. Figure 2.9 is $Q\ell / f(\theta)$ as a function of the path length ℓ together with the best fit in the form of the function def-

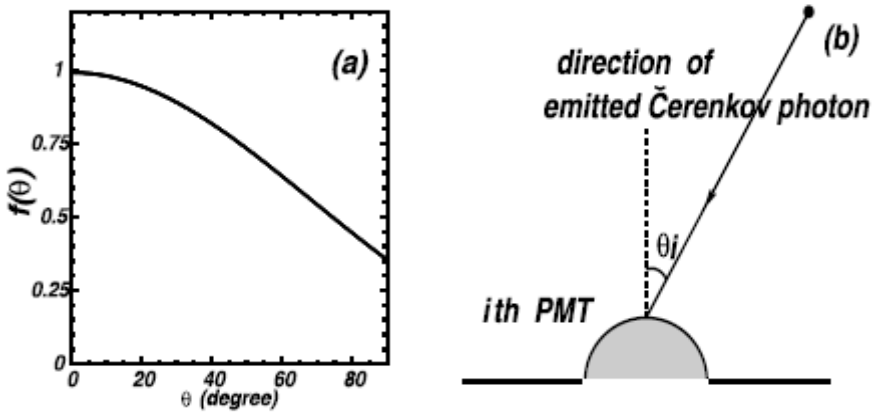

Figure 2.8 Relative photo-sensitivity. (a) Measurement result, (b) Definition of the incident angle.

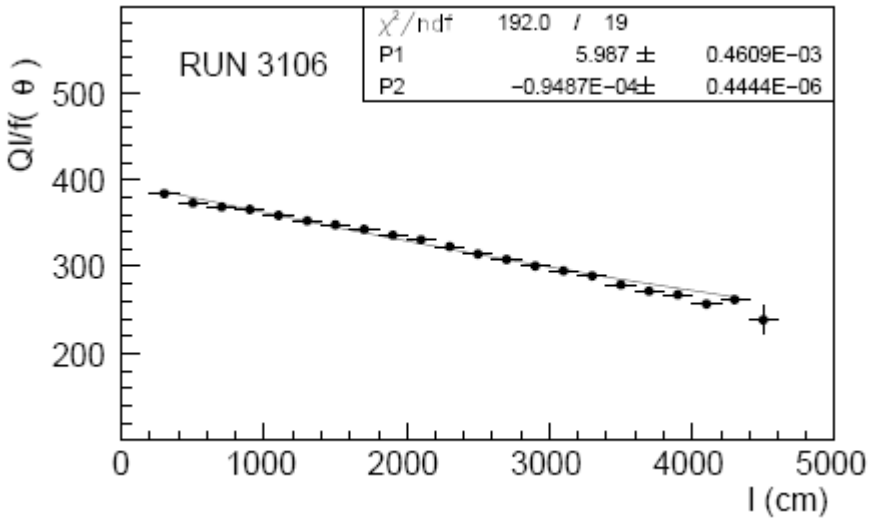

Figure 2.9 Effective charge observed as a function of the path length.

-ined above. The resulting attenuation length is found to be 105.4±0.5 m. As the data sample for this measurement is accumulated automatically while we take normal data, it is possible to continuously monitor the attenuation length as a function of time. Figure 2.10 shows the attenuation length changes with time, which are correlated with water quality. Such time variations in the attenuation length are corrected in analysis from the time series of calibration data.

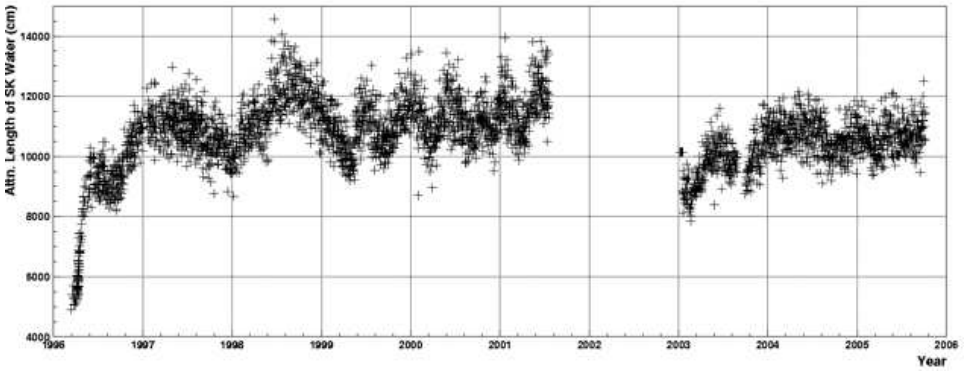

Figure 2.10 Time variation of the water attenuation length measured by through-going cosmic ray muon.

2) Light Scattering Measurement with laser

To measure the scattering and absorption parameters separately, a combination of dye and N_2 lasers of wavelengths 337, 371, 400, 420 nm are used as light sources. In Super Kamiokande-I, the laser beam is brought into the top of the detector via optical fibers. Each laser fires every 6 second during normal data taking. Figure 2.11 shows a schematic view of the laser calibration setup and a typical event of laser light. A cluster of hits at the bottom of the tank is due to unscattered photons. The remaining hits, in barrel and top PMTs, are due to photons scattered in the water or reflected by the bottom PMTs and black sheet. The total charge in the cluster of bottom hits is use-

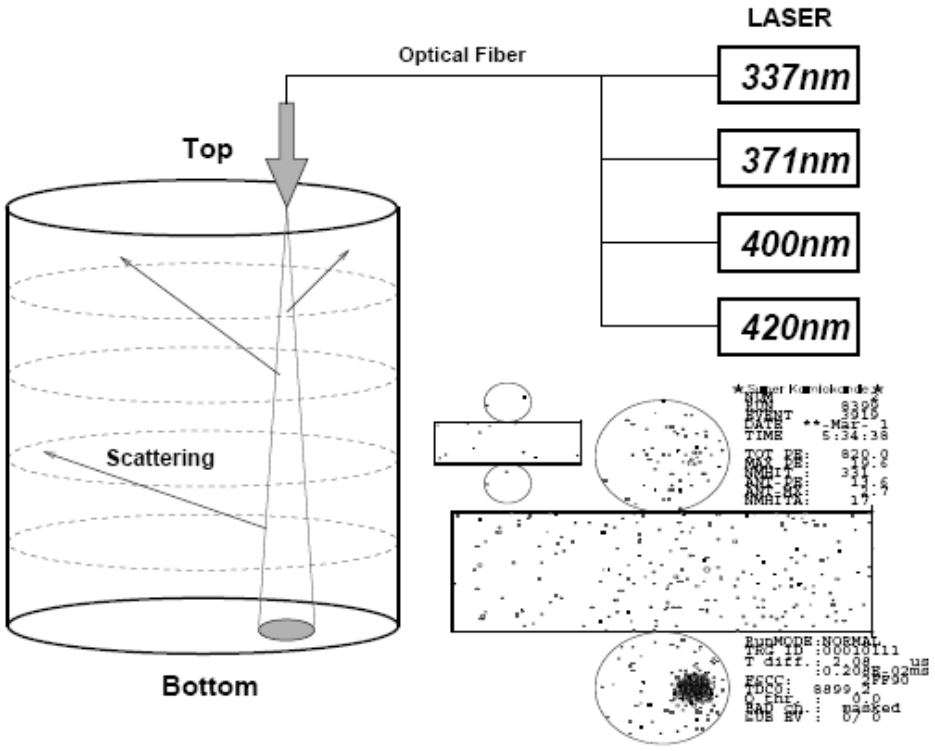

Figure 2.11 Laser system for water scattering and absorption parameter measurement and its typical event display.

-d for normalization factor as a reference of light intensity. Figure 2.12 show the detail view of the arrangement of laser firing setup. The direction of light fired by each laser is turned by half mirror and finally go to the fiber bundle where 7 fibers are connected. One of them is the fiber brought into the top of detector. 4 of them are brought to the two monitoring PMTs and two monitoring APDs. The other two remained spare. The intensity of the each laser is adjusted by ND filter. The two diffusers are put in front of the fiber bundle to diffuse light randomly. Figure 2.13 shows distributions of photon arrival times at the top PMTs. In the upper plot, the peak near 730 ns is from scattered photons, and the second peak represents reflected photons at the bottom of the detector. For the Monte Carlo, the total number of scattered photons is tuned using Rayleigh scattering parameters, and the shape of the arrival time distribution is used to adjust the absorption parameters. The lower plot in

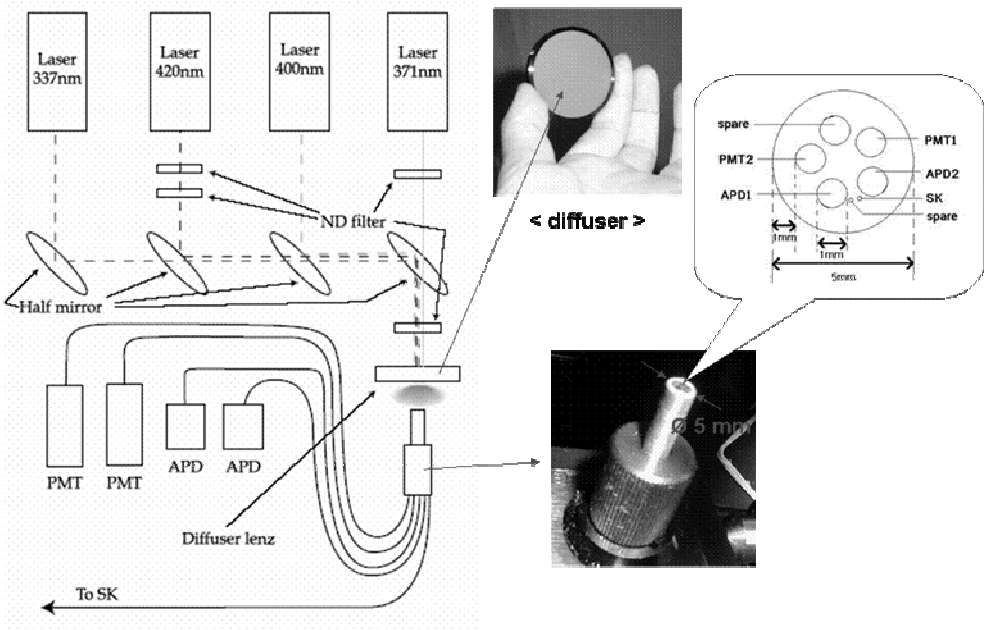

Figure 2.12 The detail view of the arrangement of laser firing setup.

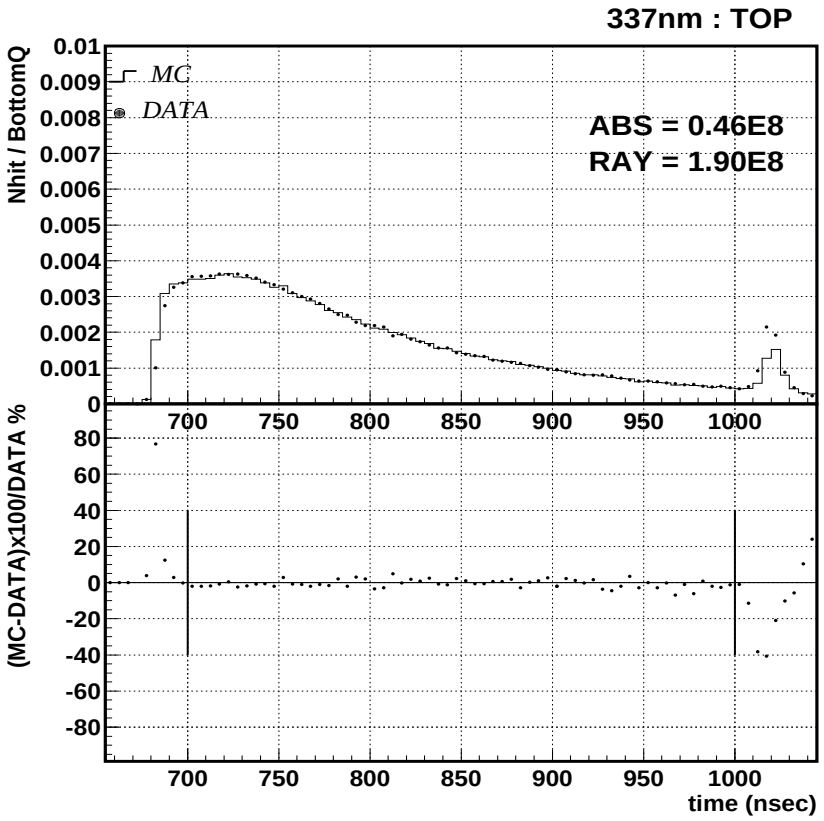

Figure 2.13 The upper plot is the photon arrival time distribution of the top PMTs. Dots is data and line is Monte Carlo. The lower plot is the ratio, (MC-DATA)/DATA.

Figure 2.13 shows the time dependence of the ratio between Monte Carlo and data, which agree within ~2%.

Using the measured absorption and scattering parameters, the light attenuation length of water is calculated using the following equation.

$$L_{atten} = \frac{1}{\alpha_{abs} + \alpha_{scatt}}$$

Figure 2.14 compares the time variation of the light attenuation length measured by the 420 nm laser and cosmic ray muon during Super Kamiokande-I period. The result from cosmic ray muon is with average Cherenkov spectrum so it does not agree with the one from the laser system. However, we can see the tendency of time variation is consistent between the two measurements.

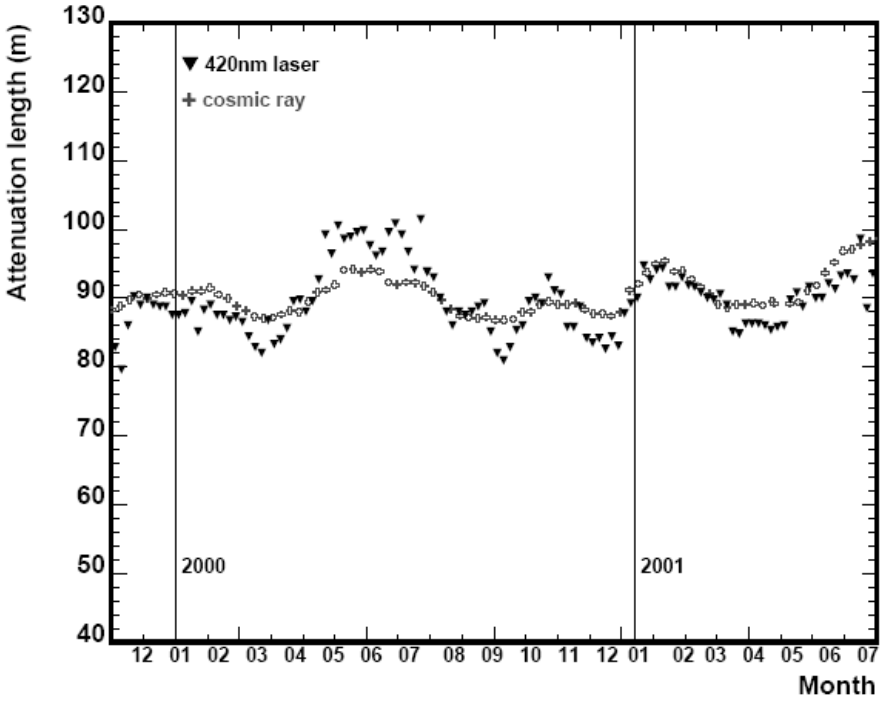

Figure 2.14 Comparison of time variation of light attenuation length measure by laser system and cosmic ray muon.

3) Upgraded Light Scattering Measurement system in Super Kamiokande-II

Super Kamiokande is a large water tank. So it was questioned if the water quality depends on positions in the tank. Actually a clue for the position dependence is observed in the detail analysis with the laser system in Super Kamiokande. However we were not sure whether it is due to position dependence of the water quality or to other effects. To investigate the position dependence of the water quality, light injectors (LI) similar to the one used in Super Kamiokande-I were installed at the different 7 positions of the detector and started to inject laser with the beginning of Super Kamiokande-II. Figure 2.15 shows the position of light injector (LI) installed in the tank. The LI used in Super Kamiokande-I was named as Oldtop LI, the new injector installed at the top as Newtop LI and other LIs were named as B1, B2, B3, B4, B5 and Bottom LI according to their positions. Figure 2.16 shows the diagram of the whole light scattering measurement system used in Super Kamiokande-II. To input laser beam to different 7 fibers connected to different 7 positions in the tank, one laser beam source is moved by step motor in 'optical SW' depicted in Figure 2.16. The step motor is controlled by software through serial communication (RS-232). Figure 2.17 shows the inside of the 'optical SW'.

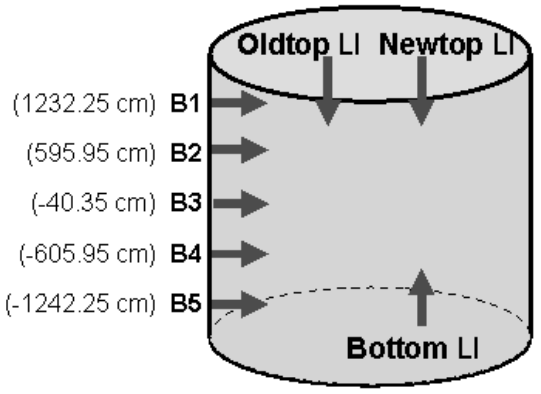

Figure 2.15 Positions of light injectors at the detector.

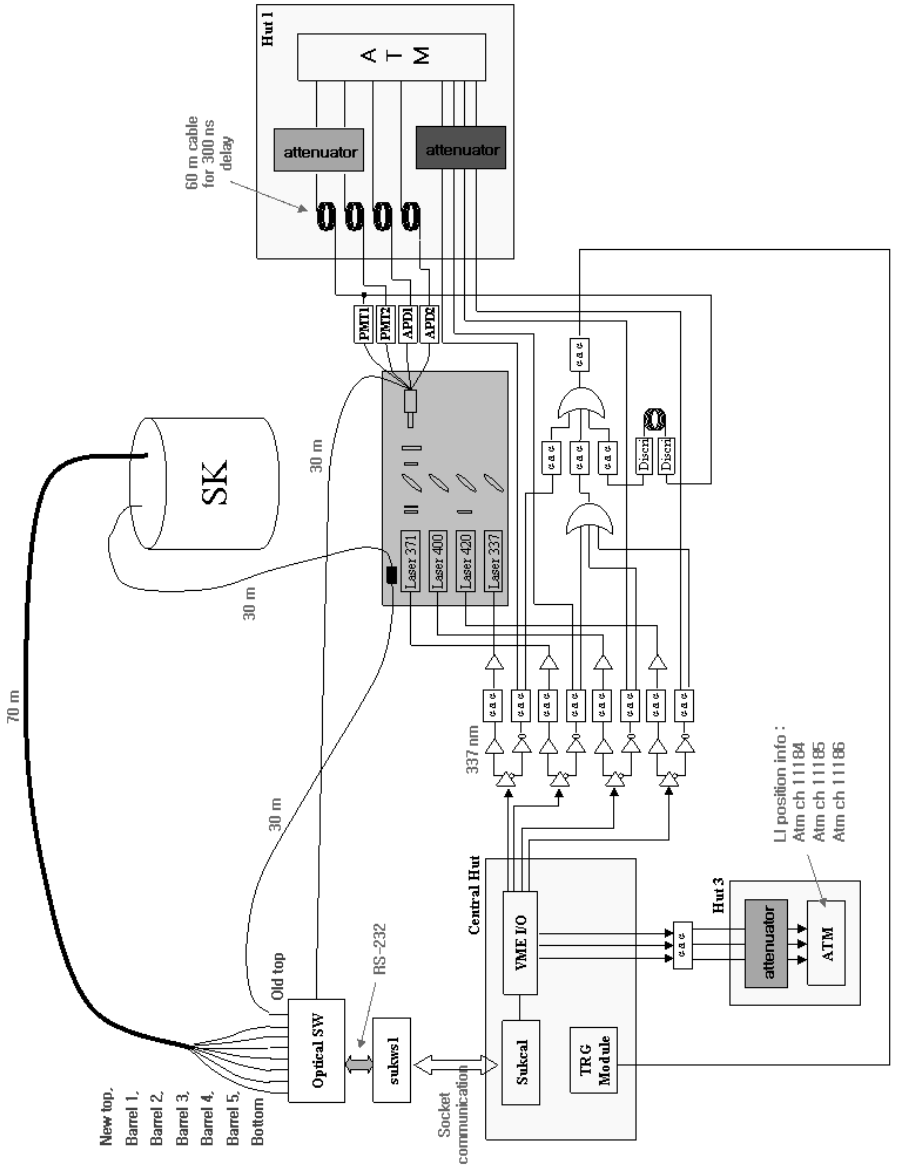

Figure 2.16 Diagram of whole light scattering measurement system used in Super Kamiokande-II.

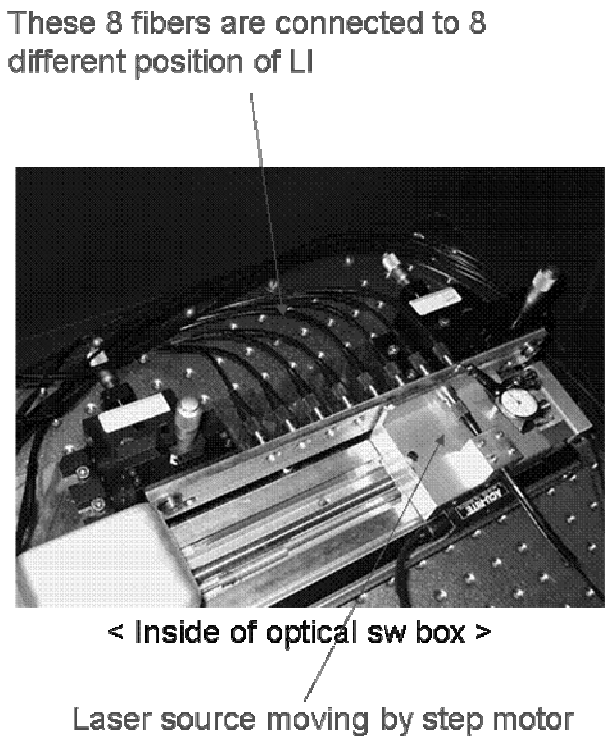

Figure 2.17 'Optical SW (switch)', which distribute laser light into 8 different fibers mechanically by step motor.

To monitor the water quality, the value, 'Nhit/Q' was used, where 'Nhit' means the number of hit PMT within a region defined around the LI and 'Q' is the total charge deposited at Super Kamiokande used as normalization factor. In SK-I, the charge in the bottom cluster was used as the normalization factor but in SK-II, total charge was used because total charge is less affected by possible change of beam shape or beam direction and their imperfect reproduction in Monte Carlo (MC). The region to calculate 'Nhit' was defined radius 10 m around LI in case of barrel LI and whole top (bottom) region is used for top (bottom) LI. Figure 2.18 explain how to calculate 'Nhit' visually. Another systematic effect to the value,'Nhit/Q' is from light intensity. We normalized the number of hit by total charge to compensate light intensity depen-

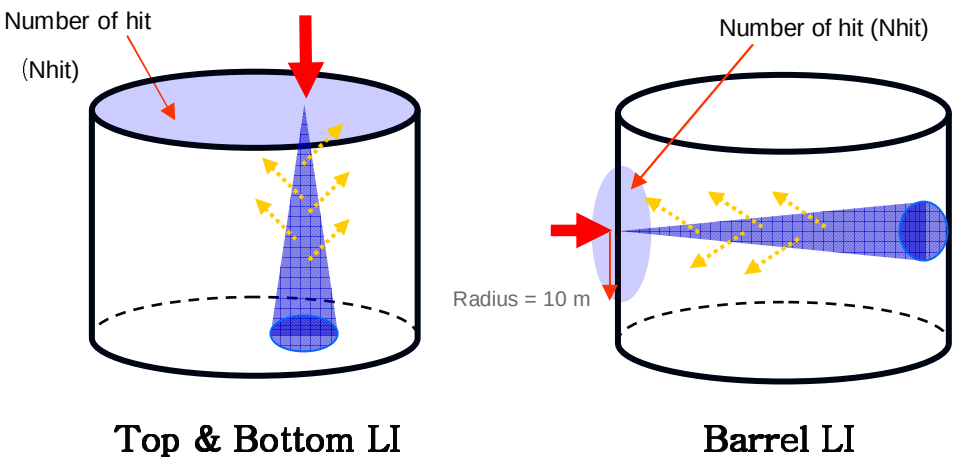

Figure 2.18 How to calculate Number of hit (Nhit) for each LI for monitoring water quality.

-dence of 'Nhit'. However, even 'Nhit/Q' has light intensity dependence slightly. Figure 2.19 shows 'Nhit/Q' as a function of light intensity estimated by Monte Carlo with oldtop LI for 337 nm laser. The tendency is that low intensity gives high 'Nhit/Q' and high intensity low 'Nhit/Q'. The reason why 'Nhit/Q' depends on light intensity was investigated and it was found that the multiple hits near LI cause this trouble. Figure 2.20 shows spatial distribution of 'number of hit' for three different intensity (that is, normal intensity, three times larger intensity than normal intensity and three times lower intensity) made with Monte Carlo of oldtop LI. Vertical axis is the number of hit PMTs (Nhit) in the top region of the tank normalized by the intensity and horizontal axis is the distance from oldtop LI. We can see the discrepancy near LI, which is due to multiple hits. To reduce this multiple hits effect, we decided not to use PMTs within 2 m from LI in the analysis. Figure 2.21 shows 'Nhit/Q' as a function of light intensity similar to Figure 2.19 but without PMTs within 2 m from LI. We can see the light intensity dependence was reduced by removing PMTs near LI.

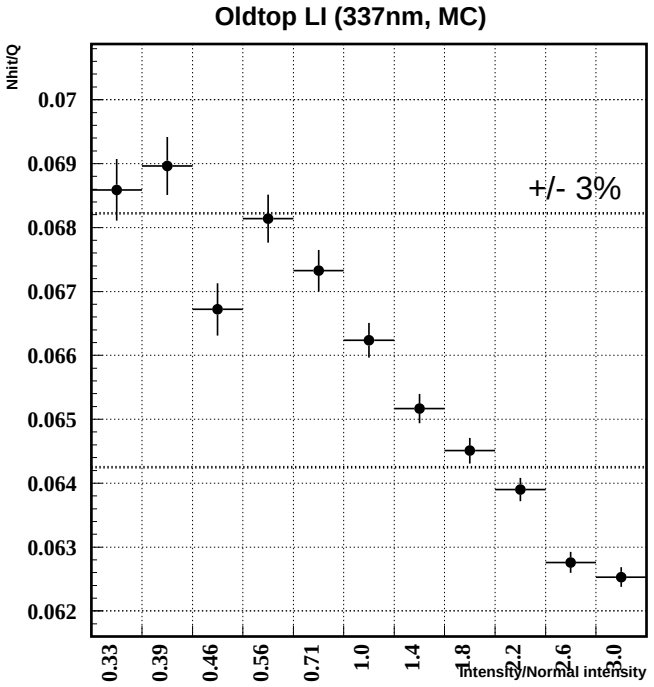

Figure 2.19 'Nhit/Q' as a function of light intensity. Horizontal axis is the ratio of light intensity to normal intensity, which was used in Monte Carlo.

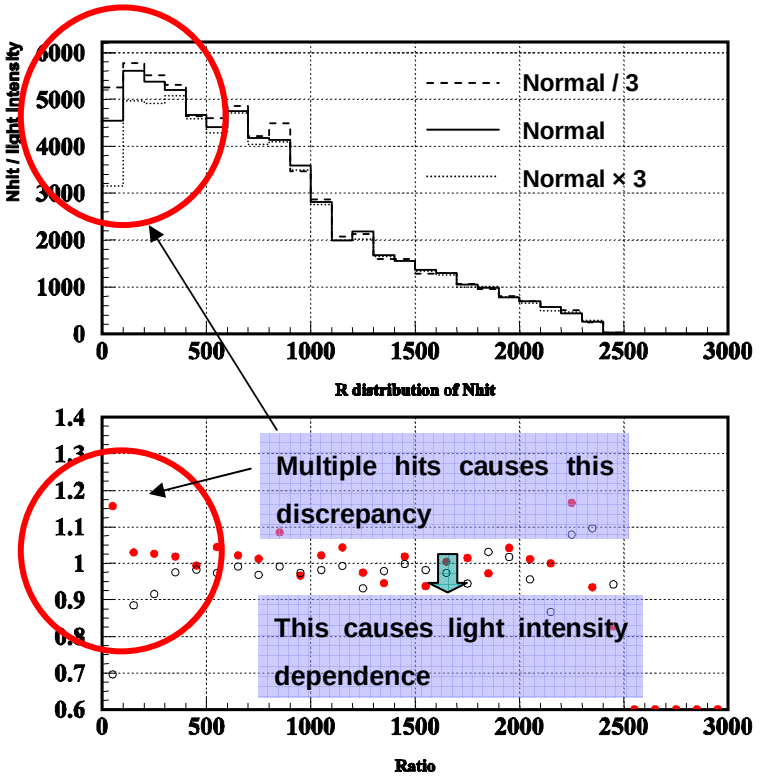

Figure 2.20 Upper plot is the spatial distribution of 'number of hit' for 3 different intensity made with Monte Carlo of oldtop LI. Vertical axis is the number of hit PMTs (Nhit) in the top region of the tank normalized by the intensity and horizontal axis is the distance from oldtop LI. Bottom plot is the ratio between lower intensity to normal (filled circle) and larger intensity to normal (open circle).

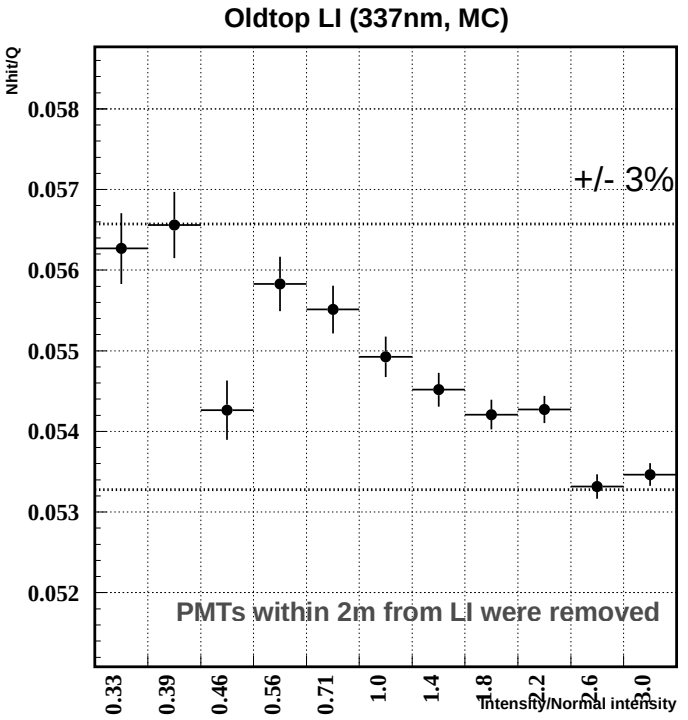

Figure 2.21 'Nhit/Q' as a function of light intensity without PMTs within 2 m from LI.

In the upgraded system of SK-II, each laser fires every 1 sec during normal data taking. This is more frequent than 6 sec of SK-I because we should inject light in total 8 positions in SK-II. To analyze the laser data, every 10 days data were combined and 'DATA(Nhit/Q) / MC(Nhit/Q)' was compared for each 7 LI to investigate Z (Z is the direction along the height of the detector) dependence of water quality. To estimate systematic error between LIs, '100×DATA(Nhit/Q) / MC(Nhit/Q)' was compared between oldtop LI and newtop LI. Systematic error between different wavelength of laser was also estimated by comparing '100×DATA(Nhit/Q) / MC(Nhit/Q)' between four wavelength lasers for one LI. Figure 2.22 (a) shows the distribution of 'Oldtop LI – newtop LI' for '100×DATA(Nhit/Q) / MC(Nhit/Q)' and (b) shows the distribution of '(Each wavelength) – (Mean of 4 wavelength)'. The 1 σ denoted in the

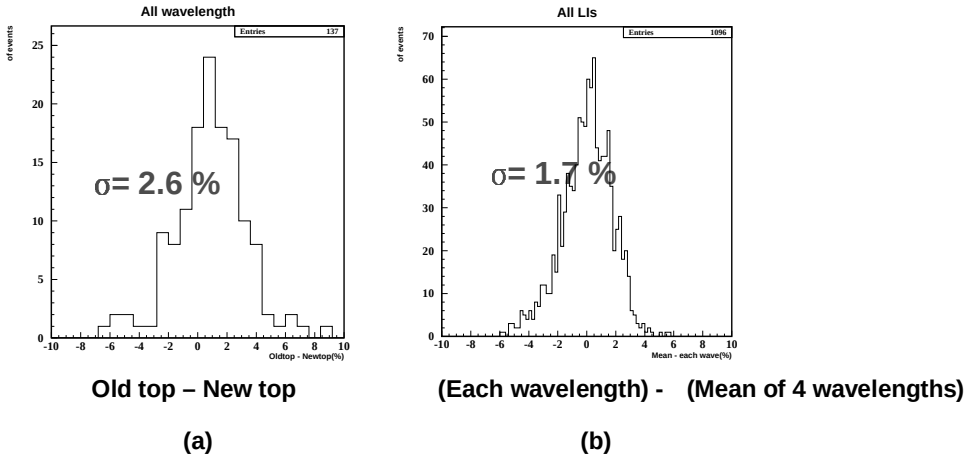

Figure 2.22 Left plot (a) is the distribution of 'Oldtop LI – newtop LI' for '100×DATA(Nhit/Q) / MC(Nhit/Q)' and Right plot (b) the distribution of '(Each wavelength) – (Mean of 4 wavelength)'.

figure is the one estimated from the distribution in the plot, which means it is from combination of a couple of variables. If we calculate 1 σ for one variable, they are 1.9 % and 2.1 % for 'Oldtop LI – newtop LI' and '(Each wavelength) – (Mean of 4 wavelength)', respectively.

Figure 2.23 shows DATA(Nhit/Q) / MC(Nhit/Q) obtained for each LI for various period of Super Kamiokande-II. According to the result in Figure 2.23, Z-dependence of water quality is not clearly seen in Super Kamiokande. However, we are trying to reduce systematic errors of the laser system to see Z-dependence, which may be hidden under the systematic effect.

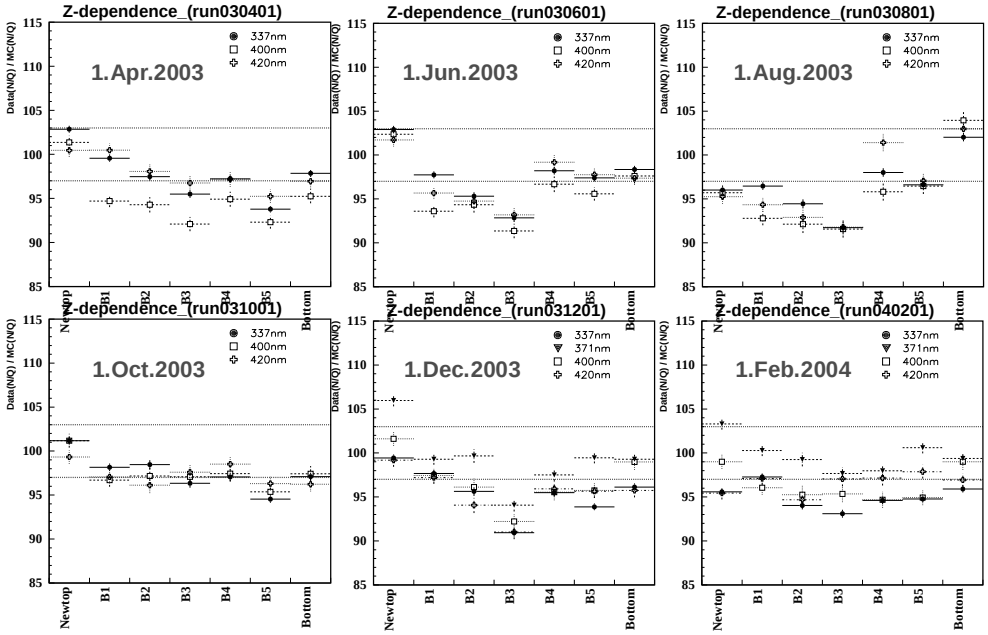

Figure 2.23 DATA(Nhit/Q) / MC(Nhit/Q) obtained for each LI for various period of Super Kamiokande-II to investigate position dependence of the water quality.

2.2.2 Relative Gain Calibration

The high voltage of each PMT is set to provide approximately equal gain for all PMTs in the Super-Kamiokande detector. Each PMT came with a nominal high voltage value, which was specified by Hamamatsu Phonics just after its production, using three calibration light sources : a DC light source, a Xe-lamp pulsed light source, and a light source at the single pe level. However, because of possible long-term drift in the factory calibration system, which may have caused a systematic difference between tubes manufactured at different times, all PMTs had their gain re-calibrated. Normalized Relative gain was measured by the system shown in Figure 2.24. Light generated by a Xe lamp is passed through an ultraviolet (UV) filter and injected into a scintillator ball via an optical fiber. The scintillator ball is an acrylic ball with BBOT

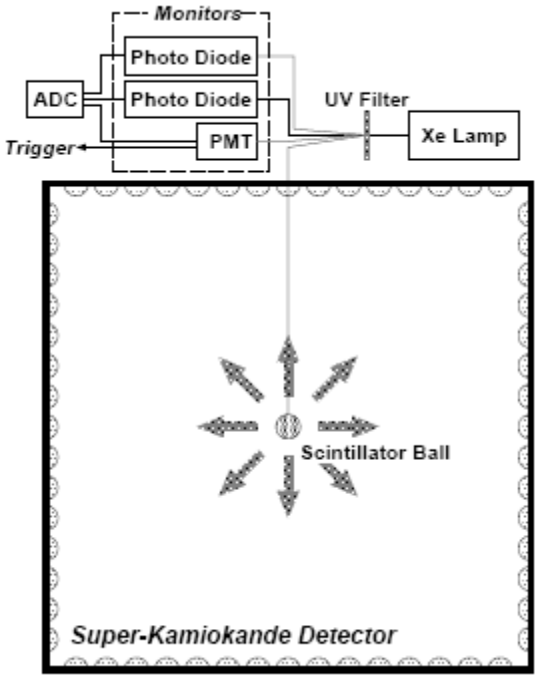

Figure 2.24 The relative gain measurement system.

(2, 5-bis(5'-tert-butyl-2-benzoxazolyl)thiophene) wavelength shifter and MgO powder diffuser. BBOT absorbs UV light and emits light with a peak at 440 nm, which is in the sensitive region of the PMTs used for Super-Kamiokande for Cherenkov light detection. In this measurement, each PMT detects a few tens of pe. The intensity of the primary UV light is monitored by two photodiodes and one PMT. The output of the monitor PMT is also used for triggering. The relative gain G_i of the i-th PMT is obtained by:

$$G_i = \frac{Q_i}{Q_0 f(\theta)} \cdot \ell_i \cdot \exp\left(\frac{\ell_i}{L}\right)$$

where Q_i is the observed charge by the PMT, Q_0 a constant, L the effective light attenuation length, ℓ_i the distance from the light source to the PMT and $f(\Theta)$ the relative photo-sensitivity as a function of the incident angle of light a on the PMT defined in Figure 2.8. The high voltage value for each PMT is set so that the "corrected Q" of each PMT is approximately the same as for all the others. Here, "corrected Q" is the pulse height corrected for light attenuation, acceptance of the PMT, and uniformity of the scintillator ball. It is further normalized by the Xe monitor pulse height. This measurement is done for various positions of the scintillator ball and settings of the high voltage value. After the initial gain adjustment, long term stability of PMT gain was monitored using the same system. The absolute value of PMT gain cannot be measured while the experiment is running.

The relative gain spread σ_{gain} is defined as the standard deviation obtained by fitting the relative gain distribution of all PMTs to a Gaussian. It was 7.0% at the beginning of Super Kamiokande-I and 1.8% at the beginning of Super Kamiokande-II.

2.2.3 Relative Timing Calibration

The relative timing of PMT hits is important for event reconstruction. It depends on the length of the signal cable between the PMT and the ATM, and also depends on observed charge because of the discriminator slewing effect. The timing difference in each individual PMT has to be measured precisely to get better timing resolution. Figure 2.25 shows the system for measuring the relative timing of hit PMTs. The N_2 laser emits intense light of wavelength 337 nm within a very short time (less than 3 ns). The wavelength is shifted to 384 nm, which is near the lower edge of sensitivity of a PMT to the Cherenkov light, by a dye laser module. The light intensity is changed by an optical filter, and the PMT timing is measured at various pulse heights. After passing through the optical filter, the light goes to the diffuser ball in the detector through an optical fiber. The schematic view of the diffuser ball is also shown in Figure 2.25. The diffuser tip located at the center of the ball is made from

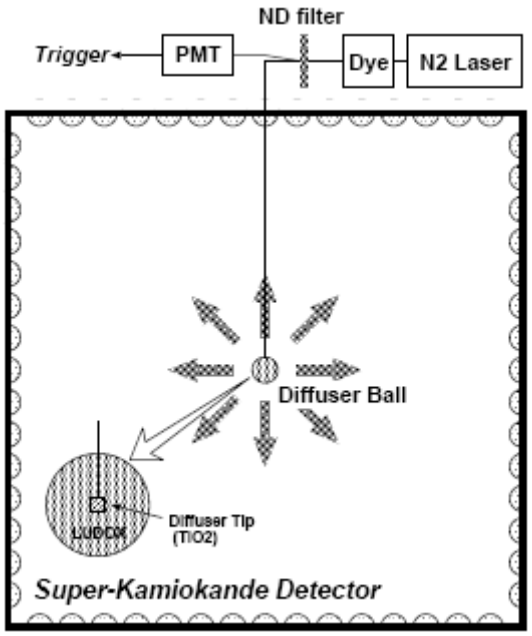

Figure 2.25 The timing calibration system.

TiO_2 suspended in optical cement. The light emitted from the tip is further diffused by LUDOX® manufactured by Grace Davison, silica gel made of 20 nm glass fragments. The combination of diffuser tip and LUDOX® make modestly diffused light without introducing significant timing spread. A typical scatter plot of the timing and pulse height is shown in Figure 2.26, which is called a 'TQ-map'. Each PMT has its own TQ-map, which is applied in data reduction. The timing resolution of PMTs as a function of pulse height is estimated from the TQ maps. Typical timing resolution at the single pe level is better than 3 ns.

2.2.4 Other calibrations

Beside the calibrations which were introduced so far, there are other calibrations

using stopping muon, neutral pion, LINAC, etc. The detail of the other calibrations can be found in [36].

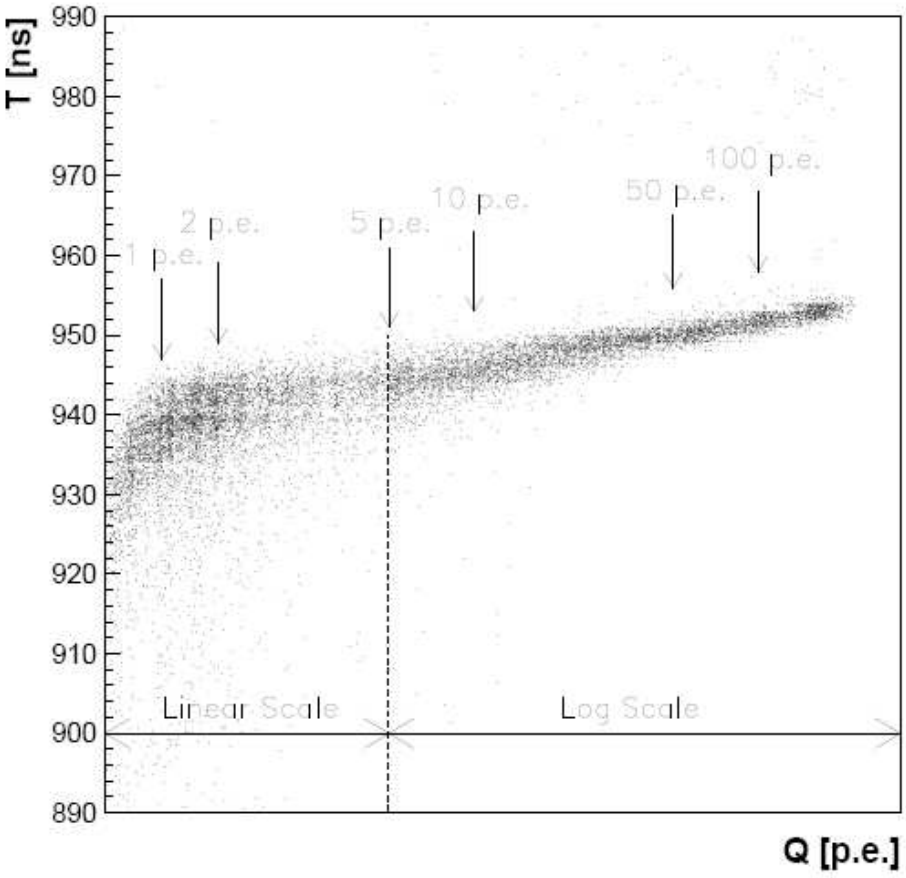

Figure 2.26 A typical plot of timing vs. pulse height. This plot is referred as 'TQ-map'.

2.3 2001 accident and Super Kamiokande-II reconstruction

Super Kamiokande underwent upgrade work to replace PMTs that began in mid-July, 2001 and ended in mid-September. It had begun to be filled with water since 18, September, 2001. On the morning of 12, November, when the purified water filled the tank to the level 31.7 m above the bottom (about 3/4 of the tank), about 60 % of the 50cm photomultipliers (PMTs) used for the Super Kamiokande detector were destroyed in a few seconds. Because data had been being taken continuously since the purified water started to fill the tank, we could analyze the data just after the accident to investigate what happen at the instant of accident. From the analysis of the data taken during a few msec period after the accident, it is most likely that the accident was caused by an implosion of one of the bottom PMTs. A lot of investigation about the possible cause of the implosion was done and the most possible cause was concluded like following.

1. Stress accumulated during the upgrade work caused the implosion of a PMT.
2. During the installation or transporting process a slight crack was made at the ASSY of a PMT caused the implosion.

And the test with the real PMTs and simulation proved that shock waves generated by an implosion of a single PMT trigger a chain reaction which destroys other PMTs. To prevent this kind of accident, it was necessary to improve PMT assembling and installation procedures and to encase PMTs to prevent onset of shock waves and chain reaction.

In 2002, the detector was reconstructed with reduced PMT coverage (47% of Super Kamiokande-I). All the PMTs were encased in acrylic covers. Super Kamiokande II were operated for about three years and terminated at October, 2005 to begin a full reconstruction.

Chapter 3

Monte Carlo Simulation

3.1 Flux calculation of atmospheric neutrino

To carry out detailed studies of neutrino oscillations using atmospheric neutrinos, it is important to know the expected flux without neutrino oscillations. The difficulties and the uncertainties in the calculation of atmospheric neutrino fluxes differ between high and low energies. For low energy neutrinos around 1 GeV, the primary fluxes of cosmic ray components are relatively well known. The low energy cosmic ray fluxes of less than about 10 GeV are modulated by solar activity, with the minimum flux occurring at times of high solar activity. At these energies, the primary cosmic rays are also affected by the geomagnetic field through a rigidity (momentum/charge) cutoff. For high energy neutrinos, above 100 GeV, primary cosmic rays with energies greater than 1000 GeV are relevant. At these energies, solar activity and the rigidity cutoff do not affect the cosmic rays, but details of the higher energy primary cosmic ray flux are not measured well. There are several flux calculations [6–14]. Unlike older calculations [15, 16], in which the secondary particles were assumed to travel in the direction of the primary cosmic ray (1-dimensional calculations), the current calculations employ three dimensional Monte Carlo methods.

In this section, we outline the methods of the calculation and results from three atmospheric neutrino flux calculations [10, 13, 14], which cover the energy range

relevant to the present analysis, are compared. They are used in the analysis of the Super-Kamiokande data. The measured flux of primary cosmic rays is used, including solar modulation and geomagnetic field effects. The interaction of cosmic ray particles with the air nucleus, the propagation and decay of secondary particles are simulated. A neutrino flux was calculated specifically for the Kamioka site. The calculated energy spectra of atmospheric neutrinos at Kamioka are shown in Figure 3.1 (a). Also shown in Figure 3.1 (b) is the comparison of the calculated fluxes as a function of neutrino energy. The agreement among the calculations is about 10% below 10 GeV. This can be understood because the accuracy in recent primary cosmic ray flux measurements [17, 18] below 100 GeV is about 5% and the data from independent experiments agree within the quoted uncertainties. However the primary cosmic ray flux is much less accurate above 100 GeV. Therefore, for neutrino energies much higher than 10 GeV, the uncertainties in the absolute neutrino flux could be substantially larger than the disagreement level among the calculations. 0.05 was assigned for the uncertainty in the energy spectrum index above 100 GeV in the primary cosmic ray energy spectrum. This causes approximate 0.05 uncertainties in the neutrino spectrum index above 5 GeV. Figure 3.2 shows the calculated flux ratio of ν_μ + *anti*-ν_μ to ν_e + *anti*-ν_e as a function of the neutrino energy, integrated over solid angle. This ratio is essentially independent of the primary cosmic ray spectrum. Especially, in the energy region of less than about 5 GeV neutrino energies, most of the neutrinos are produced by the decay chain of pions and the uncertainty of this ratio is about 3%, which is estimated by comparing the three calculation results. In the higher energy region (10 GeV for ν_μ + *anti*-ν_μ, and 100 GeV for ν_e + *anti*-ν_e), the contribution of *K* decay in the neutrino production is more important. There, the ratio depends more on the *K* production cross sections and the uncertainty of the ratio is expected to be larger. A 20% uncertainty in the K/π production ratio causes at least a few % uncertainties in the ν_μ + *anti*-ν_μ to ν_e + *anti*-ν_e ratio in the energy range of 10 to100 GeV. However, as seen from Figure 3.2, the difference in the calculated ν_μ + *anti*-ν_μ to ν_e + *anti*-ν_e ratio is substantially larger than that expected from the K/π uncertainty in the high energy region. The reason for this difference has not been

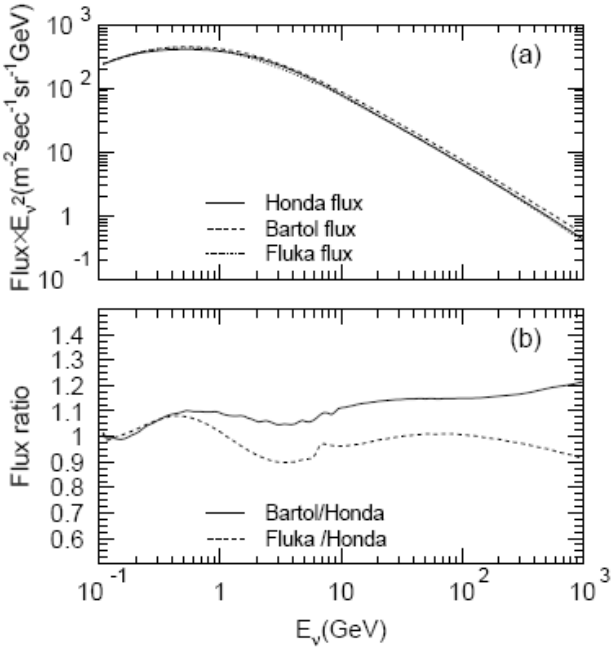

Figure 3.1 (a) The atmospheric neutrino energy spectrum calculated by several models. (b) The ratio of the calculated flux models.

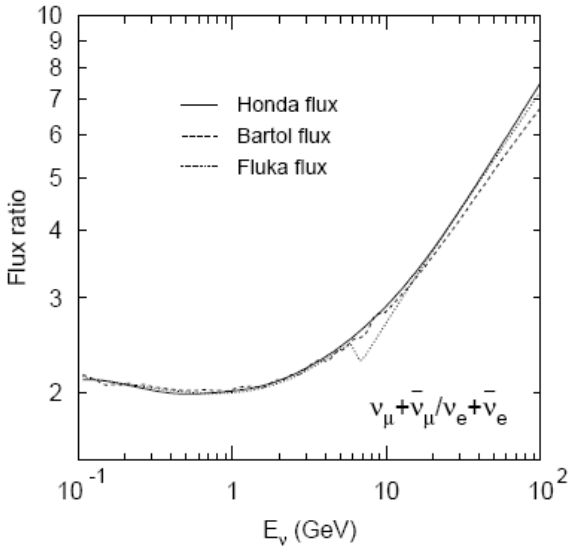

Figure 3.2 The flux ratio of ν_μ + *anti*-ν_μ / ν_e + *anti*-ν_e as a function of neutrino energy.

understood yet. As a consequence, an energy dependent uncertainty for the ν_μ + *anti*-ν_μ to ν_e + *anti*-ν_e ratio above 5 GeV neutrino energy is assumed based on the comparison of the three flux calculations. It is taken to be 3 % at 5 GeV and 10% at 100 GeV. Figure 3.3 shows the calculated flux ratios of ν_μ to *anti*-ν_μ and ν_e to *anti*-ν_e. The calculations agree to about 5% for both of these ratios below 10 GeV. However, the disagreement gets larger above 10 GeV as a function of neutrino energies. The systematic errors in the neutrino over anti-neutrino ratio are assumed to be 5 % below 10 GeV and 10% at 100 GeV for the ν_e to *anti*-ν_e ratio, and 5 % below 10 GeV and 25% at 100 GeV for the ν_μ to *anti*-ν_μ. Figure 3.4 shows the zenith angle dependence of the atmospheric neutrino fluxes of downward-going neutrinos are lower than those

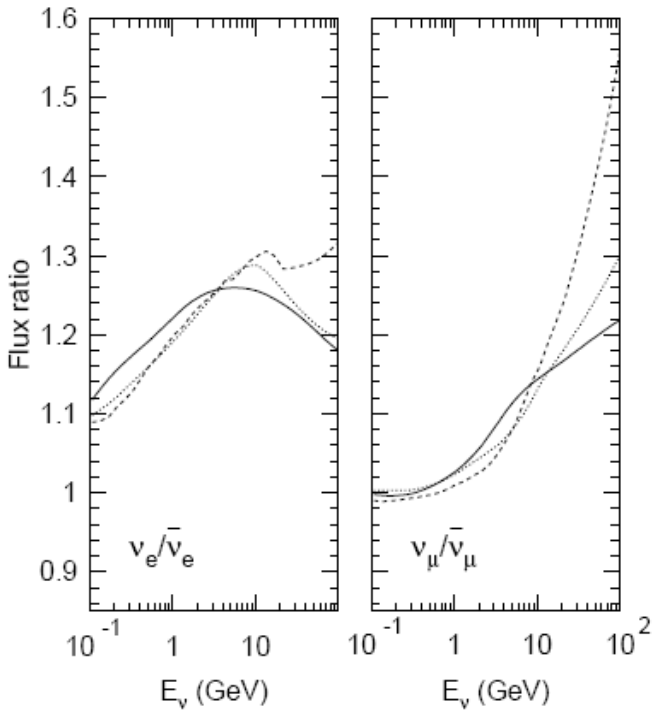

Figure 3.3 The flux ratios of ν_μ to *anti*-ν_μ and ν_e to *anti*-ν_e versus neutrino energy. Solid, dashed and dotted lines show the prediction by Honda, Bartol and Fluka flux.

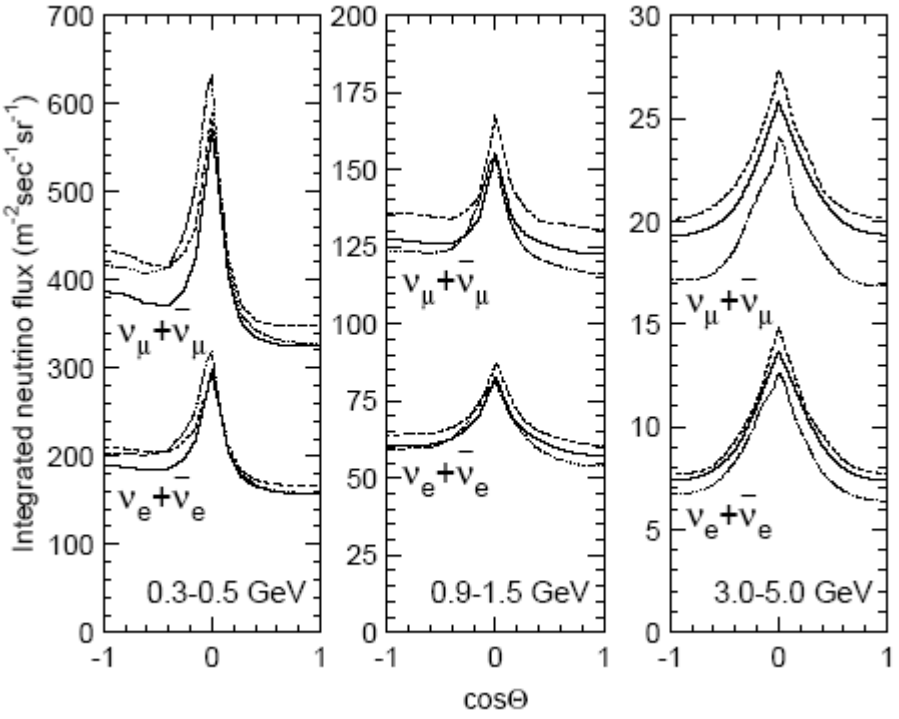

Figure 3.4 The flux of atmospheric neutrino versus zenith angle. Solid, dashed and dotted lines show the prediction by Honda, Bartol and Fluka flux.

of upward-going neutrinos. This is due to the deflection of primary cosmic rays by the geomagnetic field, roughly characterized by a minimum rigidity cutoff. For neutrino energies higher than a few GeV, the calculated fluxes are essentially up-down symmetric, because the primary particles are more energetic than the rigidity cutoff. The enhancement of the flux near horizon for low energy neutrinos is a feature characteristic of full three dimensional flux calculations [6–14]. However, in Super-Kamiokande, the horizontal enhancement cannot be seen in the lepton zenith angle distribution, due to the relatively poor angular correlation between neutrinos and leptons below 1 GeV. The uncertainties in the up-down and vertical-horizontal ratios of the number of events are estimated by comparing the predicted ratios of various

flux models. These uncertainties generally depend on the energy and the neutrino flavor. The uncertainty in the up-down event ratio is about 1 to 2% in the sub-GeV energy region and is about 1% in the multi-GeV energy region. The main source of the uncertainty in the vertical-horizontal ratio around a GeV is the size of the horizontal enhancement of the flux due to the three dimensional effect; the uncertainty is estimated to be less than a few percent. In the higher energy region, where upward through-going muons are relevant, the largest source of the uncertainty in the vertical-horizontal ratio is the *K* production cross section. We assume that the π /*K* production ratio uncertainty is 20% in the whole energy region. The uncertainties in the zenith angle and energy distributions due to the π /*K* production uncertainty are included in the systematic errors in the analysis. This error is most important for higher energy neutrinos. For example, the vertical-horizontal uncertainty for upward through-going muons due to the π/*K* production uncertainty is estimated to be 3% [19]. Figure 3.5 shows the zenith angle dependence of the atmospheric neutrino fluxes for higher energy region observed as upward muons in Super-Kamiokande. The flight length of neutrinos is an important ingredient in the analysis of neutrino oscillation. For neutrinos passing a great distance through the Earth, the flight length can be accurately estimated. However, for horizontal and downward going neutrinos, the height of production in the upper atmosphere must be accurately distributed by the Monte Carlo method. Figure 3.6 shows the distribution of calculated flight length of neutrinos for vertically down-going and horizontal directions. In summary of the atmospheric neutrino flux, we remark that, the ν_μ + *anti*-ν_μ to ν_e + *anti*-ν_e flux ratio is predicted to an accuracy of about 3% in the energy region relevant to the data analysis discussed in this thesis. The zenith angle dependence of the flux is well understood, and especially, above a few GeV neutrino energies, the flux is predicted to be up-down symmetric.

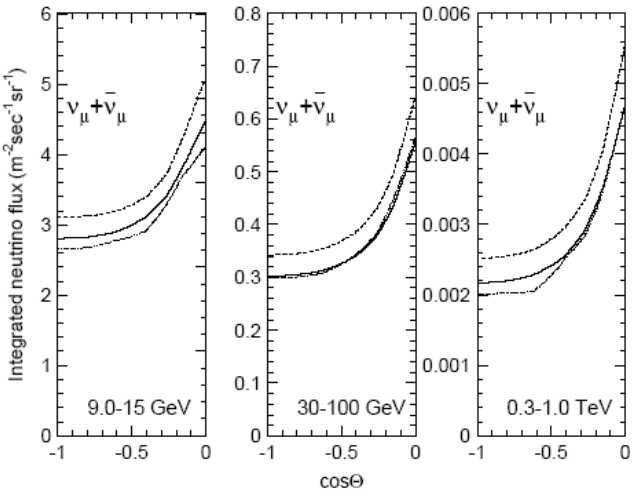

Figure 3.5 The zenith angle distribution of the flux of upward-going atmospheric neutrino observed as upward-going muon event in Super Kamiokande. Solid, dashed and dotted lines show the prediction by Honda, Bartol and Fluka flux.

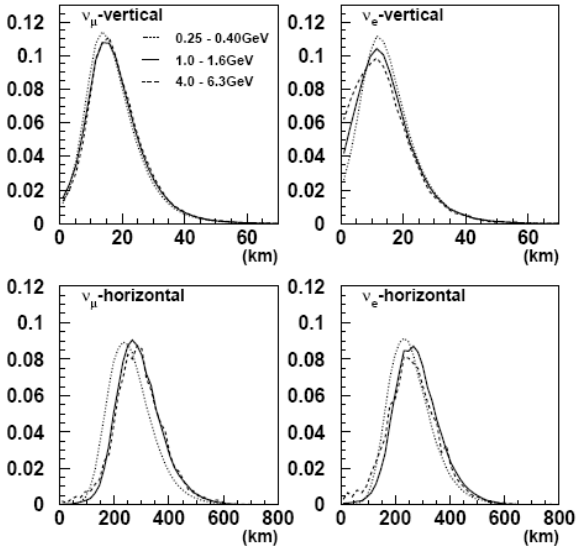

Figure 3.6 The calculated flight length of neutrinos for vertically down-going ($0.95 < \cos\theta < 1.0$) and near horizontal-going ($0.05 < \cos\theta < 0.10$) directions.

3.2 Neutrino Interaction

The neutrino oscillation analysis relies heavily on detailed comparison of the experimental data with the theoretical expectation. An important element of this is to simulate the interaction of neutrinos from 10 MeV to 100 TeV with the nuclei of water, or in the case of upward going muon, the nuclei of the rock surrounding the detector, assumed to be SiO_2. In the simulation program, the following interactions were considered.

- quasi-elastic scattering, $\nu N \rightarrow lN'$
- single meson production, $\nu N \rightarrow lN'm$
- coherent π production, $\nu\,^{16}O \rightarrow l\pi\,^{16}O$
- deep inelastic scattering, $\nu N \rightarrow lN'hadrons$

Where, *N* and *N'* are the nucleons, *l* is the lepton, and *m* is the meson, respectively.

3.2.1 Elastic and quasi-elastic scattering

The formalization of quasi-elastic scattering off a free proton, which was used in the simulation programs, was described by Llewellyn-Smith[21]. For scattering off nucleons in ^{16}O, the Fermi motion of the nucleons and Pauli Exclusion Principle were taken into account. The nucleons are treated as quasi-free particles using the relativistic Fermi gas model of Smith and Moniz[22]. The momentum distribution of the nucleons were assumed to be flat up to the fixed Fermi surface momentum of 225 MeV/c. This Fermi momentum distribution was also used for other nuclear interactions. The nuclear potential was set to 27 MeV/c.

3.2.2. Single meson production

Rein and Sehgal's model was used to simulate the resonance productions of single π, K and η [23, 24]. In this method, the interaction is separated into two parts:

$$\nu + N \rightarrow l + N^*,$$
$$N^* \rightarrow m + N'$$

where m is a meson, N and N' are nucleons, and N* is a baryon resonance. The hadronic invariant mass, W, the mass of the intermediate baryon resonance, is restricted to be less than 2 GeV/c^2. In addition to the dominant single π production, K and η production is considered.

To determine the angular distribution of pions in the final state, Rein and Sehgal's method for the P_{33} (1232) resonance were used. For the other resonances, the directional distribution of the generated pions is set to be isotropic in the resonance rest frame. The angular distribution of π^+ has been measured for $\nu p \rightarrow \mu^- p \pi^+$ mode[25] and the results agree well with the Monte Carlo prediction. The Pauli blocking effect in the decay of the baryon resonance was considered by requiring that the momentum of nucleon should be larger than the Fermi surface momentum. Pion-less delta decay is also considered, where 20 % of the events do not have the pion and only the lepton and nucleon are generated [26]. The quasi-elastic and single meson production models have a parameter (axial vector mass, M_A) that must be determined by experiments. For larger M_A values, interactions with higher Q^2 values (and therefore larger scattering angles) are enhanced for these channels. The M_A value was tuned using the K2K [27] near detector data. In our atmospheric neutrino interaction Monte Carlo simulation, M_A was set to 1.1 GeV for both the quasi-elastic and single meson production channels, but the uncertainty of the value is estimated to be 10%. Coherent single pion production, the interaction between the neutrino and the entire oxygen nucleus, was simulated using the formalism developed by Rein and Sehgal [28].

3.2.3. Deep inelastic scattering

In order to calculate the cross sections of deep inelastic scattering, the GRV94 [29] parton distribution function was used. In the calculation, the hadronic invariant mass, W, is required to be greater than 1.3 GeV/c^2. However, the multiplicity of pions is restricted to be greater than or equal to 2 for $1.3 < W < 2.0$ GeV/c^2, because single pion production is separately simulated as previously described. In order to generate events with multi-hadron final states, two models were used. For W between 1.3 and 2.0 GeV/c^2, a custom made program [30] was used to generate the final state hadrons; only pions are considered in this case. For W larger than 2 GeV/c^2, PYTHIA/JETSET [31] was used.

Total charged current cross sections including quasi-elastic scattering, single meson productions and deep inelastic scattering are shown in Figure 3.7.

3.2.4. Nuclear effects

The interactions of mesons within the ^{16}O nucleus are also important for the atmospheric neutrino analysis. Basically, all of the interactions were treated by using a cascade model. The interactions of pions are very important because the cross section for pion production is quite large for neutrino energies above 1 GeV and the interaction cross sections for pions in nuclear matter is also large. In the simulation of pion interactions in ^{16}O, inelastic scattering, charge exchange and absorption were considered. The procedure to simulate these interactions is as follows. The initial position of the pion was generated according to the Woods-Saxon nucleon density distribution [32]. The interaction mode is determined from the calculated mean free path of each interaction. To calculate the mean free path, the model described by Salcedo et al. [33] was adopted. The calculated mean free path depends not only on the momentum of pion but also on the position of the pion in the nucleus. If inelastic scattering or charge exchange occurs, the direction and momentum of the pion are

determined by using the results of a phase shift analysis obtained from π-*N* scattering experiments[34]. When calculating the pion scattering amplitude, the Pauli blocking effect is also taken into account by requiring the nucleon momentum after interaction to be larger than the Fermi surface momentum at the interaction point. The pion interaction simulation was checked using data for the following three interactions: π^{12}C scattering, π^{16}O scattering and pion photo-production ($\gamma + {}^{12}C \rightarrow \pi^{-} + X$) [37].

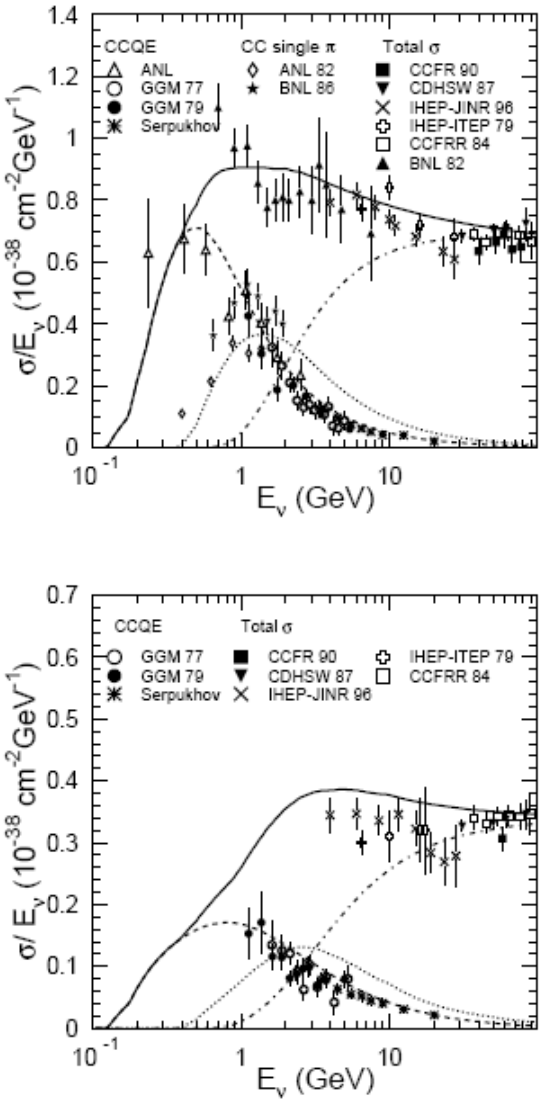

Figure 3.7 Cross section for neutrino (upper) and anti-neutrino (lower). Solid line shows the calculated total cross section. The dashed, dot and dash-dotted lines show the calculated quasi-elastic, single-meson and deep-inelastic scatterings, respectively. Data points are from various experiments.

Chapter 4

Atmospheric Neutrino Data Reduction and Reconstruction

Atmospheric neutrinos observed in Super Kamiokande are classified into four categories. The neutrinos, which were observed via charged current interactions with nuclei in the 22.5 kiloton water fiducial volume, are classified into fully-contained (FC) events if all of the energy is deposited inside the inner detector of Super-K and into partially-contained (PC) events if high energy muons produced by neutrino interactions exit the inner detector. The neutrino energies of partially-contained events are typically 10 times higher than that of fully-contained. Neutrinos can also undergo charged current interaction with the rock surrounding the detector and the outgoing high energy muons can intersect the detector. These neutrino induced muons in the rock cannot be distinguished from the cosmic ray muons traveling downward. However, the muons traveling in upward direction must be neutrino induced because cosmic ray muon cannot traverse the depth of earth in upward direction. These neutrino induced upward-going muons (UPMU) are classified into upward stopping muon if the muons come to rest in the inner detector, and into upward through-going muon if the muons pass through the entire inner detector volume. The neutrino energies of upward stopping muon events are about 10 GeV, which is roughly same as that of partially-contained events. The upward through-going muon events are the

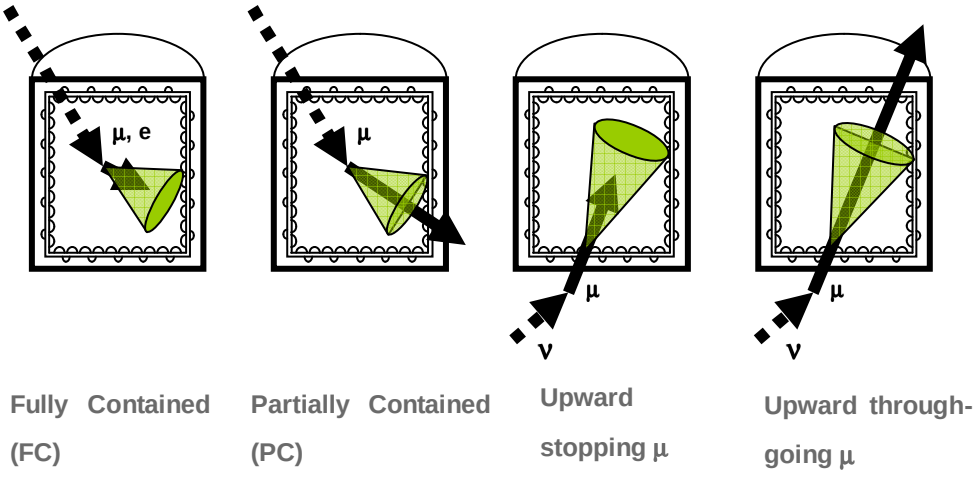

Figure 4.1 A schematic view of the four event categories of the atmospheric neutrinos observed in Super Kamiokande.

most energetic. Their parent neutrino energy is about 100 GeV on average. A schematic view of the four event categories are shown in Figure 4.1.

Three different reduction schemes were used to isolate fully contained events, partially contained events, and upward going muons, respectively. The fully contained and partially contained data sets shared a common set of good run selection criteria to choose good quality of data and therefore have identical live-time. The upward going muon data set relies mostly on fitting long muon track length. So it was less affected to detector conditions and had looser data quality cuts and therefore has different live-time from fully contained or partially contained data. To separate fully contained and partially contained events, a fast spatial clustering algorithm was applied to the outer detector hits. If the number of hits in the largest OD cluster was less than 10 (16 in SK-II), the event was classified as fully contained a (FC), otherwise, it was classified as partially contained (PC). Figure 4.2 shows the distribution of the number of the outer detector hits in the largest OD cluster for data (dot) and MC (histogram). A clear separation of FC and PC events is seen at 10 hits in SK-I. The criterion of the separation was tuned to 16 in SK-II. Systematic uncertainty of the FC and PC separat-

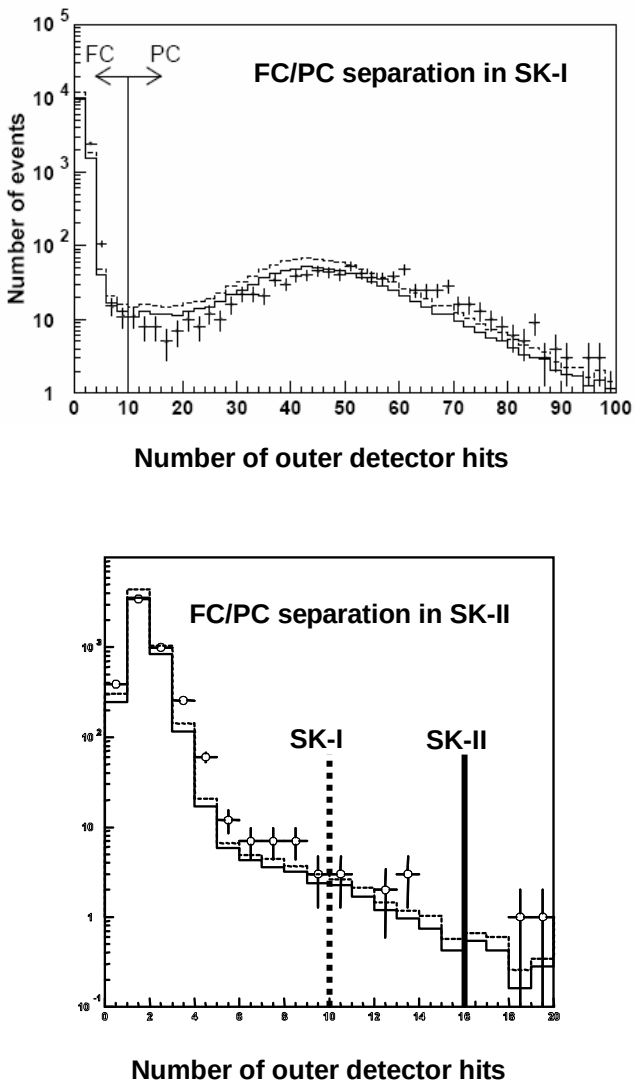

Figure 4.2 The number of hits in the largest outer detector cluster, which was used to separate the FC and PC event. The histogram is the MC prediction with neutrino oscillation (solid line) and no oscillation (dashed line). The upper figure is for SK-I MC and data. The lower figure is with SK-II, which zoomed in the region around the separation. In SK-II, the criteria of the separation was defined as 16.

-ion was estimated by scaling the number of outer detector hits to match the distribution among data and MC.

4.1 Fully Contained Events (FC)

4.1.1 FC data reduction

The Super Kamiokande event sample consists mainly of downward going cosmic ray muons and low energy radioactivity from parents such as radon. Cosmic ray muons are easily discriminated by requiring little or no ring activity in the outer detector. For atmospheric neutrino analysis, we consider the events with visible energy above 30 MeV, where visible energy (E_{vis}) is defined as the energy of an electromagnetic shower that gives a certain amount of Cherenkov light (for example, a muon of momentum 300 MeV/c yields a visible energy of about 110 MeV). To make the final FC data sample, the following five steps of data reduction criteria were used.

(1) First reduction and (2) Second reduction

Simple and efficient criteria were applied in the first and second reduction steps

• PE_{300} > 200 p.e (100 p.e for SK-II)

Where, PE_{300} is the maximum total photo electrons collected in the inner detector within 300 nsec sliding time window.

• PE_{max}/PE_{300} < 0.5

Where, PEmax is the maximum p.e. in any single PMT in inner detector.

• $NHITA_{800}$ < 25

Where, $NHITA_{800}$ is the number of hit PMT in outer detector (OD) within 800 nsec

sliding time window.

• TDIFF > 100 μsec

Where TDIFF is the time interval from the preceding event. This is to reject electrons from stopping muon decays.

(3) Third reduction

More complex criteria were applied in the third reductions step with the help of event reconstruction tools, for further rejection of cosmic ray muons and low energy events.

• $NHITA_{in} < 10$ and $NHITA_{out} < 10$ (In SK-II, $NHITA_{in} < 16$ and $NHITA_{out} < 16$)

Where, $NHITA_{in}$ ($NHITA_{out}$) is the number of hit OD PMTs within 8 m from the entrance (exit) point of muon track fitted using the inner detector light pattern.

• $NHIT_{50} < 50$ (25 for SK-II)

Where, $NHIT_{50}$ is the number of hit ID PMTs in 50 nsec sliding time window.

(4) Fourth reduction

Additional selection criteria were used to eliminate spurious events, such as "flashing" PMTs that emit light from internal corona discharges. Flasher events were removed by two different methods.

• Typical flasher events have broader PMT timing distributions than the neutrino events. Events with broader timing distributions were eliminated.

• Since flasher events have a tendency to be repeated with similar spatial hit distribution, the pattern information of observed charge was used on to eliminate these events. A correlation parameter based on the charge pattern was calculated with other data events and a "matched" tag was assigned for highly correlated events.

A cut was applied based on maximum correlation value and the number of "matched" with other events.

(5) Fifth reduction

Two further event types were eliminated in the fifth reduction step.

• $NHITA_{off} < 10$

Where $NHITA_{off}$ is the number of OD hits in 200 nsec sliding time window preceding the trigger time (-8900 ~ -100 nsec). This cut eliminates decay electrons from invisible cosmic ray muons that are below Cherenkov threshold in the inner detector.

• Cosmic ray muons are removed using a more precise fitter and the same criteria as the first cut of (3).

Finally, the vertex was required to be within a fiducial volume, 2 meters from the wall of the inner detector, and the visible energy was required to be greater than 30 MeV. Table 4.1 and 4.2 shows the event rate for each reduction step and the efficiency.

4.1.2 FC event reconstruction

The fully contained events, which passed through the data reduction, underwent a series of reconstruction.

(1) Vertex Fitting

First, the vertex position was determined using PMT hit times. The point which best fit the distribution of PMT time was obtained by adjusting it for the time of flight of the Cherenkov light and was defined as the initial vertex position. The vertex was reconstructed again after particle identification was established, to correct for particle

Table 4.1 Event rate for each FC reduction step

		events/day
Raw data		~ 10^6
1	• Low energy cut (total p.e.) • Decay-e cut (time interval from previous trigger)	~ 3000
2	• Cosmic ray μ cut (OD hits in 800 ns time window) • Low E & Flasher cut (Max p.e/Total p.e.)	~ 200
3	• Cosmic ray μ cut (OD hits around reconstructed entry or exit) • Low E cut (ID hits in 50 ns time window)	~ 45
4	• Flasher cut (broad time distribution and pattern algorithm)	~ 18
5	• Invisible cosmic ray μ cut (OD hits in earlier time) • Cosmic ray μ cut (OD hits around precisely reconstructed entry or exit)	~ 16
Fiducial volume and visible energy cut		~ 8

Table 4.2 The efficiency of each reduction step of FC events.

Reduction step	**SK-II (%)**	**SK-I (%)**
1st reduction	99.92	99.95
2nd reduction	99.89	99.94
3rd reduction	99.71	99.85
4th reduction	99.39	99.17
5th reduction	99.32	99.15
Fiducial volume and visible energy cut	99.17	97.59

track length. This final vertex fitter worked well for both SK-I and SK-II. However, it was found that the reconstruction accuracy of the initial vertex fit was deteriorated in SK-II. So in order to keep comparable performance with SK-I, new algorithm to fit Cherenkov edge was adopted and finally the performance of the initial vertex fit of SK-I and SK-II had become comparable. The final vertex resolution was estimated to be about 30 cm for single ring fully contained events in both SK-I and SK-II.

(2) Ring Counting

After an initial ring direction and vertex were found, other possible rings were searched using a Hough transform [38] based technique. The technique is iterative. A second ring was searched for by choosing possible ring directions based on the Hough map, and a likelihood technique determined if a second ring from the list of the possible rings is more consistent with the data than just one ring. If a second ring is judged to be more consistent, then this procedure was repeated as many as necessary until finally no further rings were necessary to fit the data. Figure 4.3 and 4.4 show the likelihood difference between the 2 ring assumption and a 1 ring assumption for SK-I and SK-II, respectively. In these figures, the oscillation at the best fit parameters ($\sin^2 2\theta = 1.0$, $\Delta m^2 = 2.1 \times 10^{-3}$ eV^2) was taken into account for the Monte Carlo prediction. Hereafter, if there is no mention, Monte Carlo prediction is with oscillation effect. A cut was made at likelihood difference of 0 to separate single and multi ring events. The efficiency for identifying charged current (CC) quasi-elastic ν_e (ν_μ) events as single-ring was 93.2 (95.8) % for SK-I and 92.6 (95.8) % for SK-II.

(3) Particle Identification

To determine the identity of the final state particles, a particle identification algorithm was applied which exploited systematic differences between Cherenkov rings produced from different particles. Cherenkov rings from electron or gamma-ray exhibit diffuse light distribution because of electromagnetic cascades and multiple scattering and are called *e*-like events. On the other hand, Cherenkov rings from muon or charged pion give sharper ring edge and are called μ-like events. Figures 4.5 and

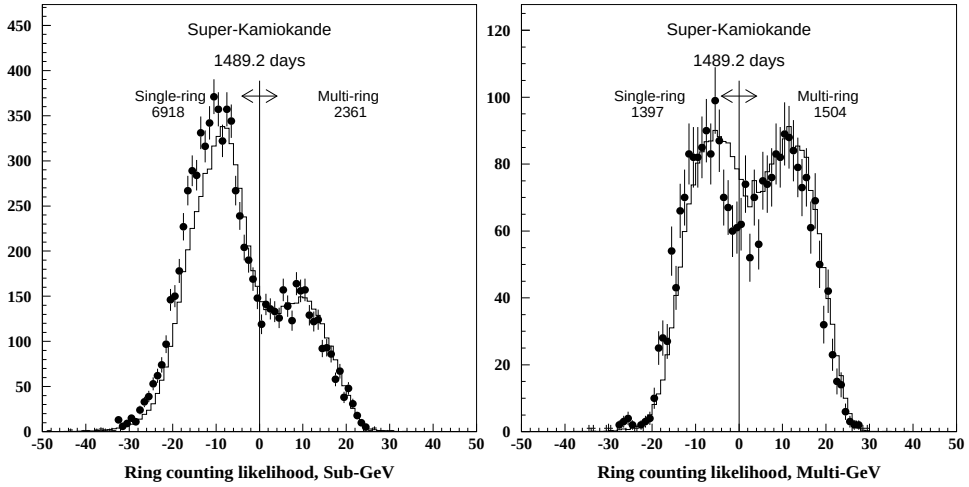

Figure 4.3 The distribution of the likelihood difference between a single-ring and multi-ring assumption for sub-GeV (left) and multi-GeV (right) FC events of SK-I. The points show the data and the histograms show the Monte Carlo.

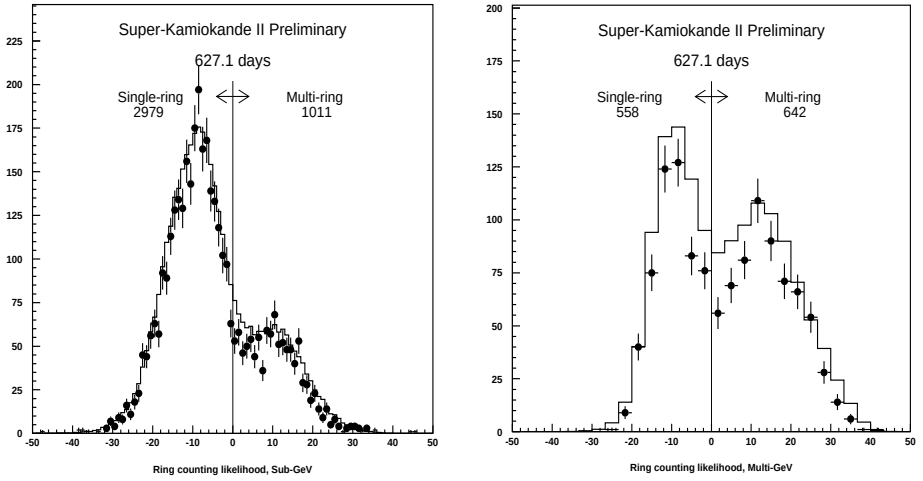

Figure 4.4 The distribution of the likelihood difference between a single-ring and multi-ring assumption for sub-GeV (left) and multi-GeV (right) FC events of SK-II. The points show the data and the histograms show the Monte Carlo.

4.6 show observed single-ring *e*-ike and μ-like events, respectively. The opening angle of the Cherenkov cone, which depends on $\beta(\equiv v/c)$, was also used to separate *e*-like and μ-like events at low momenta. The validity of the method was confirmed by a beam test experiment at KEK [39]. The misidentification probabilities for single-ring *e*-like and μ-like events were estimated using simulated charged CC (Charged Current) quasi-elastic neutrinos and summarized in the Table 4.3. The distribution of the likelihood variable used to discriminate single-ring *e*-like and μ-like events are shown for both the data and MC for the sub-GeV and multi-GeV samples in Figure 4.7 and 4.8 for SK-I and SK-II, respectively. In both of these cases, there is a clear separation of the likelihood variable.

(4) Precise Vertex Fitting & Momentum Determination

Next, the Cherenkov rings were re-fit taking into account the expected light pattern given by the particle identification, and in the case of single-ring events, a specialized event fitter was applied. After the rings were re-fit, the total photo-electrons were apportioned to all of the rings. The momentum of a particle was determined from the total number of p.e.s within a 70° half-angle of the cone relative to the track direction, with corrections for light attenuation and PMT angular acceptance.

As a final procedure, the final energy and the angle information of the ring were checked to remove the rings which are not real most likely.

4.2 Partially Contained Events (PC)

4.2.1 PC data reduction

The data reduction for PC events is different from the reduction for FC events in respect of being required the presence of OD activity. Because these extra OD hits, which result from the exiting particle, a simple criterion based on the number of hits in the OD tubes could not be applied to reject cosmic ray background. The reduction

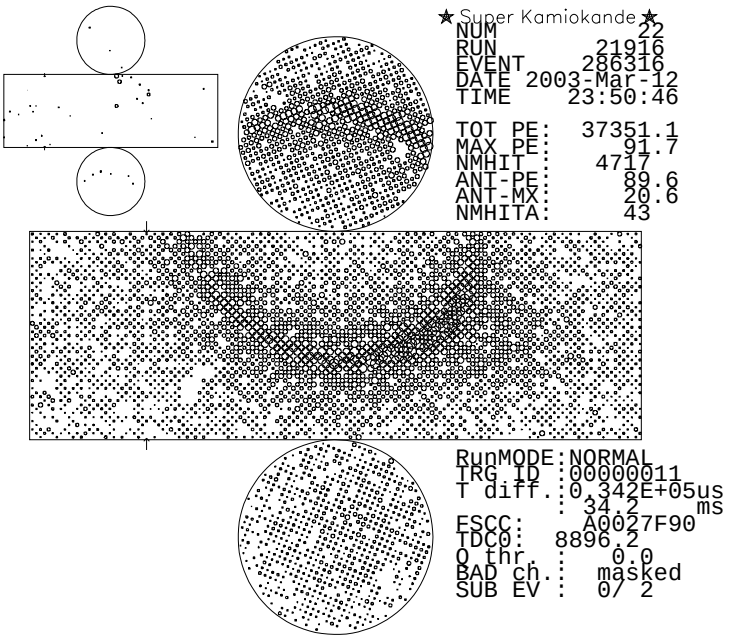

Figure 4.5 An event display of an observed single-ring *e*-like event.

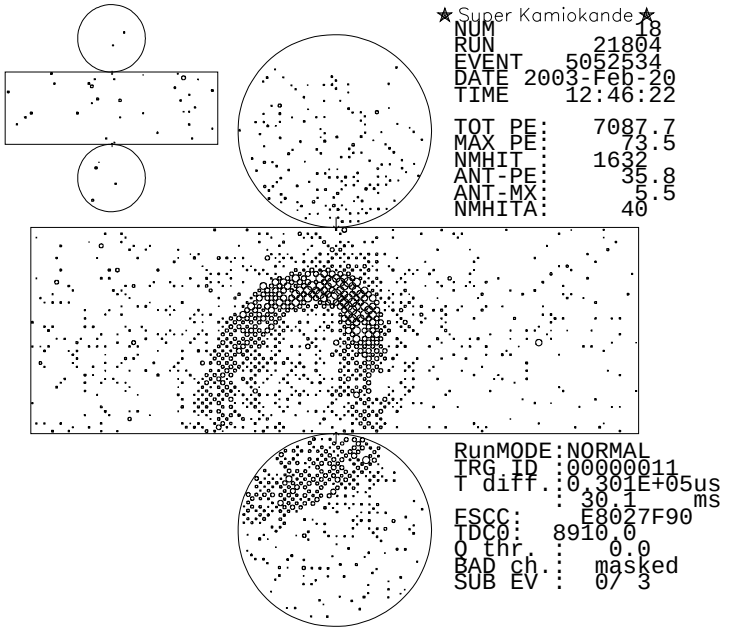

Figure 4.6 An event display of an observed single-ring μ-like event.

Table 4.3 The misidentification probabilities for single-ring *e*-like and μ-like events estimated with simulated CC quasi-elastic neutrinos

	SK-II	**SK-I**
Sub-GeV		
e → μ	0.9 %	0.8 %
μ → e	1.5 %	0.9 %
Multi-GeV		
e → μ	0.4 %	0.4 %
μ → e	1.1 %	1.4 %

used to identify partially contained events is described in this section. The description is based on SK-I data reduction. Though SK-II has basically similar reduction step, some critical values were tuned to keep similar event rate and efficiency with SK-I.

(1) First reduction

• $PE_{tot} > 1000$ p.e.

Where, PE_{tot} is the total photo electrons observed in the ID. This criterion correspond to muons (electrons) with momentum less than 310 (110) MeV/c. By definition, an exiting particle in the PC sample must have reached the OD from the inner fiducial volume, and so must have had a minimum track length of about 2.5 m, which correspond to muons greater than 700 MeV/c in momentum.

(2) Second reduction

• TWIDA < 260 nsec

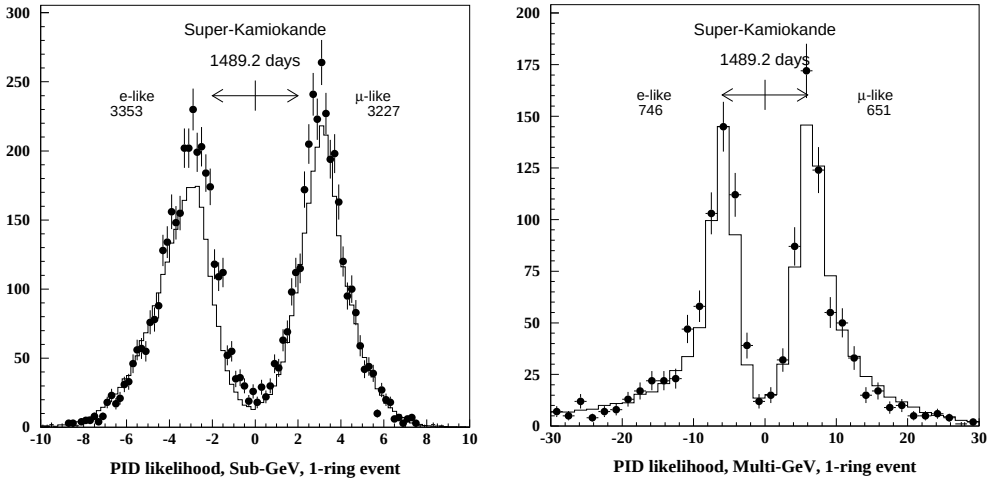

Figure 4.7 The distribution of particle identification likelihood for sub-GeV (left) and multi-GeV (right) FC single-ring events of SK-I. Dots show data and histograms show Monte Carlo.

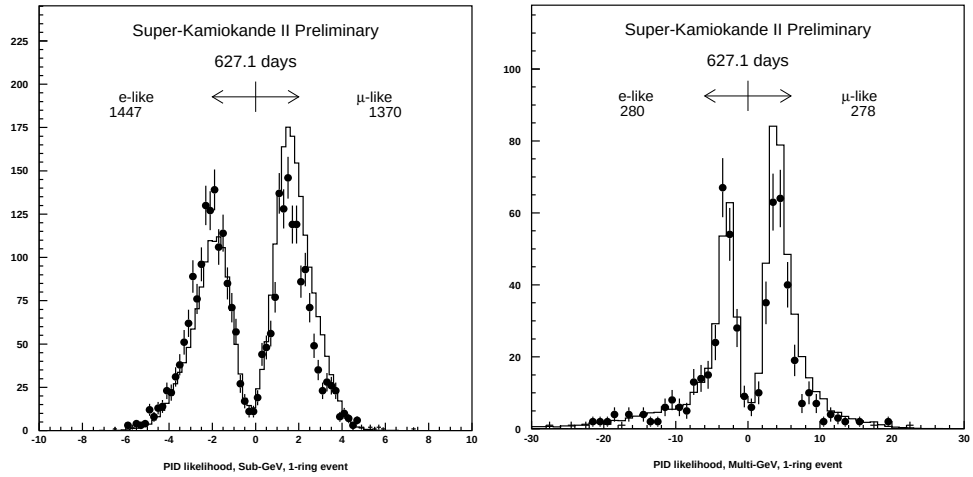

Figure 4.8 The distribution of particle identification likelihood for sub-GeV (top) and multi-GeV (bottom) FC single-ring events of SK-II. Dots show data and histograms show Monte Carlo.

Where, TWIDA is the width of the time distribution of hits in the OD.

• NCLSTA < 2

Where NCLSTA is the number of hit clusters in the OD.

These cuts eliminated through going muons, which left two well separated clusters in the OD.

• $NHITAC_{min}$ < 7

Where, $NHITAC_{min}$ is the minimum number of hit PMTs among top (or bottom) and side regions in the OD hit cluster. Muons which clipped the edges of the detector were eliminated by this cut.

• PE_{200} > 1000 p.e.s

Where, PE_{200} is the number of photoelectrons within 200 cm from OD cluster. Cosmic ray muons which entered and stopped in the inner volume of the detector were eliminated by this cut. This cut did not remove PC neutrino events because PC events produce large numbers of photoelectrons (typically 3500 p.e.'s in SK-I) in the region where the particle exited.

(3) Third reduction

In third step, a simple vertex fit and weighted direction estimation were used.

• $NHITA_{in} \leq 10$ (16 for SK-II)

Where, $NHITA_{in}$ is the number of OD hits within 8 m of the back-projected entrance point.

• Flasher events were removed by using their broader timing distribution feature.

(4) Fourth reduction

• $\mathbf{d_{pfit}} \cdot \mathbf{d_{PMT}} > -0.8$

Where, $\mathbf{d_{pfit}}$ is the reconstructed direction by point fit and $\mathbf{d_{PMT}}$ is the direction from the reconstructed vertex to the earliest hit ID PMT. This cut eliminate background muons which left few or no entrance hits in the OD.

• DCORN > 1.5 m

Where, DCORN is the distance from the reconstructed vertex to the corner of ID. This cut removes the remaining corner clipping muons.

• Fitted muon track length > 30 m (if goodness of through-going muon fit > 0.85)

(5) Fifth reduction

In the last reduction step, various remaining background events were eliminated by several selection criteria.

• $NHITA_{clust} \geq 10$ (16 for SK-II)

Where, $NHITA_{clust}$ is the OD hits in the most highly charged cluster in OD. Fully-contained events were eliminated by this cut.

• $PE_{tot} > 3000$ p.e

This cut is to get rid of low energy background events. 3000 total p.e.s in the inner detector correspond to 350 MeV of visible energy, well below that of any exiting muon.

• $DIST_{clust} > 20$ m

Where, $DIST_{clust}$ is the distance between the highest charge OD hit cluster and the second highest one. Clusters in the OD were searched for again with the same clustering algorithm used in the 2nd reduction step but with different clustering parameters. Some obvious through-going muons were removed by this cut.

- The most remaining background events so far are due to the imprecision of the fast fitters we used. A precise fitting algorithm was then applied to obtain more accurate information on ring direction and vertex position. With much more accurate information of the event, most remaining through-going and stopping events were able to be eliminated based on their distinct geometry and OD signatures.

- Some through-going muons have a very special geometry. They passed through the tank vertically along the wall of ID. These events were eliminated by counting the number of p.e.s. and hits within the region defined by an 8 m sphere around the top and bottom fringes and checking the time interval between the average timings of those top and bottom hits.

- Cable hole muon cut

There are four holes on the top of OD through which cables run and which make OD inefficient to the penetration of cosmic ray muon. To compensate the inefficiency for the holes, scintillation counters, which are called veto counters, were installed over the holes on the top of the detector. Events with a veto counter hit and consistency with cosmic ray muon were eliminated.

After the final reduction step, events were scanned by physicists to check the data quality. However, no event is rejected based on the scanning. Finally, the vertex was required to be within a fiducial volume, 2 meters from the wall of the inner detector. The final event sample is an almost 100 % pure sample. The background contamination has been estimated to be about 0.2 %. Table 4.4 and 4.5 shows the event rate for each PC reduction step and the detection efficiency for both SK-I and SK-II.

4.2.2 PC Event Reconstruction

The partially-contained events were reconstructed using inner detector PMT information by similar vertex, direction fit and ring-counting algorithms to the one of fully contained events. For some PC events, however, the direction fit was slightly modified and some criteria were tuned for SK-II PC event. The description of the criteria in this section is based on SK-I event reconstruction.

Table 4.4 Event rate for each PC reduction step

		events/day
Raw data		~ 10^6
1	• Low energy cut (total p.e.)	~ 20000
2	• Cosmic ray μ cut (OD time distribution and # of OD hit cluster) • Edge clipper cut (OD cluster topology) • Stop μ cut (low ID p.e. near OD cluster)	~ 3500
3	• Cosmic ray μ cut (OD hits around back-projected entry) • Flasher cut (broad time distribution)	~ 250
4	• Low OD activity cosmic ray μ cut (compare earliest ID hit & back-projected entry) • Edge clipper cut (fitted vertex position near ID corner) • Through-going μ cut (long fitted track length)	~ 36
5	• FC cut (OD hits in highly charged cluster) • Low E cut (total p.e.) • Through-going μ cut (# of OD hit cluster with different clustering parameter from 2^{nd} reduction) • Stop or through-going μ cut (precise fitter info) • Cosmic ray μ cut passing through vertically along ID wall • Cable hole μ cut (veto counter)	~ 1
Fiducial volume and total p.e. cut		~ 0.6

Table 4.5 The detection efficiency of PC events at each reduction step.

Reduction step	SK-II (%)	SK-I (%)
1st reduction	98.7	99.0
2nd reduction	94.2	94.2
3rd reduction	93.1	93.1
4th reduction	85.8	87.9
5th reduction (Junk cut)	83.2	85.8

In case that the number of tubes in the largest OD cluster was greater or equal to 20 and there is no clear ID exit point or ID is judged to be saturated, outer detector spatial information was used rather than the results of the precise fitting algorithm. 'No clear ID exit point' and 'Saturated ID' were defined like following.

• No clear ID exit point

If the ID PMT nearest to the projected ID exit point of the fitted track with more than 200 p.e.'s was more than 200 cm away, then it was regarded there is no clear ID exit point.

• Saturated ID

If there were more than 800 ID PMT hits with more than 200 p.e.'s in each of them, it was judged to be saturated.

The estimated vertex position resolution for PC events was 64 cm. The angular resolution for the penetrating particle in a PC event was estimated to be 2.8°. Finally, the fiducial volume cut was applied. The event rate in the fiducial volume was 0.61 events/day and 0.52 events/day in SK-I and SK-II, respectively without taking into account Monte Carlo efficiency and background.

4.3 Upward going muon (UPMU) data

The upward-going muons observed in Super-K are classified into two categories, that is, upward stopping muon events having only an entrance signal in the OD and upward through-going muon events having both entrance and exit signals in the OD as explained at the beginning of this chapter. The criterion used to separate FC and PC events was used to determine an event entry or exit signal. 10 (16 for SK-II) OD hits within 8 m of the reconstructed entry or exit point were defined as a muon entry or exit signal. We required the geometrical trajectory of through-going muons to be greater than 7 m in the inner detector, and we imposed a momentum threshold of 1.6 GeV to stopping muon, which is equivalent to 7 m path length. The purpose of the data reduction is to isolate the upward muon events and the horizontal muon events, which are needed for background estimation, to provide a classification of stopping or through-going muon type, and to reject the background from cosmic ray muons and noise such as flashing PMTs. Figure 4.9 shows the overall procedure to isolate upmu events with rough event rate for each step. First, the very clear background was rejected in the upmu reduction step and then the output of the reduction was passed to the precise fitter. With the fitting information the precise fitter gives, downward direction cut, 7 m track length cut for through-going muon and 1.6 GeV momentum cut for stopping muon were applied. Finally, the events passed through the precise fitter cuts were scanned by physicists and the remaining backgrounds were rejected.

4.3.1 UPMU data reduction

A charge cut of 8,000 $\leq$ Q (total ID charge) < 1,750,000 (3,000 $\leq$ Q < 800,000 for SK-II) p.e.s was applied. At very high ID charge corresponding to $\approx$ 1, 750,000 (800,000 for SK-II) p.e.s the ID electronics becomes saturated causing the muon fitters fail. To isolate the rate of about one neutrino induced upward going muon per day from the remaining background of about a million cosmic ray muons, we used

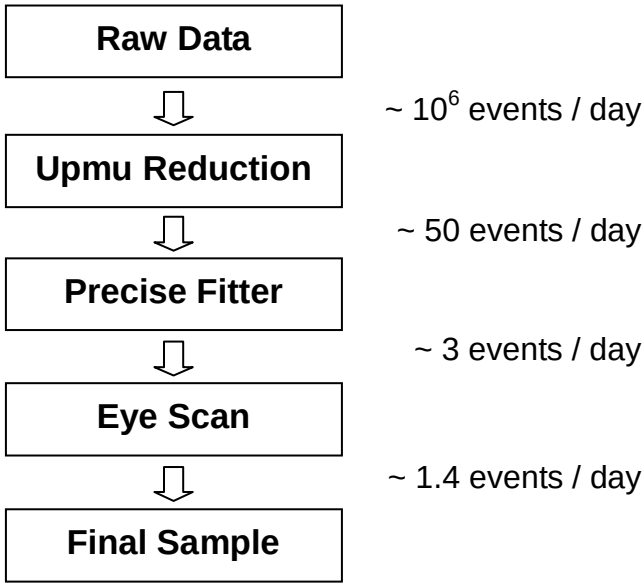

Figure 4.9 The procedure to isolate upmu events.

seven different muon fitters. Some of these fitters were specialized to fit stopping muons, others were specialized for through-going muon events, and some of them were specialized to fit muon events with Bremsstrahlung. The 7 fitters used are listed below in the same order that an event pass through.

1. Stopmu1st

'Stopmu1st' is the first fitter used in the upmu reduction. It classifies topology of muon events into multiple muons, stopping muon and through-going muon using only OD information and passes the events to the next fitter without rejecting any event.

2. Muboy

'Muboy' is the only fitter which provides fitting results (entrance position and direction, goodness of fit, track length, number of track, etc) as well as classifying

muon topology (through-going muon, stopping muon, multiple muon and corner clipper). Most of the cosmic ray muon backgrounds were removed by this fitter.

3. Stopmu2nd

'Stopmu2nd' was specially designed to fit stopping muons and run on only those event s which were classified as stopping muons by 'Muboy' or 'Stopmu1st'.

4. Thrumu1st

'Thrumu1st' is a fast muon fitter specialized for through-going muon events.

5. Fstmu

'Fstmu' is another fitter specialized for through-going muons.

6. Thrumu2nd

'Thrumu2nd' is a fitter specialized to fit multiple muons and Bremsstrahlung muon events.

7. NNfit

'NNfit' is a fitter specialized for fitting Bremsstrahlung muon events.

The basic thing what the fitters do is to decide whether an event should be saved, rejected or passed to the next fitter.

- The events to be saved: if an event is classified as through-going or stopping muon by either 'Stopmu1st' or 'Muboy' in upward direction above fitter's goodness threshold, it is saved. If an event, which 'Muboy' passed to the next fitter, 'Stopmu2nd', is the one classified as stopping muon by either 'Stopmu1st' or 'Muboy', 'Stopmu2nd' saves it if it is classified as horizontal/upward or if it gives no-fit but 'Muboy' classifies it as horizontal. If an event is classified through-gong

or stopping by either ‘Stopmu1st’ or ‘Muboy’ and its direction is horizontal above goodness threshold, the event is tagged as ‘horizontal’ and saved for background contamination study.

- The events to be rejected: if an event is classified as downward direction above fitter’s goodness threshold by any fitter, then the event is rejected. Beside, corner clipper muon cut and double muon cut are applied, which are described below.

Conditions for corner clipper cut :

- ‘Muboy’ classifies the event as corner clipper above goodness threshold.
- ‘Muboy’ classifies the event as through-going or stopping and track length is less than 4 m and direction is downward above goodness threshold.

Conditions for double muon cut:

- Both ‘Muboy’ and ‘Stopmu1st’ classify an event as multiple muon.

- The events to be passed to the next fitter: if an event is fitted with low goodness value or the fitter cannot be run on the event, then it is passed to the next fitter.

Finally, if all fitter cannot fit it, then the event is rejected. However, if at least one fitter classify it as horizontal or upward, then it is saved. All events after the upward muon reduction, which contain many background events, were then passed to the precise fitter, which gives more accurate fitting results (direction, track length, momentum etc) about muon. The precise fitter is described in the next section. Table 4.6 show the percentage of saved events and rejected events for each step in upmu reduction estimated with SK-I Monte Carlo.

Table 4.6 Percentage of events saved or rejected at each fitter.

Fitter	% of events saved	% of events rejected
Stopmu1st	0 %	3.4 %
Muboy	9.0 %	93.5 %
Stopmu2nd	20.8 %	0.1 %
Thrumu1st	29.4 %	0.9 %
Fstmu	2.8 %	1.0 %
Thrumu2nd	2.9 %	0.9 %
NNfit	6.9 %	0.1 %
No fit by all fitter or not	28.2 %	0.1 %

4.3.2 Upmu Event Reconstruction

All events from the output of the upward-going muon reduction were passed to the precise fitter. The accurate muon vertex and direction are determined by the precise fitter and they are used for the neutrino oscillation analysis. Though the fitters in the upmu reduction give fit direction and entrance point, they are just designed to reject clear background and to reduce number of events to pass to precise fitter because precise fitter take long time to fit events.

The basic algorithm is identical to that used for the vertex and direction determination for single ring fully-contained and partially-contained events. The fitter assumes that the particle is a muon and the vertex position of the event is at the inner detector surface. However, when the muon produces an energetic electro-magnetic shower, the assumption of single non-showering muon does not give an accurate direction. For these events, the information of OD hit is used to determine the particle direction. The angular resolution of the fitter was estimated by comparing true muon direction and fitted direction using Monte Carlo and it was about 1.0° for both through-going and stopping muons.

Based on the information the precise fitter gives, we selected the events, which were fitted in upward direction, longer track length than 7 m in case of through-going muon and higher momentum than 1.6 GeV in case of stopping muon. Table 4.7 shows the upward-going muon detection efficiency after upmu reduction and precise fitter cut estimated using Monte Carlo.

Table 4.7 Upmu detection efficiency estimated using Monte Carlo.

Reduction step	**SK-II (%)**	**SK-I (%)**
Total	100	100
Reduction	97.7	99.3
Precise fitter (with direction and track length cut)	96.4	99.2

4.3.3 Upmu Eye-Scanning

The events, which passed through the cuts from the precise fitter, still contain some junk events not rejected by misfitting. To eliminate this kind of events, two independent physicists scanned the events by event display program. Finally, another upmu expert compared the judgment from the two physicists and make final decision about rejecting events. The eye-scanning is used just to reject the remaining backgrounds and never change the fitting results like direction, vertex or the stop/through-going judgment decided by the fitter.

4.3.4 Background Estimation from Cosmic Ray Muon

The main background for upward going muon is cosmic ray muons. Most of these events were rejected in the upmu reduction. After the reduction, the precise fitter gave more accurate fitting information and rejected downward going muon. The remaining backgrounds after the selection from the precise fitter were eliminated by eye-scanning. Nevertheless, there may still exist some background in near horizontal direction because of the finite fitter resolution and multiple scattering of muons in the nearby rock. Figure 4.10 shows the zenith angle distribution of upward muon candidates near the horizon ($-0.1 < \cos\theta < 0.1$ for stopping muon and $-0.1 < \cos\theta < 0.08$ for through-going muon) for two different region (that is, think rock region and thick rock region) in azimuth. The region, which shows negligible cosmic ray contamination in near horizontal direction, is the thick rock region. However, we can see the other region, that is, thin rock region have non-negligible contamination. The shape of zenith angle distribution of thin rock region above horizon was extrapolated by the following fitting function

$$f[\cos(\theta)] = p1 + e^{[p2 + p3\cos(\theta)]}$$

The cosmic ray contamination was estimated form the second term in the right of the above function.

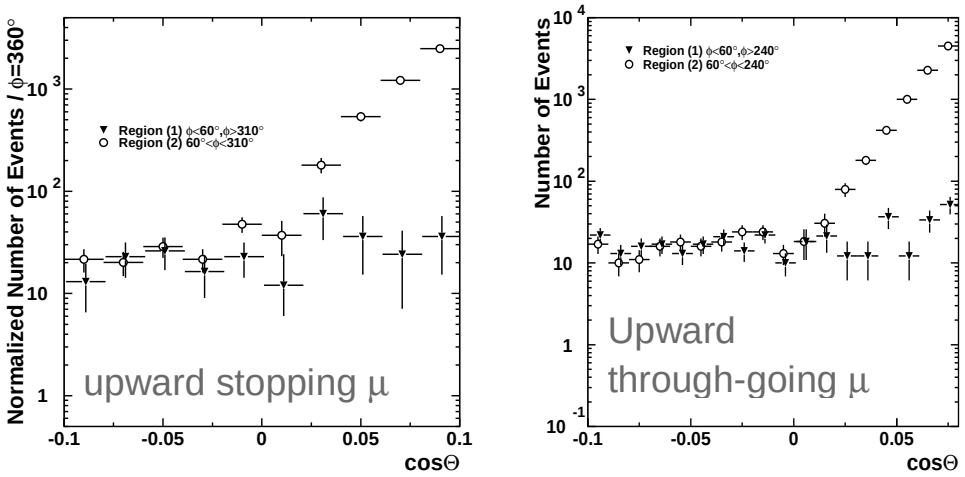

Figure 4.10 The zenith angle distribution of upward muon candidates near the horizon for two different regions in azimuth made with SK-I data. The white circles and the black inverted triangle are for thin and thick rock region, respectively.

Chapter 5

Atmospheric Neutrino Data

5.1 FC and PC Events

We have accumulated 1489.2 days of FC and PC data from May 17, 1996 to July 16, 2001. These are referred as SK-I data and compared with statistically larger samples of Monte Carlo events equivalent to 100 years of the SK-I detector exposure. After 2001 accident and reconstruction, we have accumulated 627.1 days of FC and PC data from Jan 16, 2003 to Mar 2, 2005. These are referred as SK-II data and compared with Monte Carlo equivalent to 60 years of the SK-II detector exposure. The Monte Carlo samples were processed by the same event selection and event reconstruction steps as the real events. Fully-contained events were divided into two sub-samples according to the reconstructed visible energy. We refer to the event sample below 1.33 GeV as sub-GeV, and above 1.33 GeV as multi-GeV. Fully-contained events were further divided into the events with single reconstructed Cherenkov ring and events with more than one ring. All single-sing events were classified as either e-like or μ-like based on the PID result. Lower energy cuts were applied only to the single-ring sample, P_e > 100MeV/c for a e-like and P_μ > 200MeV/c for μ-like. In addition, multi-ring events were used to study the atmospheric neutrino flux. Table 5.1 summarizes the number of observed events in th-

Table 5.1 The number of observed events in the sub-GeV and multi-GeV samples as well as the expected number of events in the absence of neutrino oscillations.

		SK-I		SK-II	
		Data	MC	Data	MC
Sub-GeV	Single-ring e-like	3353	2879.8	1447	1256.2
	Single-ring μ-like	3227	4212.8	1370	1782.8
	Multi-ring	2361	2791.7	1011	1199.1
Multi-GeV	Single-ring e-like	746	680.5	280	296.4
	Single-ring μ-like	651	899.9	278	390.1
	Multi-ring	1504	1891.6	642	767.0
PC		911	1129.6	325	461.2

-e sub-GeV, multi-GeV and PC samples as well as the expected number of events in the absence of neutrino oscillations.

A double ratio defined as $R \equiv (\mu/e)_{DATA}/(\mu/e)_{MC}$ was measured like following without oscillation effect in Monte Carlo prediction for sub-GeV events.

SK-I : $R_{sub-GeV} = 0.658 \pm 0.016 \pm 0.035$

SK-II : $R_{sub-GeV} = 0.667^{+0.026}_{-0.025} \pm 0.038$

A substantial fraction of muons in the multi-GeV energy range exit from the inner detector and are detected as PC events. The partially-contained event sample is estimated to be 97 % pure CC ν_μ interactions, even without requiring any particle identification or ring-number cuts. Therefore, we add FC single-ring and PC event totals when calculating R in the multi-GeV range. The double ratio R in the multi-

GeV energy range was measured like following without oscillation in Monte Carlo.

SK-I : $R_{multi-GeV+PC} = 0.702^{+0.032}_{-0.030} \pm 0.101$

SK-II : $R_{multi-GeV+PC} = 0.750^{+0.057}_{-0.052} \pm 0.065$

The double ratios of SK-I and SK-II agree well.

The up-down ratio, where U is the number of upward-going events ($-1 < \cos\Theta < -0.2$) and D is the number of downward-going events ($0.2 < \cos\Theta < 1$), is summarized in Table 5.2, where θ is zenith angle. While the ratio for e-like events is the consistent with 1, the μ-like up-down ratio for the multi-GeV data differs from 1 by more than 12 standard deviations.

Table 5.2 UP/DOWN ratio of fully-contained events.

		UP/DOWN ratio		
		SK-I	SK-II	SK-II / SK-I
Sub-GeV	e-like	1.11+0.04-0.04	0.97+0.06-0.06	0.88+/-0.06 (2.0σ)
	μ-like	0.77+0.03-0.03	0.84+0.05-0.05	1.09+/-0.08 (1.1σ)
Multi-GeV	e-like	0.96+0.09-0.08	1.07+0.16-0.14	1.11+/-0.18 (0.6σ)
	μ-like	0.48+0.05-0.04	0.40+0.05-0.04	0.87+/-0.15 (0.9σ)

5.2 UPMU events

The SK-I upward-going muon data used in this analysis were taken from May 1996 to July 2001. The detector live-time is 1645.9 days. The SK-II upward-going muon data were taken from Jan 5, 2003 to Mar 2, 2005. The detector live-time was 609 days. Figure 5.1 shows the event rates as a function of the elapsed days for SK-II upward going muons. The event rates for these samples are stable. Table 5.3 summarizes the number of observed events in the upward-going muon data sample and Monte Carlo. Upmu event rate are consistent between SK-I and SK-II for both data and MC.

Fewer upward stopping muons were observed than predicted, while the observed number of upward through-going muons was consistent with the theoretical prediction within the errors.

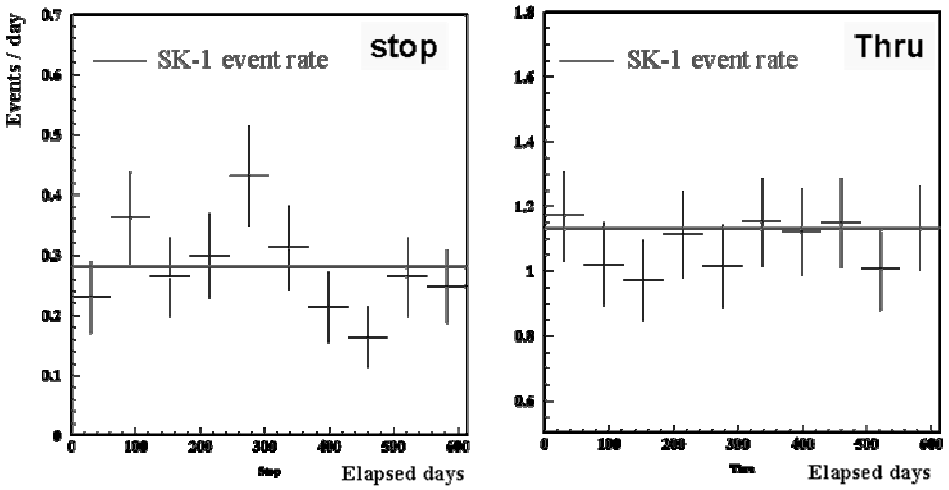

Figure 5.1 Event rate as a function of elapsed days of SK-II data. SK-I event rates were shown as a reference by line.

Table 5.3 The number of observed events in the upward-going muon data sample and Monte Carlo. The numbers in 100 years SK-I MC were normalized to SK-II MC live-time of 60 years.

Fitted event class	Data		MC	
	SK-I	SK-II	SK-I	SK-II
Stop mu	417.7	170	9504	9285
(events / day)	(0.28)	(0.28)		
Thru mu	1841.6	662	22374	22022
(events / day)	(1.13)	(1.09)		

Chapter 6

Two Flavor Neutrino Oscillation Analysis

6.1 Overview

In the previous atmospheric neutrino analysis [2-5], a significant deficit of atmospheric muon neutrino interactions was observed compared to the expectation and it was interpreted as neutrino oscillation. Oscillation between electron neutrinos and muon neutrinos cannot explain the data because the number of observed upward-going electron neutrinos is consistent with null-oscillation expectation. The other hand, atmospheric ν_μ oscillation into ν_τ can explain the ν_μ disappearance well, as the majority of the flux is below the 3.5 GeV neutrino energy, which is the threshold for charged current τ production. So previously the atmospheric neutrino data were analyzed based on hypothesis of pure 2 flavor neutrino oscillation between muon neutrino and tau neutrino and the best fit parameters of $\nu_\mu \leftrightarrow \nu_\tau$ oscillation were established using the whole SK-I atmospheric neutrino data [35]. Also in this study, the pure 2 flavor oscillation was assumed but to measure the oscillation parameters more precisely, the new strategy of binning, which is one of the oscillation analysis procedures, was applied and the combined analysis of Super-Kamiokande-I and

Super-Kamiokande-II data was accomplished.

6.2 Oscillation Analysis with New Binning

6.2.1 New binning

In the oscillation analysis, the data and Monte Carlo are classified by reconstructed event type, momentum, and zenith angle. The fully-contained (FC) sample is divided into sub-GeV and multi-GeV according to the visible energy (E_{vis} < 1.33 GeV is for sub-GeV and E_{vis} > 1.33 GeV is for Multi-GeV), into single-ring and multi-ring by the number of reconstructed Cherenkov rings, and into *e*-like and μ-like by particle identification (PID) of the most energetic ring. Upward going muon events are divided into upward stopping and upward through-going according to the energy deposited in OD. Each category is divided further by momentum and zenith angle. In previous oscillation analysis [35], total 180 bins were used: 150 for the FC sample, 10 for PC sample, 20 for upward going muon sample.

In new binning, the PC sample is divided further into OD stopping and OD through-going according to energy deposited in OD, multi-ring *e*-like sample were added newly, and momentum of multi-GeV samples were divided more finely to increase sensitivity to oscillation parameters. The number of total bins has become 370 in this new binning strategy: 270 for FC sample, 80 for PC sample and 20 for upward-going muon sample. Figure 6.1 shows the schematic view of the old bins (180 bins) and new bins (370 bins).

6.2.2 Oscillation analysis method with new binning

The number of events of data in each bin is compared with expectation and the agreement between data and expectation is estimated by the following χ^2 statistic

using Poisson probability distribution.

$$\chi^2 = \sum_{i=1}^{370}\left[2\left(N_i^{\exp} - N_i^{obs}\right) + 2N_i^{obs}\ln\left(\frac{N_i^{obs}}{N_i^{\exp}}\right)\right] + \sum_{j=1}^{44}\left(\frac{\varepsilon^j}{\sigma_j}\right)^2$$

$$N_i^{\exp} = N_i^0 \cdot P(\nu_\mu \to \nu_\tau)\cdot(1+\sum_{j=1}^{46} f_j^i \cdot \varepsilon_j)$$

Where,

N_i^{obs} is the number of observed events in the i_{th} bin,

N_i^{exp} is the expected number of events taking into account the oscillation effect,

σ_i is the combined statistical uncertainties of the data and Monte Carlo simulation,

N_i^0 is the expected number of events predicted without neutrino oscillation,

ε^j is the systematic variation,

f^i_j is the fractional change in the predicted event rate in the i_{th} bin due to a variation of the parameter ε^j.

In the estimation of N_i^{exp}, systematic variations due to uncertainties in the neutrino flux model, neutrino cross section model, and detector response were taken into account. These uncertainties are represented by 46 parameters, ε^j, which are described in the next section.

The second sum in the χ^2 definition collects the contributions from variables which parameterize the systematic uncertainties in the expected neutrino rates but among the 46 parameters, only 44 parameters contribute because the two parameters ('the absolute normalization' and 'sample normalization of multi-ring e-like events') are regarded as free. During the χ^2 calculation, the systematic parameters, ε^j are varied to minimize χ^2 for each choice of oscillation parameters, $\sin^2 2\theta$ and Δm^2.

A global scan was made on a ($\sin^2 2\theta$, $\log\Delta m^2$) grid searching the point minimizing χ^2. Assuming a linear dependence of N_i^{exp} on the each systematic parameter, ε^j which minimize χ^2 is obtained by calculating $\partial\chi^2 / \partial\varepsilon^j = 0$ for each of the parameters ε^j. As a result, the minimization of χ^2 is equivalent to solving the following equation for k=1,

$$\left(\sum_{i=1}^{370} N_i^{obs} f_j^i f_k^i + \frac{1}{\sigma_j^2} \delta_{jk} \right) \varepsilon_k = \sum_{i=1}^{370} \left(\left(1 + (f\varepsilon)^2 \ldots\right) N_i^{obs} - N_i^{\exp} \right) f_j^i$$

where σ_j is the estimated uncertainty in the parameter ε^j .

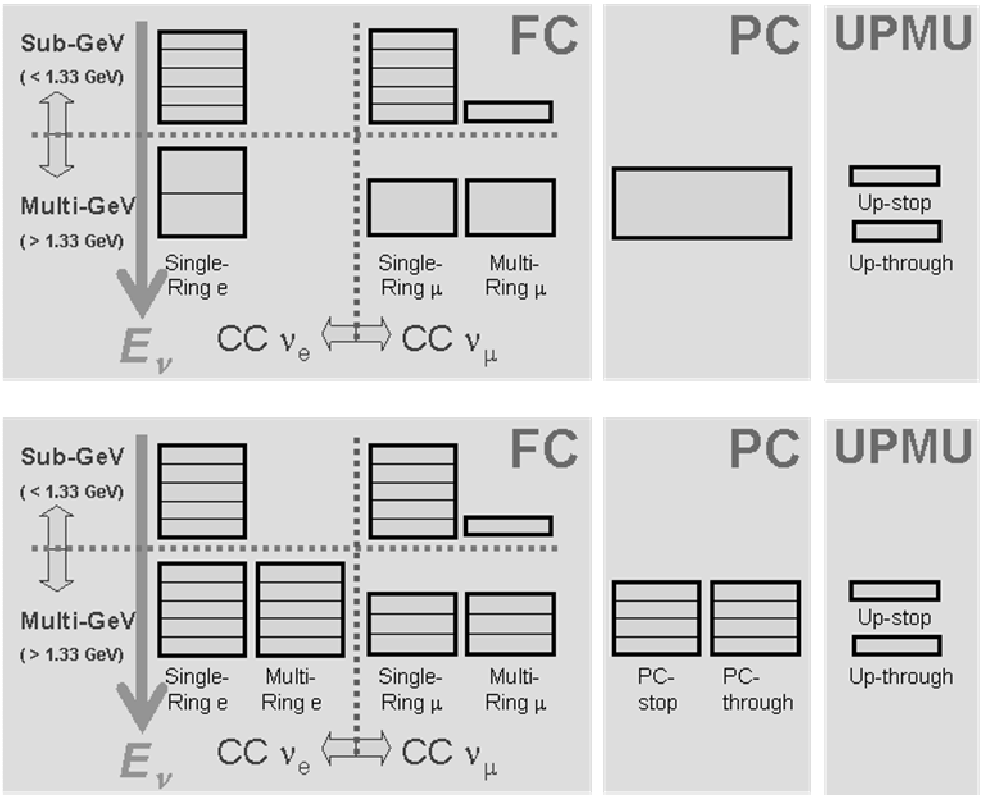

Figure 6.1 The schematic view of the binning. Each bin in this figure is divided further by 10 zenith angle bin. The top is the bins used in the old analysis (180 bins) and the bottom is the new bins (370 bins) used in this analysis.

Since this equation has non-linear terms for our χ^2 definition, an iteration method was used to obtain the approximate solution. The following data set were used in this analysis as mention at the chapter 5.

	SK-I		SK-II	
	Data	MC	Data	MC
FC, PC	1489.2 days	100 years	627.1 days	60 years
UPMU	1645.9 days	100 years	608.6 days	60 years

6.2.3 Systematic uncertainty terms used in the oscillation analysis

In this section, the 46 systematic parameter terms are described briefly. The estimated 1 σ for each parameter are shown in Appendices with the best fit values obtained from the combined analysis described in section 6.3.

Systematic uncertainties in atmospheric neutrino flux

- Absolute normalization ----- (1)

  Absolute normalization uncertainty comes from the uncertainty in the primary cosmic ray flux and hadronic interaction models. It was roughly estimated to be 20% below 100 GeV and 30% above 100 GeV. However, this parameter was treated as a free parameter in the analysis because of its large uncertainty.

- Flavor ratio ν_μ/ν_e ratio ($E_\nu < 5$ GeV) ----- (2)

  ν_μ/ν_e ratio ($E_\nu > 5$ GeV) ----- (3)

  The flavor ratio is predicted from the independent flux calculations. At the low energy, the uncertainty mainly comes from the estimation of pion spectrum in the

primary hadronic interactions, which affects decay probabilities of secondary muons in atmosphere. At high energy, the uncertainty mainly comes from the K/π production ratio.

- Anti-neutrino / neutrino ratio
  anti-ν_e / ν_e (E_ν < 10 GeV) ----- (4)
  anti-ν_e / ν_e (E_ν > 10 GeV) ----- (5)
  anti-ν_μ / ν_μ (E_ν < 10 GeV) ----- (6)
  anti-ν_μ / ν_μ (E_ν > 10 GeV) ----- (7)

  Systematic uncertainty of anti-neutrino to neutrino ratio comes from π^+/π^- ratio in hadronic interaction in the flux calculation.

- up / down ratio ----- (8)

  The neutrino flux below a few GeV has up/down asymmetry because of the rigidity cutoff by the geomagnetic field. The systematic uncertainty in the up/down ratio of atmospheric neutrino flux is derived from the treatment of the geomagnetic field in the calculation.

- horizontal / vertical ratio ----- (9)

  The source of the uncertainties in horizontal/vertical ratio of atmospheric neutrino flux depends on the neutrino energy. For relatively lower energy neutrinos below 10 GeV, the uncertainties come form the difference in 3-dimensional calculation method for each calculation. For higher energy neutrinos, the uncertainties are derived from the generated K/π ratio in hadronic interactions in the atmosphere. However, these uncertainties were treated as the correlated.

- K/π ratio ----- (10)

- Flight length of neutrino ----- (11)

  The uncertainty of flight length of neutrino is not related to flux but it affect on oscillation probabilities of neutrinos. The systematic uncertainty for upward-

going neutrinos is negligible but downward-going and horizontal-going neutrinos are affected largely by the uncertainty of the production height of the neutrinos. The systematic uncertainty in the calculation of the production height and neutrino flight length is measured by changing the density structure of atmosphere.

- Energy spectrum of primary cosmic ray ----- (12)

The spectrum of primary cosmic ray is well fit to the form E^{γ}. The spectral index for the primary proton flux used is γ=2.74. We assigned 0.05 for the uncertainty in the energy spectrum index above 100 GeV in the primary cosmic ray energy spectrum.

- Sample-by-sample normalization (FC Multi-GeV) ----- (13)
  (PC + Upward-stopping muon) ----- (14)

  Actually, the uncertainty of flux estimated from independent flux model depends on neutrino energy. Therefore, the uncertainties of absolute normalization and energy spectrum were not enough. So the uncertainties of the flux for Multi-GeV and PC+upward-stopping muon samples were introduced as sample-by-sample normalization.

- Normalization of multi-GeV multi-ring e-like events ----- (15)

- Uncertainty from solar activity ----- (16)

  Primary cosmic ray flux is affected by solar activity changing by about 11 years period. The effect of solar activity on the atmospheric neutrino flux calculation was taken into account. +/- 1 year of uncertainty was introduced to the modulation of solar activity.

Systematic uncertainties in neutrino interaction

- M_A in quasi-elastic scattering and single meson production ----- (17)

The value of M_A is set to be 1.11 based on experiment. The uncertainty of this parameter makes effect on angular correlation between incident neutrino and out-going lepton.

- Model dependence quasi-elastic scattering ----- (18)
  deep inelastic scattering ----- (19)

- Cross section quasi-elastic scattering ----- (20)
  single meson production ----- (21)
  deep inelastic scattering ----- (22)
  coherent π cross section ----- (23)

- Neutral current / charged current ratio ----- (24)

- Nuclear effect in ^{16}O ----- (25)

  In neutrino interaction with nucleons in ^{16}O, the Fermi motion of the nucleons and Pauli Exclusion Principle are taken into account. The nucleons are treated as quasi-free particles using the relativistic Fermi gas model of Smith and Moniz. The momentum distribution of the nucleons is assumed to be flat up to the fixed Fermi surface momentum of 225 MeV/c and the nucleon potential is set to 27 MeV/c. These configurations and the calculation of kinematics in neutrino interaction are thought to have uncertainty.

- Nuclear effect (π spectrum) ----- (26)

  The uncertainty is related to the interaction of π and nucleons in ^{16}O.

- Charged current ν_τ interaction ----- (27)

  The number of charged current ν_τ interactions in the FC single-ring e-like samples was considered. The systematic uncertainty in the cross section of charged current ν_τ interaction is estimated from τ analysis in Super Kamiokande.

Systematic uncertainties in event section

- Reduction efficiency FC ----- (28)
  PC ----- (29)
  Upward-going muon ----- (30)

  Systematic uncertainty of reduction efficiency was estimated by comparing the distribution of each cut variable of the data with that of the Monte Carlo.

- FC/PC relative normalization ----- (31)

  This uncertainty is mainly from FC/PC separation made by OD hits. Fiducial volume, non-neutrino background and hadron simulation also affect on this uncertainty.

- Separation of upward-stopping and through-going muon ----- (32)

  This separation is done by the number of hits in OD PMTs within 8 m from the reconstructed exit point (NHITEX). The uncertainty was estimated by comparing NHITEX distribution of the data with that of Monte Carlo.

- Separation PC stop/through events ----- (33)

- Hadron simulation (contamination of NC in single-ring μ-like events) ----- (34)

- Non-neutrino background flasher for *e*-like ----- (35)
  cosmic ray muon in μ-like events ----- (36)

- Background contamination multi-GeV single-ring e-like events ----- (37)
  multi-GeV multi-ring e-like events ----- (38)

- Background subtraction upward through-going muon ----- (39)
  upward stopping-going muon ----- (40)

The background subtraction of upward-going muon events in the most horizontal zenith angle bin was described in 4.3.4.

Systematic uncertainties in event reconstruction

- Single-ring / multi-ring separation ----- (41)

  This uncertainty was estimated by comparing the evaluation function distribution of data with that of Monte Carlo.

- Particle identification single-ring events ----- (42)
  multi-ring events ----- (43)

  The error for the particle identification was estimated by comparing the likelihood distribution of the data with that of Monte Carlo.

- Energy calibration ----- (44)

  The absolute energy scale was estimated with several sources over a wide energy range. The uncertainty of the absolute energy reconstruction was less than 2 %.

- Energy cut for upward-stopping muon ----- (45)

  The systematic uncertainty of an energy cut (P > 1.6 GeV), which is applied to upward-stopping muon samples to isolate well reconstructed events, was estimated by varying the energy scale by 2 %.

- Up/down symmetry of energy calibration ----- (46)

  The difference of the energy scale for upward-going and downward-going event was measured using decay electrons from cosmic ray stopping muons.

6.2.4 Study of sensitivity to finer binning with SK-I MC

The effect of the new binning on the 2 flavor analysis was tested using Monte Carlo before applying it to the real data. To do it, the number of events in each bin was calculated using 100 years SK-I MC and was scaled to have the live-time of 5 years, 20 years and 80 years respectively. The numbers of real data events in each bin were replaced with that of the scaled MC. To investigate sensitivity for various oscillation parameters regions, four different set of parameters, that is, ($\sin^2 2\Theta$, Δm^2) = (0.85, 5.6×10^{-3}), (0.85, 1.0×10^{-3}), (0.85, 2.5×10^{-3}), (1.0, 2.5×10^{-3}) were applied when making the virtual data, which was made from the scaled MC. With these virtual data, the 2 flavor oscillation analysis was done in the old binning (180 bins) and the new binning (370 bins).

Figure 6.2 shows the 90% C.L. allowed regions obtained with the virtual data in 180 bins and 370 bins. It is clear that the analysis in the new binning constrain Δm^2 more strongly for all oscillation parameters regions and live-time. With this clear improvement in MC, we decided to apply this new binning to real data analysis.

6.2.5 Result with SK-I data and SK-II data separately

SK-I real data were analyzed in the new binning with the method described in 6.2.2. The minimum χ^2 value, χ^2_{min} = 376.5 / 367 DOF, was obtained at ($\sin^2 2\theta = 1.00$, Δm^2 = 2.5×10^{-3} eV^2). Including the unphysical region ($\sin^2 2\theta > 1$) in the scan, the minimum χ^2 value, χ^2_{min} = 376.1 / 367 DOF is located at ($\sin^2 2\theta = 1.03$, Δm^2 = 2.5×10^{-3} eV^2). The minimum χ^2 in the unphysical region is lower than that in the physical region by 0.44. The allowed oscillation parameter region corresponding to the 68%, 90% and 99% confidence level are shown in Figure 6.3 (a) and the contour of 90% confidence level was compared with that of the old analysis using 180 bins in Figure 6.3 (b). Assuming no oscillation, that is, ($\sin^2 2\theta = 0$, Δm^2 = 0), χ^2 value is 795.7 / 369 DOF. The 90 % C.L allowed region of the oscillation parameters is also

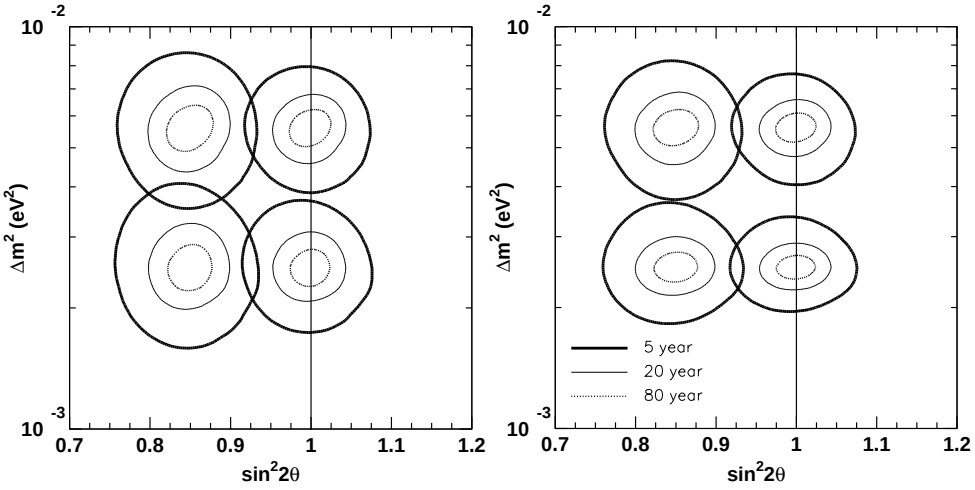

(a) 180 bins (b) 370 bins

Figure 6.2 Result of sensitivity study to binning effect. 90 % C.L allowed region obtained with the virtual data using 180 and 370 bins are shown for various oscillation parameter region and live-time.

estimated by using FC single-ring sub-GeV below 400 MeV/*c*, FC single-ring sub-GeV above 400 MeV/*c*, FC single-ring multi-GeV, PC, FC multi-ring and UPMU events separately. The results are shown in Figure 6.4, which compare the old and new binning analysis. The finely binned samples, 'Multi-GeV','PC' and 'Multi-ring' make contribution to constrain Δm^2 region tightly. FC single-ring and UPMU events give no effect because their binning was defined same as the old. Table 6.1 summarized the best fit parameters and the allowed range of the oscillation parameters at 90% confidence level in old and new binning analysis. The same analysis was also done with SK-II data and 60 year SK-II MC. Figure 6.5 show the contours plot with all the samples combined and the 90% C.L. contour plot for each sub-sample.

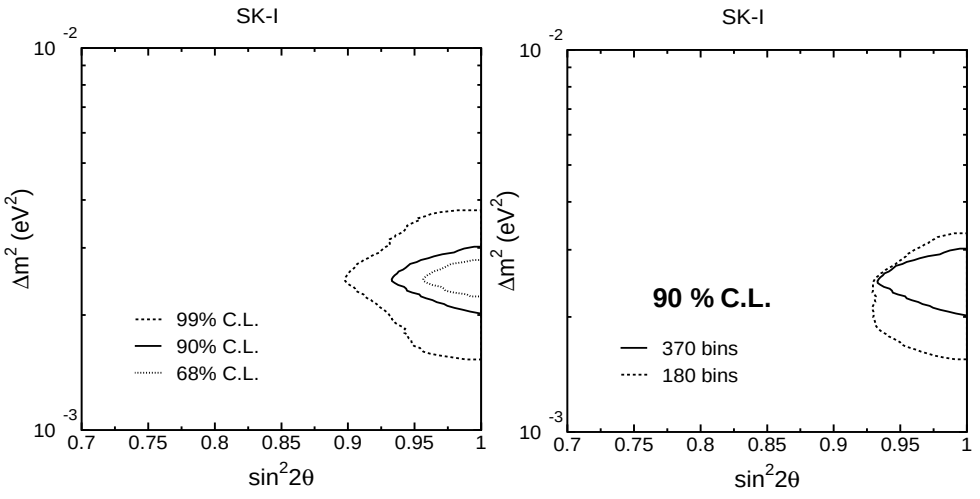

(a) 370 bins **(b) 180 vs. 370 bins**

Figure 6.3 The left plot (a) is the allowed oscillation parameter region corresponding to the 68%, 90% and 99% confidence level (C.L.) obtained with 370 bins. The right plot (b) is the comparison of the results with 180 bins and 370 bins for 90 % C.L.

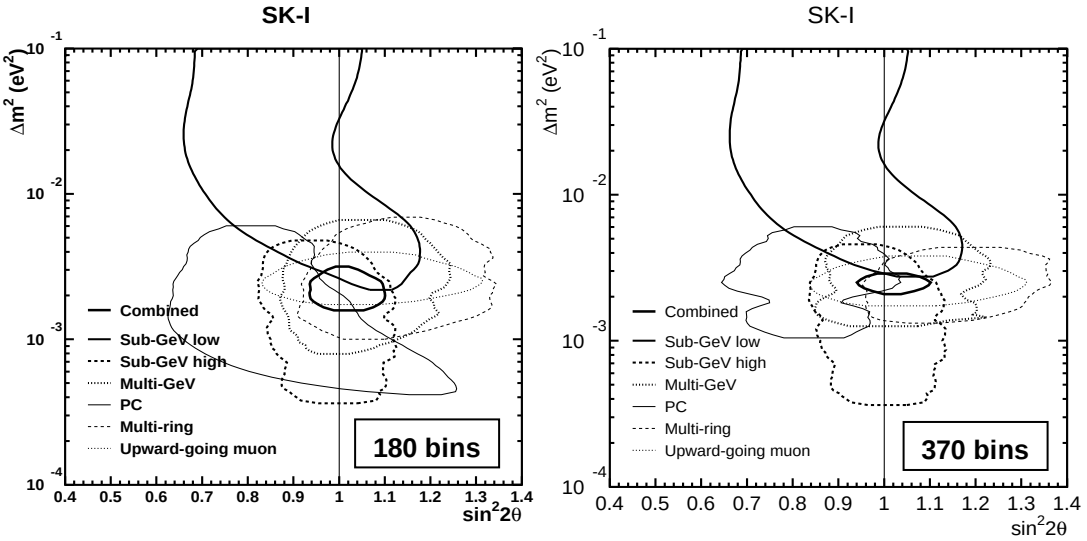

Figure 6.4 90 % C.L allowed region for each sub-sample. The left is the result with 180 bins and the right is 370 bins.

Table 6.1 Summary of the best fit parameters and the allowed range obtained with SK-I data.

	χ^2 / dof	$\sin^2 2\theta$	Δm^2 (eV^2)	90% C.L
180 bins				
Physical	174.9 / 177	1.00	2.11×10^{-3}	$\sin^2 2\theta > 0.92$
Unphysical	174.7 / 177	1.02	2.11×10^{-3}	$1.5\times10^{-3} < \Delta m^2 < 3.3\times10^{-3}$
370 bins				
Physical	376.5 / 367	1.00	2.48×10^{-3}	$\sin^2 2\theta > 0.93$
Unphysical	376.1 / 367	1.03	2.48×10^{-3}	$2.0\times10^{-3} < \Delta m^2 < 3.0\times10^{-3}$

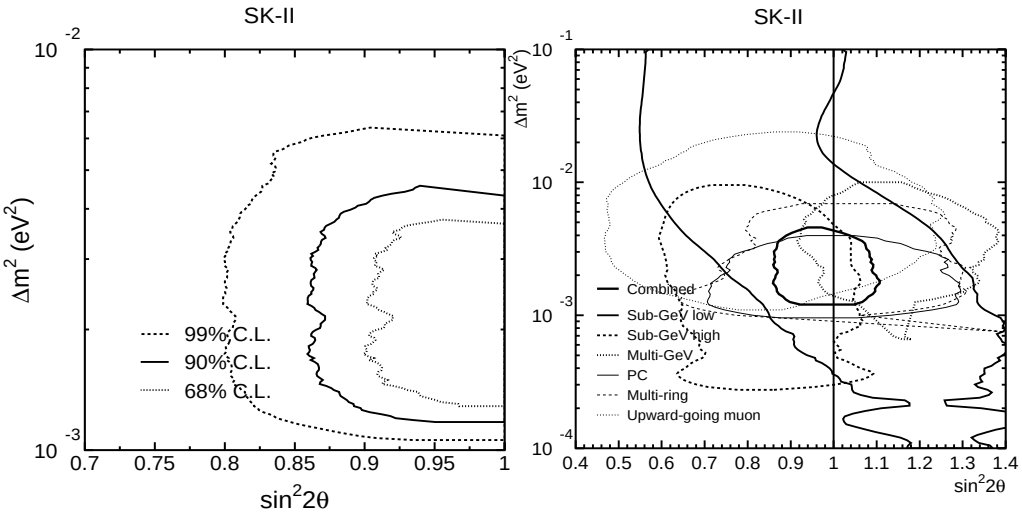

Figure 6.5 The allowed oscillation parameter region obtained with SK-II data. The left is the contour obtained with all the samples combined and the right is 90% C.L allowed region for each sub-sample.

6.3 Oscillation analysis with SK-I and SK-II combined

6.3.1 Combining strategy

SK-II data, which started to be taken from January, 2003, have different systematic effect in detector response. Therefore we do not mix SK-I and SK-II data directly. To combine SK-I and SK-II data in oscillation analysis, the number of bins were increased double for SK-II data. That is, total 740 bins were used in this analysis: 370 bins for SK-I and 370 bins for SK-II. The definition of 370 bins for SK-II is same as the one of SK-I. Though the systematic errors related to detector response are different between SK-I and SK-II, the systematic errors related to neutrino flux and neutrino interaction are identical for SK-I and SK-II. So the systematic errors of neutrino flux and interaction were treated in common in the combined analysis and in case of systematic errors of detector response and the uncertainty of solar activity were regarded as independent between SK-I and SK-II. In total, 64 systematic error terms were used in the combined analysis: 14 for neutrino flux, 12 for neutrino interaction, 19 for SK-I detector response, 19 for SK-II detector response and 2 for solar activity of SK-I and SK-II. The same oscillation analysis as section 6.2.2 was repeated with increased bins and systematic error terms.

6.3.2. Result of the combined analysis

In the combined analysis of SK-I and SK-II, the minimum χ^2 value, χ^2_{min} = 767.5 / 737 DOF, is located at ($\sin^2 2\theta = 1.00$, $\Delta m^2 = 2.5\times10^{-3}$ eV^2). Including the unphysical region ($\sin^2 2\theta > 1$) in the scan, the minimum χ^2 value is obtained at ($\sin^2 2\theta = 1.01$, $\Delta m^2 = 2.5\times10^{-3}$ eV^2). Contours corresponding to the 68%, 90% and 99% confidence level are shown in Figure 6.6 with comparison of SK-I result for 90% confidence level. Figure 6.7 shows the $\chi^2 - \chi^2_{min}$ distributions projected to $\sin^2 2\theta$ and Δm^2 axes, in which the minimum $\chi^2 - \chi^2_{min}$ values for each $\sin^2 2\theta$ and Δm^2 are plotted. Table 6.2

summarized the best fit parameters and the allowed range of the oscillation parameters at 90% confidence level in SK-I and the combined analysis. Assuming no oscillation, ($\sin^2 2\theta = 0$, $\Delta m^2 = 0$), a χ^2 value is 1306.8 / 739. The allowed neutrino oscillation parameters obtained by using each six sub-samples are shown in Figure 6.8. The allowed region contours from combined data show a little bit stronger constraint than SK-I. The best fit systematic parameters, which were fitted during χ^2 calculation, are shown in Table A1~10 in appendix with their 1σ uncertainty.

The zenith angle distributions of the FC, PC and upward−going muon samples are shown in Figure 6.9 and 6.10. The data (dot) are compared with the Monte Carlo expectation assuming no oscillations (box) and the best-fit expectation for $\nu_\mu \leftrightarrow \nu_\tau$ oscillations (line). The $\nu_\mu \leftrightarrow \nu_\tau$ oscillation hypothesis provides a consistent explanation of the full data set.

Table 6.2 Summary of the best fit parameters and the allowed range obtained from the combined analysis. SK-I result are shown for comparison.

	χ^2 / dof	$\sin^2 2\theta$	Δm^2 (eV^2)	90% C.L
SK-I				
Physical	376.5 / 367	1.00	2.48×10^{-3}	$\sin^2 2\theta > 0.93$
Unphysical	376.1 / 367	1.03	2.48×10^{-3}	$2.0\times10^{-3} < \Delta m^2 < 3.0\times10^{-3}$
SK-I+SK-II				
Physical	767.5 / 737	1.00	2.48×10^{-3}	$\sin^2 2\theta > 0.93$
Unphysical	767.5 / 737	1.01	2.48×10^{-3}	$2.1\times10^{-3} < \Delta m^2 < 3.0\times10^{-3}$

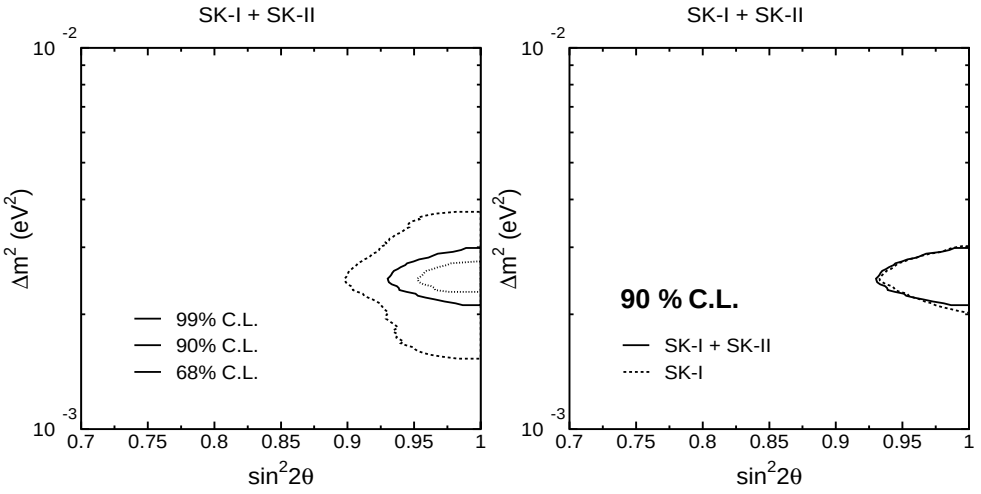

Figure 6.6 The left plot is the allowed oscillation parameters for $\nu_\mu \leftrightarrow \nu_\tau$ with the combined analysis of SK-I and SK-II. Three contours correspond to 68 %, 90 % and 99 % C.L. allowed region. The right plot is the comparison with the result of SK-I only analysis for 90 % C.L..

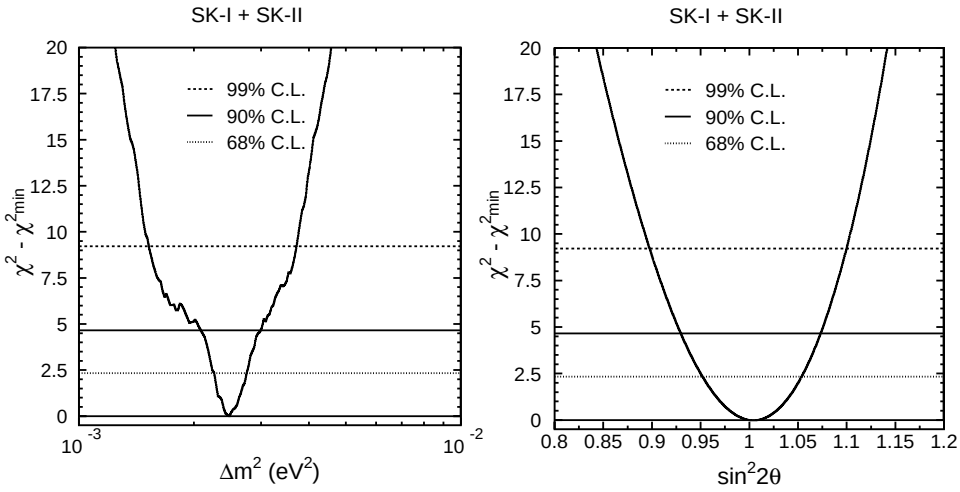

Figure 6.7 χ^2-χ^2_{min} distribution projected to $\sin^2 2\theta$ and $\triangle m^2$ axes resulted from SK-I and SK-II combined analysis.

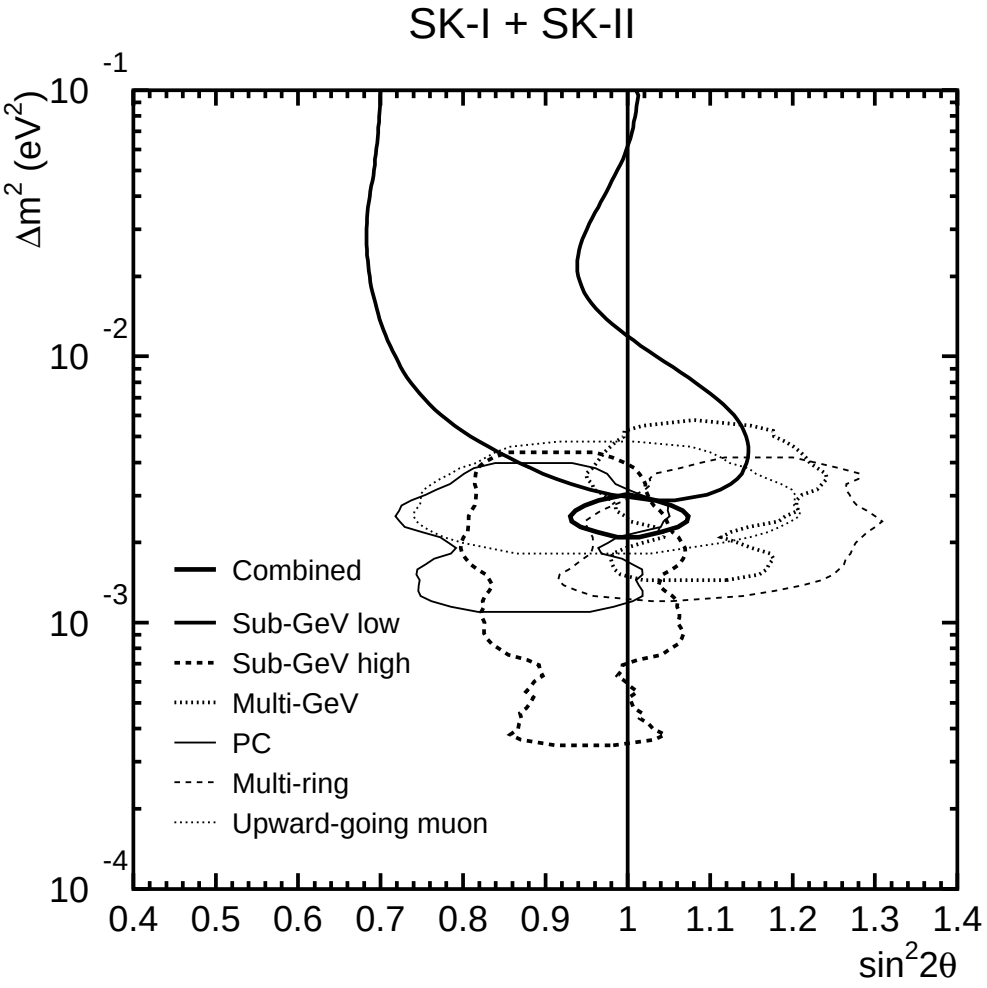

Figure 6.8 90 % confidence level allowed oscillation parameter regions of each sub-sample for $\nu_\mu \leftrightarrow \nu_\tau$ oscillations with SK-I and SK-II data combined.

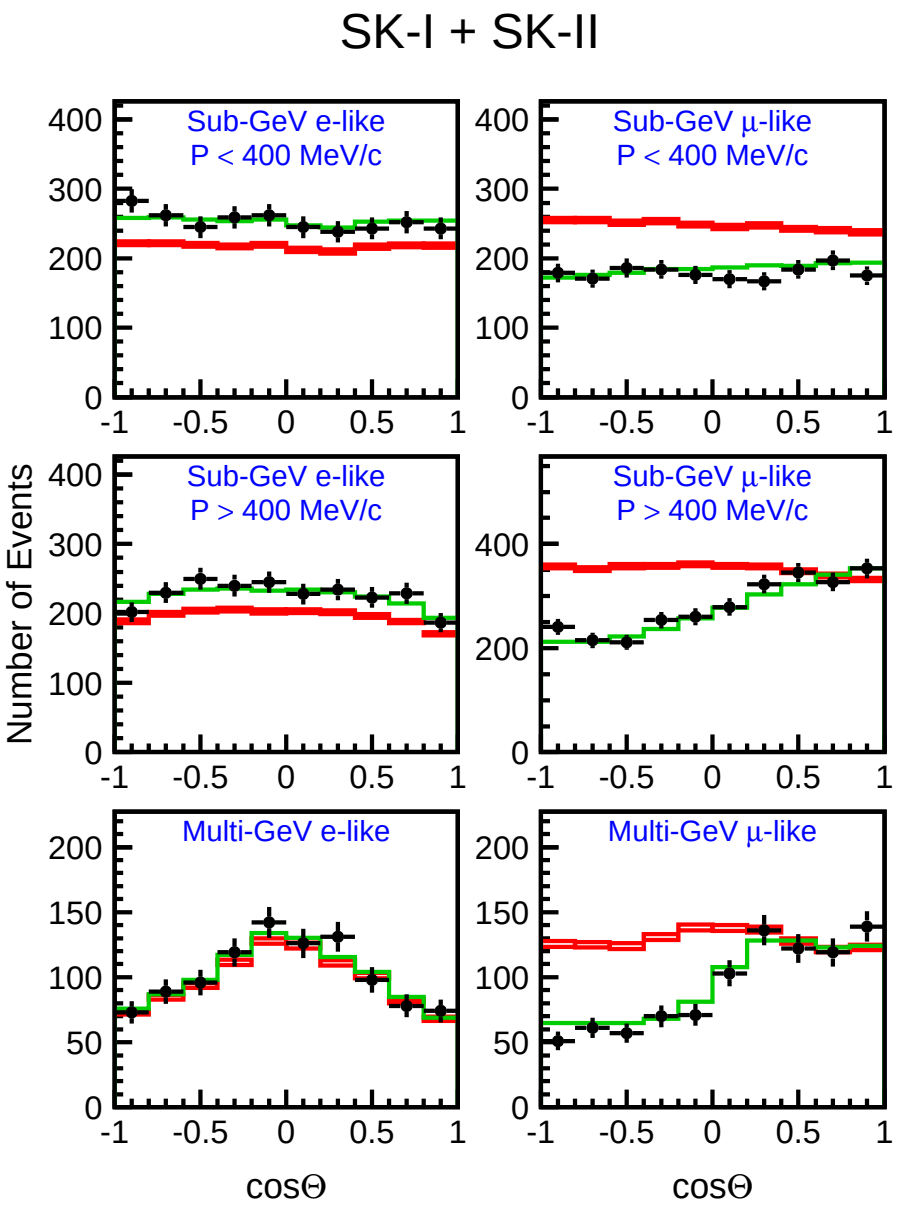

Figure 6.9 The zenith angle distribution of fully-contained sub-GeV and multi-GeV sample obtained by the combined analysis of SK-I and SK-II. The points show data, box histograms show the non-oscillated Monte Carlo and the lines show the best fit expectation obtained from the combined analysis.

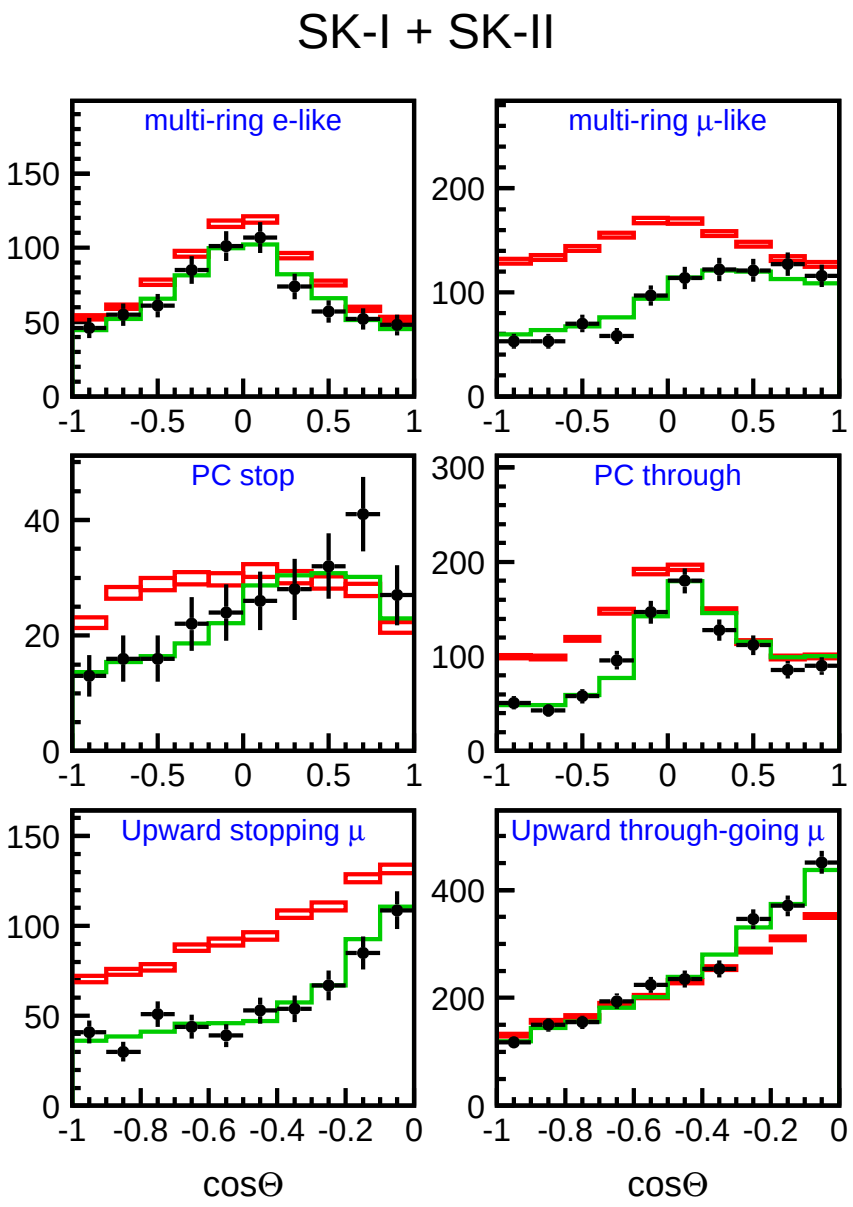

Figure 6.10 The zenith angle distribution of multi-ring, partially-contained and upward-going muon sample obtained by the combined analysis of SK-I and SK-II. The points show data, box histograms show the non-oscillated Monte Carlo and the lines show the best fit expectation obtained from the combined analysis.

6.3.3. Oscillation analysis with pseudo data to check the likeliness of the result obtained with real data

When we compared the allowed oscillation parameter region obtained from the combined analysis with that of just SK-I (refer to Figure 6.6), there was almost no improvement with the combined analysis. It was inferred that that was because the result with just SK-II data was on rather bad side unlikely so it couldn't contribute for the improvement by the combined analysis.

To check this inference, 20 set of pseudo data, which have the same live-time with real data and have the best-fit oscillation parameters ($\sin^2 2\theta = 1.0$, $\Delta m^2 = 2.5\times10^{-3}$ eV^2), were made using Monte Carlo for SK-I and SK-II, respectively. The oscillation analysis was done with this 20 set of pseudo data and the allowed regions of Δm^2 at 90% C.L were compared with that of real data.

The Figure 6.11 shows the width of Δm^2 region at 90% C.L obtained with 20 set of pseudo data and real data for SK-I and SK-II, respectively. The first bins in the graph of Figure 6.11 indicate the result of real data. We can see that the result of SK-I real data is on the lucky side and SK-II is rather unlucky. Thus we conclude that because of the unlucky situation of SK-II, the combined analysis of SK-I and SK-II made almost no improvement on the result of just SK-I.

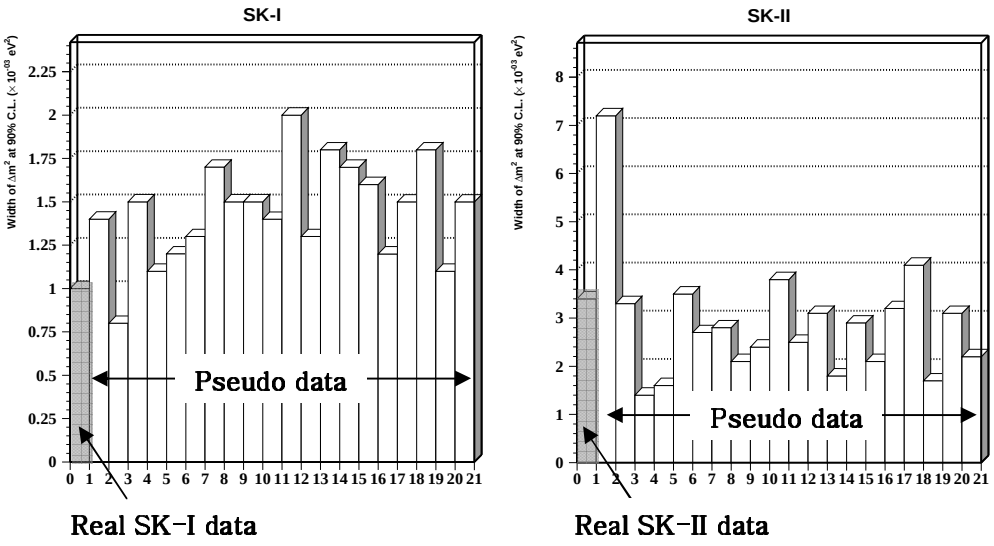

Figure 6.11 The width of Δm^2 region at 90% C.L obtained with 20 set of pseudo data and real data for SK-I (left) and SK-II (right), respectively to check the likeliness of the result of real data.

Chapter 7

Conclusion

Atmospheric neutrino events observed in Super-Kamiokande have the energy range approximately from 100 MeV to 10 TeV, and the neutrino flight-length from about 10 km to 13,000 km. These wide ranges of energy and flight length and high statistics enable us to study neutrino oscillations phenomena. In this study, the 2 flavor neutrino oscillation ($\nu_\mu \leftrightarrow \nu_\tau$) analysis was done using 1489.2 days exposure of SK-I fully-contained and partially-contained events, 1645.9 days of SK-I upward-going muon events, 627.1 days of SK-II fully-contained and partially contained events, and 608.6 days of SK-II upward-going muon events.

SK-II detector has half density of ID (inner detector) PMTs compared to SK-I and the PMTs are covered with acrylic covers to prevent chain reaction of PMT implosion. As SK-II has different detector configuration and responses from SK-I, some cut variables in data reduction were tuned and some reconstruction algorithm were modified in SK-II. The systematic uncertainties related to SK-II data reduction and reconstruction were estimated again and SK-II yielded consistent detection efficiency and oscillation analysis result with SK-I. To investigate any possible position dependence of SK water quality, the additional light injectors (LIs) were installed in 7 different positions (one on the top of the tank, five on the barrel and one on the bottom) and started to inject light from 8 different positions of the tank since the beginning of SK-II while only one injector on the top was used in SK-I. However, the

position dependence of the water quality was not seen in the result obtained from the upgraded LI system. Therefore the position dependence effect of the water quality was not applied in the neutrino data analysis.

The oscillation parameters ($\sin^2 2\theta$, Δm^2) between ν_μ and ν_τ were constrained utilizing the zenith angle and energy dependent deficit observed in atmospheric muon neutrino data. Especially it was shown that the determination of Δm^2 allowed region is improved much by dividing momentum bins of fully-contained multi-GeV and PC samples further. Oscillation analysis was done with SK-I data, SK-II data and combined data of SK-I and SK-II in the new finer binning, which was proved more sensitive to constraining the oscillation parameter, Δm^2. The results with the above three kinds of data set were consistent each other. The best fit oscillation parameters obtained with the combined data set are $\sin^2 2\theta = 1.00$ and $\Delta m^2 = 2.5 \times 10^{-3}$ eV^2 with χ^2/DOF = 767.5/737. The oscillation parameters are constrained as $\sin^2 2\theta > 0.93$ and $2.1 \times 10^{-3} < \Delta m^2 < 3.0 \times 10^{-3}$ at 90% C.L. with the combined data set. Zenith angle distribution of the observed atmospheric neutrinos in Super Kamiokande is explained well at the best fit expectation obtained from pure $\nu_\mu \leftrightarrow \nu_\tau$ oscillation analysis.

The oscillation parameters can also be constrained by *L*/*E* dependent oscillation analysis of FC and PC samples. This independent study yielded consistent result [40]. Though 2 flavor $\nu_\mu \leftrightarrow \nu_\tau$ oscillation is dominant, other sub-dominant effect such as θ_{13} and solar terms (θ_{12} and Δm_{12}^2) might be observable in the atmospheric neutrinos in Super Kamiokande. We are making effort to detect this small effect. To achieve that, the neutrino flux and interaction should be understood more accurately.

Appendix Tables

Table A1. Systematic errors in neutrino flux (1)

(common to SK-I and SK-II)

			σ (%)	Best-fit
Absolute normalization			Free	7.2
$(\nu_\mu + \text{anti-}\nu_\mu)/(\nu_e + \text{anti-}\nu_e)$	E_ν < 5 GeV		3.0	-2.7
	E_ν > 5 GeV		3.0[a]	2.7
$\text{anti-}\nu_e/\nu_e$	E_ν < 10 GeV		5.0	2.0
	E_ν > 10 GeV		5.0[b]	-0.9
$\text{anti-}\nu_\mu/\nu_\mu$	E_ν < 10 GeV		5.0	-0.8
	E_ν > 10 GeV		5.0[c]	2.3
Up/down	< 400 MeV	e-like	0.5	0.1
		μ-like	0.8	0.2
	> 400 MeV	e-like	2.1	0.6
		μ-like	1.8	0.5
	Multi-GeV	e-like	1.5	0.4
		μ-like	0.8	0.2
	PC		0.4	0.1
	Sub-GeV multi-ring μ		0.8	0.2
	Multi-GeV multi-ring μ		0.7	0.2

[a]Energy dependent error linearly increasing with $\log E_\nu$ from 3.0% at 5 GeV to 15% at 100 GeV

[b]Energy dependent error linearly increasing with $\log E_\nu$ from 5.0% at 10 GeV to 10% at 100 GeV

[c]Energy dependent error linearly increasing with $\log E_\nu$ from 5.0% at 10 GeV to 10% at 100 GeV

Table A2. Systematic errors in neutrino flux (2)

(common to SK-I and SK-II)

			σ (%)	Best-fit
Horizontal/vertical	< 400 MeV	*e*-like	0.3	0.1
		μ-like	0.3	0.1
	> 400 MeV	*e*-like	1.2	0.5
		μ-like	1.2	0.5
	Multi-GeV	*e*-like	2.8	1.1
		μ-like	1.9	0.8
	PC		1.4	0.6
	Sub-GeV multi-ring μ		1.5	0.6
	Multi-GeV multi-ring μ		1.3	0.5
K/π ratio			20[a]	-2.7
L_ν (production height)			10[b]	1.1
Energy spectrum			0.05[c]	0.045
Sample-by-sample	FC Multi-GeV		5.0[d]	-7.3
	PC+upward stopping μ		5.0	-5.8

[a]20% uncertainty in K/p ratio in hadronic interaction in the atmosphere.

[b]10% uncertainty in the atmospheric density structure.

[c]0.05 uncertainty in the spectral index of the primary cosmic ray above 100 GeV.

Table A3. Systematic errors in neutrino interaction
(common to SK-I and SK-II)

	σ (%)	Best-fit
M_A in quasi-elastic and single-π	10[a]	3.4
Quasi-elastic scattering (model dependence)	1.0[b]	-0.8
Quasi-elastic scattering (cross-section)	10	9.4
Single-meson production (cross-section)	10	-3.1
Multi-π production (model dependence)	1.0[c]	1.46
Multi-π production (cross-section)	5.0	-1.6
Coherent π production	30	1.0
NC/CC ratio	20	-7.8
Nuclear effect in ^{16}O	30[d]	-6.9
Energy spectrum of pions	1.0[e]	0.36
Charged current ν_τ interaction	30[f]	1.7
Hadron simulation	1.0[h]	-0.25

[a]10% uncertainty in the axial vector mass, M_A value.

[b]Difference from the model, S.K.Singh and E.Oset, is set to 1.0.

[c]Difference from the model, A.Bodek and U.K.Yang, is set to 1.0

[d]30% uncertainty in the mean free path of hadron in the ^{16}O nucleus.

[e]Difference in the predicted pion energy spectrum by two interaction models (Neut and Nuance) was taken.

[f]30% uncertainty assumed for the CC ν_τ interaction cross-section.

[h]Difference from Fluka model

Table A4. Systematic errors in event section

(For only SK-I)

			σ (%)	Best-fit
FC reduction			0.2	0.0
PC reduction			2.6	1.0
Detection efficiency	upward stopping μ		1.3	0.0
	upward through-going μ		0.5	0.0
FC/PC separation			0.9	-0.4
Non-ν BG	Sub-GeV	*e*-like	0.4	0.0
		μ-like	0.1	0.0
	Multi-GeV	*e*-like	0.2	0.0
		μ-like	0.1	0.0
	PC		0.2	0.0
Upward stopping/through-going μ separation			0.4	0.0
Relative normalization of PC stop/through			9.6	4.7
BG subtraction of upward through-going μ			3.0	-0.2
BG subtraction of upward stopping μ			17	4.6
Non-ν_e contamination in multi-GeV single-ring *e*			14	-0.6
Non-ν_e contamination in multi-GeV multi-ring *e*			20	-2.8

Table A5. Systematic errors in event reconstruction

(For only SK-I)

			σ (%)	Best-fit
Ring separation	< 400 MeV	e-like	6.3	3.2
		μ-like	2.4	1.2
	> 400 MeV	e-like	3.4	1.7
		μ-like	1.3	0.7
	Multi-GeV	e-like	15.9	8.1
		μ-like	6.2	3.2
	Sub-GeV multi-ring μ		-3.7	-1.9
	Multi-GeV multi-ring μ		-7.2	-3.7
Particle identification	Sub-GeV	e-like	-0.6	0.1
		μ-like	0.6	-0.1
	Multi-GeV	e-like	-0.4	0.1
		μ-like	0.4	-1.0
	Sub-GeV multi-ring μ		3.4	0.3
	Multi-GeV multi-ring μ		4.7	0.4
Energy calibration for FC event			2.0	-0.2
Energy cut of upward stopping μ			1.1	-0.2
Up/down symmetry of energy calibration			0.6	0.0
Normalization of multi-GeV single-ring e			10	-0.05

Table A6. Systematic errors in event section

(For only SK-II)

			σ (%)	Best-fit
FC reduction			0.2	0.0
PC reduction			2.6	-1.9
Detection efficiency	upward stopping μ		1.9	0.1
	upward through-going μ		0.9	0.0
FC/PC separation			0.9	0.2
Non-ν BG	Sub-GeV	*e*-like	0.4	0.0
		μ-like	0.1	0.0
	Multi-GeV	*e*-like	0.2	0.0
		μ-like	0.1	0.0
	PC		0.2	0.0
Upward stopping/through-going μ separation			0.3	0.0
Relative normalization of PC stop/through			9.6	13.8
BG subtraction of upward through-going μ			3.0	1.1
BG subtraction of upward stopping μ			17	-11.4
Non-ν_e contamination in multi-GeV single-ring e			14	0.4
Non-ν_e contamination in multi-GeV multi-ring e			20	-1.8

Table A7. Systematic errors in event reconstruction

(For only SK-II)

			σ (%)	Best-fit
Ring separation	< 400 MeV	e-like	7.3	0.4
		μ-like	2.5	0.1
	> 400 MeV	e-like	3.0	0.1
		μ-like	1.2	0.1
	Multi-GeV	e-like	7.4	0.4
		μ-like	2.6	0.1
	Sub-GeV multi-ring μ		-3.3	-0.2
	Multi-GeV multi-ring μ		-3.5	-0.2
Particle identification	Sub-GeV	e-like	-0.9	0.0
		μ-like	0.9	0.0
	Multi-GeV	e-like	-0.3	0.0
		μ-like	0.3	0.0
	Sub-GeV multi-ring μ		16.8	10.2
	Multi-GeV multi-ring μ		6.7	4.1
Energy calibration for FC event			2.1	-2.0
Energy cut of upward stopping μ			1.1	0.0
Up/down symmetry of energy calibration			0.5	-0.1
Normalization of multi-GeV single-ring e			10	0.08

Table A8. Systematic errors in solar activity

	σ (%)	Best-fit
Solar activity (SK-I)	0.2[a]	0.02
Solar activity (SK-II)	0.5[b]	0.02

[a,b] + /- 1 year of solar activity uncertainty was taken into account.

Bibliography

[1] G. Barr *et al*., Phys. Rev. **D39**, 3532 (1989); V. Agrawal, *et al*., Phys. Rev. **D53**, 1313 (1996); T. K. Gaisser and T.Stanev, Proc. 24th Int. Cosmic Ray Conf. (Rome) Vol. 1 694 (1995)

[2] Y. Fukuda et al. (Super-Kamiokande), Phys. Lett. **B436**, 33 (1998), hep-ex/9805006.

[3] Y. Fukuda et al. (Super-Kamiokande), Phys. Lett. **B436**, 33 (1998), hep-ex/9805006.

[4] Y. Fukuda et al. (Super-Kamiokande), Phys. Rev. Lett. **82**, 2644 (1999), hep-ex/9812014.

[5] Y. Fukuda et al. (Super-Kamiokande), Phys. Lett. **B467**, 185 (1999), hep-ex/9908049.

[6] G. Battistoni et al., Astropart. Phys. **12**, 315 (2000), hepph/9907408.

[7] M. Honda, T. Kajita, K. Kasahara, and S. Midorikawa, Phys. Rev. **D64**, 053011 (2001), hep-ph/0103328.

[8] Y. Tserkovnyak, R. Komar, C. Nally, and C. Waltham, Astropart. Phys. **18**, 449 (2003).

[9] Y. Liu, L. Derome, and M. Buenerd, Phys. Rev. **D67**, 073022 (2003), astro-ph/0211632.

[10] G. Battistoni, A. Ferrari, T. Montaruli, and P. R. Sala (2003), hep-ph/0305208.

[11] J. Wentz et al., Phys. Rev. **D67**, 073020 (2003), hepph/0301199.

[12] J. Favier, R. Kossakowski, and J. P. Vialle, Phys. Rev. **D68**, 093006 (2003), astro-ph/0305460.

[13] M. Honda, T. Kajita, K. Kasahara, and S. Midorikawa, Phys. Rev. **D70**, 043008 (2004), astro-ph/0404457.

[14] G. D. Barr, T. K. Gaisser, P. Lipari, S. Robbins, and T. Stanev, Phys. Rev. **D70**, 023006 (2004), (Also, private communication with the authors. A slightly different flux from the one discussed in the paper is used in the present analysis.), astroph/0403630.

[15] M. Honda, T. Kajita, K. Kasahara, and S. Midorikawa, Phys. Rev. **D52**, 4985 (1995), hep-ph/9503439.

[16] V. Agrawal, T. K. Gaisser, P. Lipari, and T. Stanev, Phys. Rev. **D53**, 1314 (1996), hep-ph/9509423.

[17] J. Alcaraz et al. (AMS), Phys. Lett. **B490**, 27 (2000).

[18] T. Sanuki et al., Astrophys. J. **545**, 1135 (2000), astroph/0002481.

[19] P. Lipari, Nucl. Phys. B (Proc. Suppl.) **81**, 159 (2001).

[20] B. Pontecorvo, JETP, 6, 429 (1958); Z. Maki, M. Nakagawa and S. Sakata, Prog. Theor. Phys. 28, 870 (1962).

[21] C. H. Llewellyn Smith, Phys. Rept. **3**, 261 (1972).

[22] R. A. Smith and E. J. Moniz, Nucl. Phys. **B43**, 605 (1972).

[23] D. Rein and L. M. Sehgal, Ann. Phys. **133**, 79 (1981).

[24] D. Rein, Z. Phys. **C35**, 43 (1987).

[25] T. Kitagaki et al., Phys. Rev. **D34**, 2554 (1986).

[26] S. K. Singh, M. J. Vicente-Vacas, and E. Oset, Phys. Lett. **B416**, 23 (1998).

[27] M. H. Ahn et al. (K2K), Phys. Rev. Lett. **90**, 041801 (2003), hep-ex/0212007.

[28] D. Rein and L. M. Sehgal, Nucl. Phys. **B223**, 29 (1983).

[29] M. Gluck, E. Reya, and A. Vogt, Z. Phys. **C67**, 433 (1995).

[30] M. Nakahata et al. (KAMIOKANDE), J. Phys. Soc. Jap. **55**, 0 3786 (1986).

[31] T. Sjostrand, Comput. Phys. Commun. **82**, 74 (1994).

[32] R. Woods and D. Saxon, Phys, Rev. **95**, 577 (1954).

[33] L. L. Salcedo, E. Oset, M. J. Vicente-vacas, and C. Garcia-Recio, Nucl. Phys. **A484**, 557 (1988).

[34] G. Rowe, M. Salomon, and R. H. Landau, Phys. Rev. **C18**, 584 (1978).

[35] Y.Asie et al. (Super-Kamiokande), Phys. Rev. D **71**, 112005 (2005), hep-ex/0501064.

[36] S.Fukuda et al. The Super-Kamiokande Detector, Nucl. Instrum. Meth. **A501**(2003) 418-462.

[37] D. Ashery et al., Phys. Rev. **C23**, 2173 (1981).

[38] E.Davis, *Machine Vision : Theory, Algorithms, Practicalities* (Academic Press, San Diego, 1997).

[39] S.Kasuga et al., Phys. Lett. **B374**, 238 (1996)

[40] Y.Ashie, et al., Phys.Rev.Lett. **93** (2004).

[41] M.B.Smy et al. (Super-Kamiokande), Phys. Rev. **D69**, 011104 (2004), hep-ex/0309011.

[42] S.N.Ahmed et al. (SNO), Phys.Rev.Lett. **92**, 181301 (2004), nucl-ex/0309004.

[43] K.Eguchi et al. (KamLAND), Phys.Rev.Lett. **90**, 021802 (2003), hep-ex/0212021.

[44] E.Aliu et al. (K2K), Phys.Rev.Lett. **94**, 081802 (2005), hep-ex/0411038.

A Measurement of $\nu_\mu \leftrightarrow \nu_\tau$ Oscillation Parameters Using Atmospheric Neutrino Observed in Super Kamiokande-I and Super Kamiokande-II

서현관
성균관대학교 물리학과

Abstract

수퍼 카미오칸데에서 검출된 대기 뮤온 중성미자의 부족은 $\nu_\mu \leftrightarrow \nu_\tau$진동을 가정하면 잘 설명된다. 이 연구에서는 대기 뮤온 중성미자가 zenith angle과 에너지에 따라서 감소되는 관측사실을 이용하여 중성미자 진동 현상을 분석하였다. 진동변환상수를 결정하는데, 운동량 binning이 끼치는 영향을 연구하였고, 최적의 운동량 binning에서 수퍼 카미오칸데-I 과 수퍼 카미오칸데-II 데이터를 합하여 분석한 결과, 최적의 진동변환상수는 $\sin^2 2\theta = 1.00$ 과 $\Delta m^2 = 2.5\times10^{-3}$ eV^2 에 위치하고, 그 때의 χ^2/DOF는 767.5/737 이다. 90% C.L.에서 진동변환상수의 범위는 $\sin^2 2\theta > 0.93$ 과 $2.1\times10^{-3} < \Delta m^2 < 3.0\times10^{-3}$ eV^2 이다.